

DYNAMICS EXPLORER-1 SATELLITE STUDY  
OF ELECTROSTATIC ION CYCLOTRON WAVES

by

Scott Arnold Boardsen

An Abstract

Of a thesis submitted in partial fulfillment  
of the requirements for the Doctor of  
Philosophy degree in Physics  
in the Graduate College of  
The University of Iowa

December 1988

Thesis supervisor: Professor Donald A. Gurnett

## ABSTRACT

This thesis describes representative examples of hydrogen cyclotron waves detected by Dynamics Explorer-1 (DE-1). Most of the hydrogen cyclotron waves can be classified into two categories: 1) wave events in which the excited harmonics are located below the lower hybrid frequency, and 2) wave events in which the excited harmonics are located at or above the lower hybrid frequency. Wave events satisfying the first category are strongly correlated with the presence of ion beams flowing up the field lines, while events satisfying the second category are associated with loss cone features in the ion distribution functions. However, the loss cone features usually persist before and after the hydrogen cyclotron wave events. The hydrogen wave emissions that occur below the lower hybrid frequency are found to be a factor of 10 to 100 times more intense than emissions that occur above the lower hybrid frequency. Examples are shown in which the ion cyclotron emissions in the second category have a double peaked spectral characteristic. The double peaked spectrum is shown to be produced by Doppler shifts from a spectrum of wave vectors distributed uniformly in azimuth around the magnetic field. The separation between the double peaks can be used to infer the wavelength of the emissions. The global distribution of hydrogen cyclotron waves is also investigated. The

global distribution is found to coincide with the statistical auroral oval, with the waves occurring at higher invariant latitudes near noon magnetic local time and at lower latitudes around midnight magnetic local time. The distribution of hydrogen cyclotron waves exhibits a strong dawn-dusk asymmetry, occurring mainly in the afternoon and evening sectors. The frequency of occurrence agrees within a factor of two with the frequency of occurrence of ion beams detected at lower altitudes by the S3-3 satellite. A sharp drop off in the number of hydrogen cyclotron wave events occurs at altitudes below 1 R<sub>E</sub>. Part of this drop off is due to Doppler broadening obscuring the detection of these waves.

Abstract approved:

Donald A. Gurnett  
Thesis supervisor

Prof., Physics and Astronomy  
Title and department

Dec. 2, 1988  
Date

DYNAMICS EXPLORER-1 SATELLITE STUDY  
OF ELECTROSTATIC ION CYCLOTRON WAVES

by

Scott Arnold Boardsen

A thesis submitted in partial fulfillment  
of the requirements for the Doctor of  
Philosophy degree in Physics  
in the Graduate College of  
The University of Iowa

December 1988

Thesis supervisor: Professor Donald A. Gurnett

Graduate College  
The University of Iowa  
Iowa City, Iowa

CERTIFICATE OF APPROVAL

PH.D THESIS

This is to certify that the Ph.D. thesis of

Scott Arnold Boardsen

has been approved by the Examining Committee  
for the thesis requirement for the Doctor of  
Philosophy degree in Physics at the December  
1988 graduation.

Thesis committee:

Donald A. Hummel  
Thesis supervisor

Dan T. Carpenter  
Member

Robert H. Merlino  
Member

Christopher K. Gail  
Member

D. R. AL  
Member

## ACKNOWLEDGEMENTS

I wish to express my appreciation to Dr. Gurnett for his support, helpful suggestions, guidance and patience. I wish to express my gratitude to Bill Peterson for the time and effort he spent in analyzing EIC's particle data that was observed during these wave events. I wish to acknowledge Dr. Hoffman and Dr. Ghielmetti for letting me include their data in this thesis. I wish to show my appreciation to Rich Huff and Ann Persoon for helping me with the DE-1 data analysis. I wish to express my gratitude to Miles Bailey and other engineers for orienting me with the logcompressor. I wish to thank Paul Hansen for his prompt handling of my request for data analysis. I'd also like to thank Mark Brown, Terry Averkamp, and Tracy Barnett-Fisher for handling data processing requests. I wish to express my gratitude to Mark Baumbach for his legacy of the spectrum analyzer. Last I'd like to thank Kathy Kurth for the good food.

This research was supported by the National Aeronautics and Space Administration through grants NAG5-310 and NGL 16-001-043.

## ABSTRACT

This thesis describes representative examples of hydrogen cyclotron waves detected by Dynamics Explorer-1 (DE-1). Most of the hydrogen cyclotron waves could be classified into two categories: 1) wave events in which the excited harmonics are located below lower hybrid frequency, and 2) wave events in which the excited harmonics are located at or above the lower hybrid frequency. Wave events satisfying the first category are strongly correlated with the presence of ion beams flowing up the field lines, while events satisfying the second category are associated with loss cone features in the ion distribution functions. However, the loss cone features usually persist before and after the hydrogen cyclotron wave events. The hydrogen wave emissions that occur below the lower hybrid frequency are found to be a factor of 10 to 100 times more powerful than the emissions that occur above the lower hybrid frequency. Examples are shown in which the ion cyclotron emissions in the second category have a double peaked spectral characteristic. The double peaked spectrum is shown to be produced by Doppler shifts from a spectrum of wave vectors distributed uniformly in azimuth around the magnetic field. The separation between the double peaks can be used to infer the wavelength of the emissions. The global distribution of hydrogen cyclotron waves is also investigated. The

global distribution is found to coincide with the statistical auroral oval, with the waves occurring at higher invariant latitudes near noon magnetic local time and occurring at lower latitudes around midnight magnetic local time. The distribution of hydrogen cyclotron waves exhibited a strong dawn-dusk asymmetry, occurring mainly in the afternoon and evening sectors. The frequency of occurrence in magnetic local time and invariant latitude of hydrogen cyclotron waves detected by DE-1 agrees within a factor of two with the frequency of occurrence of ion beams detected at lower altitudes by the S3-3 satellite. A sharp drop off in the number of hydrogen cyclotron wave events occurred at altitudes below 1  $R_E$ , part of this drop off is due to Doppler broadening obscuring the detection of these waves.



# TABLE OF CONTENTS

|   | Page |
|---|------|
| LIST OF TABLES . . . . .  | vi   |
| LIST OF FIGURES . . . . .   | vii  |
| I. INTRODUCTION . . . . .   | 1    |
| II. DESCRIPTION OF THE DYNAMICS EXPLORER 1 SATELLITE . . . . .      | 7    |
| III. DISCUSSION OF TYPICAL ION CYCLOTRON WAVE EVENTS . . . . .      | 13   |
| A. EIC Waves Associated With Ion Beams . . . . .                    | 14   |
| B. Ion Cyclotron Harmonic Waves . . . . .                           | 18   |
| IV. GLOBAL DISTRIBUTION OF H <sup>+</sup> CYCLOTRON WAVES . . . . . | 21   |
| V. DOPPLER EFFECTS . . . . .  | 29   |
| A. Observations of Double Peaked Harmonics . . . . .                | 29   |
| B. Interpretation of Double Peaked Harmonics . . . . .              | 32   |
| C. Spectral Broadening in General . . . . .                         | 40   |
| VI. CONCLUSION . . . . .  | 42   |
| APPENDIX: DISCUSSION OF THE LOGARITHMIC COMPRESSOR . . . . .        | 130  |
| A. Discussion of the Compressor Circuitry . . . . .                 | 130  |
| B. Computer Generated Test Signals . . . . .                        | 134  |
| REFERENCES . . . . .  | 135  |

## LIST OF TABLES

| Table |   | Page |
|-------|---|------|
| 1.    | Parameters Used in Dispersion Relationship . . . . .              | 44   |
| 2.    | Measured Perpendicular Phase Velocities of<br>Harmonics . . . . . | 45   |

## LIST OF FIGURES

| Figure |  | Page |
|--------|--|------|
| 1      | This figure shows a plot of the orientation of the satellite orbit in the orbital plane at two different times. One orbit occurred on January 4, 1984, and the other orbit occurred on May 24, 1984. The fuzzy trace on each of the orbits corresponds to the detection of electrostatic H <sup>+</sup> cyclotron waves by the DE-1 satellite. The lines that intersect the Earth's surface (at geographic latitudes of 65° and 85° in both hemispheres) are magnetic field lines. . . . . | 46   |
| 2      | This figure (a) shows the sine wave input signal before compression, and (b) is the resulting compressed output signal. . . . .  | 48   |
| 3      | This figure (a) shows the spectrum of the input signal which is composed of two frequency components, and (b) is the spectrum of the resulting compressed signal. Figure 3c is the spectrum of the input signal which is composed of four frequency components, and (d) is the corresponding spectrum of the compressed signal. . . . .  | 50   |
| 4      | In this figure (a) is the spectrum of a more complex input signal, and (b) is the spectrum of the resulting output signal. Figure 4c is the spectrum of a more complex input signal, and (d) is the spectrum of the resulting output signal. . . . .   | 52   |
| 5      | This figure is a spectrum of an EIC event that occurred at 14:38:54 UT on January 4, 1984, the evenly spaced vertical lines are located at integer multiples of the local H <sup>+</sup> cyclotron frequency. . . . .  | 54   |
| 6      | This figure is a spectrum of an IHC event that occurred at 07:19:35 UT on June 15, 1984, the evenly spaced vertical lines are located at integer multiples of the local H <sup>+</sup> cyclotron frequency. The fourth and eleventh harmonics are excited. . . . .   | 56   |

|    |  |    |
|----|--|----|
| 7  | This figure is a spectrogram of the EHC event that occurred on May 24, 1984, from 04:16 UT to 04:32 UT. . . . .  | 58 |
| 8  | This figure is a spectrum taken at 04:25:46 UT on May 24, 1984, showing the fundamental slightly above the H+ cyclotron frequency and a small number of of harmonics. . . . .  | 60 |
| 9  | In this figure is a plot of H+ and O+ particle flux recorded by Energetic Ion Composition Spectrometer in the 0-1 keV energy range as a function of time and pitch angle that occurred from 4:16 UT to 4:32 UT on May 24, 1984. . . . .  | 62 |
| 10 | In this figure is a plot of H+ and O+ particle flux recorded by Energetic Ion Composition Spectrometer in the 0-1 keV energy range as a function of time and pitch angle that occurred from 4:16 UT to 4:32 UT on May 24, 1984. . . . .  | 64 |
| 11 | This figure is a plot of the rms electric field recorded by the Ex antenna during the time interval from 04:16 UT to 04:32 UT on May 24, 1984, note the strong correspondence of local minimums in power with the disappearance of EHC wave during the interval. . . .   | 66 |
| 12 | This figure is a wideband spectrum taken at 10:40:46 UT on January 15, 1984, the evenly spaced lines are located at integer multiples of the local H+ cyclotron frequency. . . . .   | 68 |
| 13 | In this figure (a,b) are contour plots of the corresponding O+ and H+ velocity space distributions measured around 10:40 UT on January 15, 1984. The solid contours are spaced at the decade intervals of the phase space density measured in units of $s^3km^{-6}$ . The dashed curves are at half decade intervals. Particles with a positive parallel velocity are flowing toward the ionosphere. The axes are labelled in units of km/s. . . . . | 70 |
| 14 | This figure is the dispersion relationship for an H+ beam streaming through an O+ beam similar to the beams shown in Figure 12 which indicates that the EHC waves are damped and therefore H+ background is probably needed. The negative of the damping rate is plotted (dashed curve). . . . .   | 72 |

|    |  |    |
|----|--|----|
| 15 | This figure is a plot of rms electric field detected in the 1 kHz band for electrostatic ion cyclotron wave events versus geocentric Earth radii (in units of $R_E$ ). . . . .   | 74 |
| 16 | This figure is a spectrogram of an H <sup>+</sup> cyclotron harmonic event that occurred at 10:45 UT on day 15 of the year 1984. . . . .   | 76 |
| 17 | This figure is a plot of H <sup>+</sup> distribution function measured by EICs on June 12, 1984, at 10:45:28-46 UT. Note the loss cone feature flowing up the field line in the data. The solid contours are spaced at the decade intervals of the phase space density measured in units of $s^3 km^{-6}$ . The dashed curves are at half decade intervals. Particles with a positive parallel velocity are flowing toward the ionosphere. The axes are labelled in units of km/s. . . . . | 78 |
| 18 | This figure is a plot of rms electric field detected in the 1 kHz band for ion cyclotron harmonic events versus geocentric Earth radii (in units of $R_E$ ). . . . .   | 80 |
| 19 | This figure (a) shows a plot of the satellite orbit coverage when the wideband receiver was on as a function of geocentric Earth radii and invariant latitude, and (b) is a similar plot to (a) of orbit coverage when ICW events were detected. . . . .   | 82 |
| 20 | This figure (a,b) shows plots of the halfwidths normalized by the local H <sup>+</sup> cyclotron frequency for the (a) fundamental and the (b) second harmonic of a sample of electrostatic H <sup>+</sup> cyclotron wave events. . . . .  | 84 |
| 21 | In this figure (a) is a plot of the occurrence of ion cyclotron waves between 2 $R_E$ and 4 $R_E$ and 60° and 80° invariant latitude versus magnetic local time, and (b) is reproduced from Figure 3 in Ghielmetti et al. [1978] and is a plot of the relative occurrence of upflowing ion beam events versus magnetic local time in the auroral oval. . . . .   | 86 |
| 22 | This figure (a) shows a plot of satellite orbit coverage when the wideband receiver is on as a function of invariant latitude and magnetic local time, while (b) is a similar plot of orbit coverage when ICW events are observed. The circles are separated by 10° invariant latitude. . . . .  | 88 |

|    |   |     |
|----|---|-----|
| 23 | In this figure (a) is a plot giving the total time in minutes the wideband instrument was on in each bin between 2 and 3 Earth radii and (b) is a plot giving the total time in minutes the wideband instrument was on in each bin between 3 and 4 Earth radii. . . . .   | 90  |
| 24 | In this figure (a,b) are contour plots made from the binned observations of ion cyclotron waves normalized by wideband receiver ontime in each bin, (a) is a probability of occurrence plot as a function of magnetic local time and invariant latitude for observations between 2 and 3 Earth radii, and (b) is a probability of occurrence plot as a function of magnetic local time and invariant latitude for observations between 3 and 4 Earth radii. . . . .   | 92  |
| 25 | This figure (a) is reproduced from Figure 6 in Hoffman and Lin [1980] and is a plot of electron energy versus magnetic local time for inverted V events, while (b) is reproduced from Figure 4 in Hoffman and Lin and is a plot of the occurrence of inverted V events as a function of magnetic local time and invariant latitude. . . . .   | 94  |
| 26 | This figure (a) is a plot of the distribution of $K_p$ values for the year of 1984, while (b) is a plot of the distribution of $K_p$ values when ion cyclotron wave events are occurring. . . . .   | 96  |
| 27 | This figure (a) is a histogram of $A_e$ index for the year of 1984, and (b) is a histogram of $A_e$ index when ICW events were occurring. . . . .   | 98  |
| 28 | This figure is a spectrogram of the analog wideband electric field signal detected by the $E_x$ antenna on DE-1 in the 0-1 kHz mode. Split $H^+$ cyclotron harmonics are present between 300 Hz and 600 Hz. . . . .   | 100 |
| 29 | This figure (a) is a spectrum of the analog wideband electric field signal taken at 03:53:15 UT consisting of 50 spectrums averaged over 2.5 seconds. The evenly spaced lines are located at integer multiples of the $H^+$ cyclotron frequency. This figure (b) is a spectrum of the analog wideband electric field signal taken at 03:54:40 UT consisting of 250 spectrums averaged over 12.5 seconds. The 9th through 11th harmonics are excited, each one is split. This figure (c) is a spectrum consisting of |     |

|    |   |     |
|----|---|-----|
|    | 50 spectrums averaged over 2.5 seconds taken at 03:55:35 UT. In this figure (d) is a spectrum consisting of 250 spectrums averaged over 12.5 seconds taken at 03:56:20 UT. The evenly spaced lines are located at integer multiples of the H <sup>+</sup> cyclotron frequency. . . . .  | 102 |
| 30 | This figure is the rms electric field in the 10 Hz-1 kHz band measured by the E <sub>x</sub> antenna versus time. The dashed vertical lines indicate when the E <sub>x</sub> antenna is parallel to the magnetic field. . . . .   | 104 |
| 31 | This figure (a) is a plot of the spectrum obtained when the E <sub>x</sub> antenna is perpendicular to the magnetic field for various values of $\Delta k_{\perp 0}/k_{\perp 0}$ . $\Delta k_{\perp x}/k_{\perp 0} = (\omega - \omega_n)/(k_{\perp 0} V \sin \theta)$ relates the shift in frequency to $k_{\perp x}$ . This figure (b) is a plot of the spectrum obtained when the E <sub>x</sub> antenna is parallel to the magnetic field for various values of $\Delta k_{\perp 0}/k_{\perp 0}$ . . . . . | 106 |
| 32 | This figure is a plot of randomly selected perpendicular wave numbers lying in an annular ring of width $2\Delta k_{\perp 0}$ , centered at $k_{\perp 0}$ . . . . .   | 108 |
| 33 | In this figure (a) is a plot of the envelope of computer generated signal as seen by the E <sub>x</sub> antenna in DE-1's reference frame covering 1 spin period. The E <sub>x</sub> antenna is parallel to the magnetic field at 1.5s and (b) is the envelope of the signal shown in Figure 33a after it has been compressed. . . . .  | 110 |
| 34 | This figure (a) is the spectrum made from the six second signal shown in Figure 33a. (b) is the spectrum made from the six second compressed signal shown in Figure 33b. (c) is a spectrum, which consists of averaging spectrums made from 1 second subintervals, which cover the spin period. . . . .   | 112 |
| 35 | This figure (a) is a spectrum taken on January 15, 1984, where the 3rd to the 7th harmonics are excited. Figure (b) is a plot of the inferred inverse wavelengths versus the center frequencies for the excited harmonics shown in 8a. . . . .  | 114 |
| 36 | This figure is a plot of the log of phase space density versus energy for H <sup>+</sup> during the wave event. Each curve refers to a different pitch angle range in which the particle detector was sampling. . . . .   | 116 |

|    |   |     |
|----|---|-----|
| 37 | This figure is a histogram of the ratio of the second harmonic to that of the first harmonic for a number of ion cyclotron wave events, the peak in the histogram lies closer to 1 instead of 2. . . . .  | 118 |
| 38 | In this figure (a-c) shows the effect of introducing a phase coherence time into the wave modes that make up the signal. In Figure 38a the phase coherence time is .5s, coherence time is .1s (Figure 38b), and the phase coherence time is .025s in Figure 38c. . . . .  | 120 |
| 39 | This figure is a schematic of the logarithmic compressor. . . . .   | 122 |
| 40 | This figure shows the response time of the LC voltage when the input signal is suddenly switched on and then switched off after the LC voltage saturates. Each curve corresponds to an input signal with a different db level. Plot (a) is for a 700 Hz sine wave input signal, while plot (b) is for an input signal that consists of white noise. . . . . | 124 |
| 41 | This figure is a preflight calibration curve of LC output voltage vs. input voltage in decibels (referenced to 1 volt rms) for a 700 Hz sine wave input signal. The superimposed curved (smoother of the two curves) is a computer model generated calibration curve. . . . .   | 126 |
| 42 | This figure is a superimposed plot of the LC level versus input signal power of the single component sine wave case as compared to the white noise case. . . .  | 128 |



## I. INTRODUCTION

The purpose of this thesis is to use the Dynamics Explorer 1 spacecraft (DE-1) to study the global distribution of electrostatic ion cyclotron waves and to discuss and interpret cases in which the ion cyclotron harmonics take on a double peaked appearance. From this study we hope to gain a better understanding of the role these waves play in the coupling of the ionospheric and magnetospheric plasmas. This coupling occurs mainly in the auroral and polar regions. Electrostatic ion cyclotron waves are believed to play an important role in this coupling. These waves occur in a plasma which has a relatively strong magnetic field. Typically,  $\beta$ , the ratio of the plasma energy density to the magnetic field energy density, is less than 0.01. The ion cyclotron waves usually consist of strong emissions near harmonics of the ion cyclotron frequency ( $\Omega_i = e_i B / c M_i$ ). The wavelength of the fundamental is typically on the order of the ion cyclotron radius ( $\rho_i = v_{th,i} / \Omega_i$ ), with the electric field directed almost perpendicular to the magnetic field.

Observations of large fluxes of H<sup>+</sup> and O<sup>+</sup> ion's [Shelley et al., 1976] flowing up the auroral field lines from the ionosphere to the magnetosphere (upstreaming ions) indicated that the ionosphere is a significant source of ion's that make up the magnetospheric ion populations. These upflowing fluxes are either in the form of ion

beams or ion conics [Sharp et al., 1977; Klumpar et al., 1979]. One reason for studying electrostatic ion cyclotron waves is that these waves are believed to play a role in the transverse energization of  $H^+$  and  $O^+$  ions on the auroral field lines.

The ion energization process is believed to be composed of separate parallel and perpendicular energization mechanisms. The parallel processes are believed to be field aligned potential drops caused by anomalous resistivity and/or double layers in regions of field-aligned currents. The perpendicular processes are believed to be either due to wave mechanisms or perpendicular electrostatic shocks [Borovsky, 1984]. The two most studied wave mechanisms for transverse heating are lower hybrid waves and electrostatic ion cyclotron waves. Since waves can also contribute to anomalous resistivity, the parallel and perpendicular energization processes may be interrelated.

Electrostatic ion cyclotron (EIC) waves were first observed in laboratory experiments using a Q-machine [D'Angelo and Motley, 1962]. The waves were excited by drawing a current along a magnetized plasma column. Drummond and Rosenbluth [1962] did the first theoretical study of current driven EIC waves. They showed that EIC's have a lower instability threshold compared to the ion acoustic mode. The detection of field aligned currents along the auroral field lines [Cloutier et al., 1971; Choy et al., 1970] lead to the suggestion that ion cyclotron waves may play a role in producing anomalous resistivity and diffusion along the auroral field lines. An extensive study of the current driven EIC instability using a Maxwellian distribution and linear

stability theory was done by Kindell and Kennel [1971]. They showed that for a wide range of parameter values ( $T_e/T_i$ , etc.) EIC waves have a lower instability threshold than other electrostatic instabilities that occur in the auroral ionosphere. For plasmas consisting of both  $H^+$  and  $O^+$  ions they showed that oxygen cyclotron waves have the lowest instability threshold when at least 10% of the plasma is composed of  $O^+$ . They also indicated that the electrostatic instability will dominate the electromagnetic instability as long as  $\beta \leq 10^{-3}$ .

A theoretical study of transverse heating of ions by ion cyclotron waves generated by field-aligned currents was carried out by M. Ashour-Abdalla and H. Okuda [1984]. Based on a marginal stability analysis they showed that the heating saturated when the temperature anisotropy increases to a point where the ion cyclotron waves are no longer destabilized by the drifting electrons. They also carried out plasma simulations of the plasma heating process. They found that transverse heating of  $O^+$  is generally greater than the transverse heating of  $H^+$ .

Electrostatic  $H^+$  ion cyclotron waves were first detected in the ionosphere from sounding rocket experiments [Mosier and Gurnett, 1969]. Later Bering et al. [1975] detected  $O^+$  cyclotron waves. A survey of electrostatic ion cyclotron waves has been made by Kintner et al. [1979] using the S3-3 satellite. Their survey covered a range from 500 km to 8000 km.  $H^+$  ion cyclotron waves occurred along the auroral field lines between  $65^\circ$  and  $85^\circ$  invariant latitude. They also present a case

in which  $H^+$  ions formed a conic distribution that was associated with electrostatic  $H^+$  cyclotron waves. Their data for this event indicates that drifting thermal ionospheric electrons were probably driving these waves. However, their study is not conclusive in identifying the instability mechanism. Peterson et al. [1988] using DE-1 data presents a case where perpendicular heating of the  $O^+$  ions seems to occur in association with  $H^+$  cyclotron waves. However, field-aligned currents could also be the wave source.

At present, there is little observational evidence that ion cyclotron waves play a major role in ion energization at low altitudes in the auroral region. There is also no observational data that clearly shows drifting thermal electrons as the wave source. One reason for the lack of confirmation of the basic instability mechanism, is that spacecraft charging makes measurements of the cold thermal electron component very difficult. Despite significant satellite coverage of the lower auroral region few observations of ion cyclotron waves exist in this region. The absence of ion cyclotron waves in this region is usually attributed to Doppler broadening of the ion cyclotron waves caused by the satellite's velocity relative to the plasma's rest frame.

Kintner et al. [1979] observed a sharp dropoff of S3-3 satellite observations of ion cyclotron waves at altitude's below 5000 km. They also arrived at the following conclusions about ion cyclotron waves.

- 1) The waves appear to be coherent in nature.
- 2) There seems to be a high correlation between upstreaming ion events and the presence of

electrostatic ion cyclotron waves. 3) The upstreaming ions are in the form of either beams or conics or a superposition of both. 4) A strong correlation was observed between ion density fluctuations and the maximum in upstreaming ion energy, which is consistent with the idea that ion cyclotron waves heat the ions, but could also indicate that ion beams are the source of electrostatic ion cyclotron waves.

Mozer et. al. [1977] using S3-3 data observed ion cyclotron waves associated with inverted V events. Inverted-V events are potential structures that develop along the magnetic field lines. In the middle of the structure the potential drop occurs mostly parallel to the magnetic field. The waves observed by Mozer et al. [1977] are probably destabilized by ion beams instead of by field aligned currents. Rachelle Bergmann [1984] performed a theoretical study using linear Vlasov theory and determined that ion beams can destabilize electrostatic ion cyclotron waves if the electron temperature is much greater than the ion temperature. This is true for most inverted-V events [Temerin et. al., 1979]. Numerical studies of ion beam driven electrostatic hydrogen cyclotron waves have been carried out by H. Okuda and K. I. Nishikawa [1984]. Since DE-1 makes observations mainly in the mid-altitude (2 to 4.6 Earth radii) auroral region as opposed the low altitude (1 to 2 Earth radii) auroral region, ion cyclotron wave events associated with ion beams are probably the dominant mode.

This thesis is divided into five chapters. Chapter II gives a brief discussion of the DE-1 satellite, its orbit and the instrumentation pertinent to this study. Chapter III presents selected

case studies typical of the ion cyclotron wave events observed by the DE-1 satellite. Chapter IV presents a statistical study of the global distribution of ion cyclotrons waves in the region swept out by DE-1 during the time period studied. Chapter V discusses cases in which the ion cyclotron wave spectrum has a double-peaked appearance. Chapter VI summarizes the conclusions of the study.

## II. DESCRIPTION OF THE DYNAMICS EXPLORER 1 SATELLITE

DE-1 is in an ideal orbit for studying ion cyclotron waves along the mid-altitude auroral field lines. Among the existing satellites at the beginning of this study, DE-1's orbit was uniquely positioned to study mid-altitude auroral phenomena. This spacecraft is in a polar orbit about the Earth with an apogee of  $4.67 R_E$  and a perigee of  $1.106 R_E$ . The orbital period is roughly 7 hours. Figure 1 shows DE-1 orbits for January 4 and May 24 of 1984. The magnetic field lines intersecting the Earth are located at  $65^\circ$  and  $85^\circ$  degrees geographic latitude. These magnetic field lines approximately define the polarward and equatorward edge of the auroral oval. Note that DE-1 makes four auroral zone crossings every orbit, two in the northern hemisphere and two in the southern hemisphere.

Note that the orientation of the DE-1 orbit in the orbital plane has changed from January 4 to May 24. This change in the orientation of the orbit is called the advance of the line of apsides, which occurs at a rate of approximately  $108^\circ$  per year. This motion is caused by the Earth's quadrupole moment. The advance of the line of apsides allows DE-1 to sample the auroral plasma environment from  $1.106 R_E$  to  $4.67 R_E$ . The fuzzy segments on each orbit show where electrostatic  $H^+$  cyclotron waves were detected, in one case a large range in altitude was covered,

while in the other case the satellite was cutting almost directly across the field lines.

The coordinate system used to define the spatial location of the DE-1 satellite in this study is the following. The geocentric radial distance is the distance between the satellite and the center of the Earth and is usually expressed in units of Earth radii ( $R_E$ ). If the Earth's magnetic field was described by a perfect dipole aligned with the spin axis, invariant latitude would correspond to the geographical latitude at which the magnetic field line which passes through DE-1 intersects the Earth's surface in the northern hemisphere. Invariant latitude is usually expressed in units of degrees. Magnetic local time is defined as the projection of the angle formed between the Sun, the Earth, and the satellite onto the Earth's magnetic equator (which almost coincides with the Earth's geographic equator). Magnetic local time is expressed in units of hours.

If the satellite is between the Sun and the Earth, the magnetic local time is 12 hrs (noon). If the Earth is between the Sun and the satellite the magnetic local time is 24 hrs (midnight). In each orbit DE-1 samples two different magnetic local times (MLT) in the auroral region separated by approximately 12 hrs. Since the orbital plane remains fixed in space as the Earth revolves around the sun, the magnetic local times sampled by DE-1 changes by 0.066 hrs each day. Therefore, in half a year DE-1 samples a full range of magnetic local times (0 hrs to 24 hrs). A half year of observations does not cover the a full range of radial distance. In order to get complete coverage



of all altitudes over the auroral zone, three years of data are required.

The DE-1 spin axis is oriented perpendicular to the orbital plane and the period of rotation is roughly 6 seconds. A 215-meter electric antenna ( $E_x$ ), oriented perpendicular to the spin axis of the spacecraft is used to detect the electric field of the ion cyclotron waves. The signal detected by the  $E_x$  antenna is processed by the plasma wave instrument (PWI).

The plasma wave instrument (PWI) consists of three receiver systems. The step frequency correlator (SFC), the low frequency correlator (LFC) and the wideband receiver (WBR). Both the SFC and LFC are digital and play only a minor role in this study so they will not be discussed further. The PWI also uses the  $E_x$  antenna for DC field measurements. The DC measurements are of potential value in detecting ion cyclotron waves that occur in the frequency range of 1 Hz to 8 Hz. The DC-field data is also needed to measure the plasma flow velocity and for the detection of electrostatic shocks. The wideband receiver is analog and is the principal instrument used in this study.

The wideband receiver can be operated in 4 different modes. Since the typical harmonic spacing of ion cyclotron waves is  $< 100$  Hz the wideband receiver was operated in the mode that provides the highest resolution at frequencies of a few hundred Hz. In this mode the input signal, detected by the  $E_x$  antenna, is band limited by a 1 kHz filter and also a 10 kHz filter. To enhance the dynamic range of the signal, the amplitude of the 10 kHz signal is adjusted by an automatic gain

control (AGC). The 1 kHz signal is passed through a logarithmic compressor to reduce the dynamic range that must be transmitted. Signals in the 1 kHz band are strongly attenuated below 10 Hz by a series of filters. The output from the logarithmic compressor modulates a 13.6 kHz subcarrier which is added to the 10 kHz signal. The composite signal is then transmitted to a ground station in real time.

The data transmitted to Earth is stored on magnetic tape along with a time code, so it can be processed later. Both spectrograms and digital spectra can be made from the analog signal. Spectrograms are made by processing of the signal with a 500 channel spectrum analyzer that covers the frequency range of interest: for a 0-1 kHz wideband signal the typical frequency resolution is 2 Hz per channel. The voltage from each channel drives a corresponding light cell in an array of 500 light cells whose intensity is proportional to the logarithm of the corresponding channel voltage. Photographic film transverses this linear array of light cells at a constant rate to produce the time axis on the spectrogram.

The H<sup>+</sup> cyclotron waves can be detected by searching the 1 kHz spectrogram for structure near the H<sup>+</sup> cyclotron frequency. Since the study is of waves with a harmonic nature, it is important to consider the nonlinear distortion of the signal caused by the satellite instrumentation that processes the signal. The principal source of nonlinear signal distortion is the logarithmic compressor. To gain a quantitative understanding of the distortion that occurs in the

logarithmic compressor, a simple computer model was developed to simulate the operation of this circuit..

The computer model of the logarithmic compressor is discussed in detail in the Appendix. To demonstrate the effect of the logarithmic compression on the signal a few examples will be given. The simplest case is when the input signal consists of just one sine wave (Figure 2a). The resulting spectrum after compression is shown in Figure 2b. Compression has the effect of transforming a sine wave into a signal that resembles a rounded square wave. The spectrum of the compressed signal is similar to the spectrum of a square wave.

If the input signal consists of two frequency components of equal amplitude the resulting output spectrum is more complicated. Figure 3a-b shows the corresponding input and compressed signal spectra for the two component case. Sidebands spaced at the frequency difference between the frequencies of the two input signals are produced. The input and compressed output spectra for a four frequency component input signal are shown in Figures 3 c-d. Comparison of Figures 2 a-b with Figures 3 c-d shows that a simple modification of the input signal adds more detail to the resulting compressed spectrum.

The spectra of more complex input signals closer to reality are shown in Figures 4a-d. Figure 4a is the spectrum of a complex input signal whose compressed spectrum is shown in Figure 4b. Figure 4c shows the spectrum of another complex signal whose compressed spectrum is shown in Figure 4d. These spectra indicate that the larger frequency components seen in the compressed satellite

data are probably real, but care should be taken in interpreting peaks that are small in relation to the primary signal.

A number of points can be made about the effects of compression on the data. 1) The two largest spectral peaks are probably real. 2) Compression alters the ratio of the spectral power of the two largest signals. 3) Compression reduces the ratio between the maximum and minimum in amplitude of an amplitude modulated waveform. One implication is that the modulation caused by the satellite's spin is reduced and becomes more difficult to detect. 4) Once the input signal is large enough for nonlinear compression to occur, the shape of the compressed frequency spectrum hardly changes even when the input signal's power is increased. 5) Compression can produce a signal close to zero hertz which is completely instrumental in nature (Figure 4b). A spectral peak observed below 10 Hz is almost certainly instrumental in nature. The fundamental of  $O^+$  is usually below 10 Hz and therefore, detecting  $O^+$  ion cyclotron waves in the wideband analog wave data is difficult.

### III. DISCUSSION OF TYPICAL ION CYCLOTRON WAVE EVENTS

Plasma waves with structure near the ion cyclotron frequency or spaced at harmonics of the ion cyclotron frequency have been observed in both the ionosphere and the magnetosphere. The waves are generally grouped into two different categories [Kintner, 1980]. 1) Plasma waves in which the fundamental and lower harmonics (usually in the range 2-5) are excited are called electrostatic ion cyclotron waves (EIC). 2) Plasma waves with structure occurring at high harmonic numbers (usually  $n > 5$ ) with no lower harmonics present are called ion cyclotron harmonics (ICH).

Figure 5 shows the spectrum of an EIC event. The vertical lines in the plot are spaced at integer multiplies of the local  $H^+$  cyclotron frequency. The fundamental, second, third, and possibly the fourth harmonics are excited. This event occurred on January 4, 1984, and is discussed in detail in Peterson et al. [1988]. Note the appearance of double peaks in the second and third harmonics. This effect is discussed in Chapter 5. For EIC events the excited harmonics are observed to occur at frequencies below the lower hybrid frequency. This observation is based on EIC events in which plasma density and ion ratio estimates are available.

Figure 6 is a spectrum of an ICH event. This event occurred on June 24, 1984. The fourth through the eleventh harmonics are excited.

For IHC events the excited harmonics occur at frequencies at or slightly above the lower hybrid frequencies. This observation is based on IHC events in which plasma density and ion ratio estimates are available. Ion cyclotron waves also occur that could be classified in either of the two categories [Peterson et al., 1986].

The two categories introduced by Kintner [1980] can be further classified according to the source of free energy that drives the waves unstable, such as ion beams, field aligned currents, loss cone distributions and ion conics. Ion cyclotron instabilities driven by ion beams and field aligned currents approximately satisfy the resonance condition  $\omega - k_{\parallel}V_{\parallel} = n\Omega$ , where  $V_{\parallel}$  is the velocity at which the largest contribution to the growth rate occurs. Ion cyclotron instabilities driven by loss cone distributions and ion conics can be either resonant or nonresonant in nature and are characterized by a region of positive slope  $\partial f / \partial v_{\perp} > 0$  in the reduced distribution function.

#### A. EIC Waves Associated With Ion Beams

For the majority of ion cyclotron waves events in which energetic ion data has been obtained, there is a strong correlation between the presence of ion cyclotron waves and upflowing ion beams. This correlation was also observed in the S3-3 data at lower altitudes.

Kaufmann and Kintner [1982] have performed a detailed analysis of an S3-3 observation of an EHC event generated by upward flowing H<sup>+</sup> beams. Their idea is that EHC waves tend to heat the H<sup>+</sup> distribution

perpendicular to the magnetic field lines. The perpendicular heating balances the tendency for perpendicular velocity to be converted into parallel velocity due to the mirror force. Since ion beams are the free energy source, the waves can't energize the beam ions. Instead the waves tend to redistribute the ions in velocity space. They show that in order for  $H^+$  beams to be the source of the instability cold thermal electrons of ionospheric origin must not be present because they heavily Landau damp the waves.

The absence of thermal ionospheric electrons was demonstrated by Mozer et al. [1977] with S3-3 data. This absence is due to parallel potential drops which develop along the auroral field lines. The potential drops acts as a barrier to the passage of ionospheric ions and also creates the observed ion beams. The energetic electrons of magnetospheric origin would be too hot to contribute significantly to Landau damping of the waves. However, Kaufmann and Kintner [1982] did not include the presence of simultaneous  $O^+$  beams, which are usually observed in both S3-3 and DE-1 data [Collin et al., 1987].

A spectrogram of a typical electrostatic ion cyclotron wave event that occurred on May 24, 1984, is shown in Figure 7. This event started at 04:16:40 UT and lasted to about 04:32:00 UT. A spectrum (Figure 8), which was taken at 04:25:26 UT shows that the fundamental is slightly above the  $H^+$  cyclotron frequency and that a small number of harmonics are present. Note that the EHC waves are continuous in the following sub-intervals 04:17 UT to 04:19 UT, 04:19:25 UT to 04:21 UT,

04:23:20 UT to 04:25 UT, 04:25:22 UT to 04:26:15 UT, and 04:27:10 UT to 04:30:17 UT.

To within the 24 sec resolution of the Energetic Ion Composition Spectrometer, these intervals correspond to the occurrence of inverted-V signatures formed by ion beams, which are observed flowing up the magnetic field lines. A plot (Figures 9 and 10) of H<sup>+</sup> (upper panel) and O<sup>+</sup> (middle panel) particle flux recorded by EICS in the 0-17 keV energy range as a function of time and pitch angle indicate when the ion beams are present. The triangular waveform in the lower panel is the pitch angle between the direction the EICS particle detector is looking and the magnetic field direction. When the detector is looking at upflowing ions the pitch angle is 180°. Low energy oxygen conics are sometimes present (4:19 UT, 4:21 UT to 4:23 UT) between the inverted-V structures.

The plot (Figure 11) of the rms electric field recorded by the E<sub>x</sub> antenna during the event on May 24 shows strong correspondence between local minima in wave power and the disappearance of the EHC waves. The large electric field that occurs around 4:25:50 UT correspond to the most energetic ion beams seen during the event. The spiky appearance of the wave amplitude is mainly due to the spacecraft spin modulation. The location of the spikes verify that the electric field intensity peaks occur when the E<sub>x</sub> antenna is perpendicular to the magnetic field, as would be expected for ion cyclotron waves.

The spectrum of another example of an electrostatic ion cyclotron wave event that occurred at 04:40:46 UT on January 15, 1984, is shown



in Figure 12. The first three harmonics are excited. The corresponding H+ and O+ velocity space distributions are shown in the contour plots in Figures 13a,b, respectively. The contour curves are placed at half decade intervals. The phase space density is in units of  $s^3 km^{-6}$ . Both contour plots show upstreaming ion beams of roughly the same energy. No information is available about the thermal ion background. Energetic Ion Composition Spectrometer cannot measure the thermal ion background.

To determine if an O+ beam streaming through an H+ beam without a H+ background can generate EIC waves, the linear growth rate of the ion cyclotron mode was investigated using drifting Maxwellians to approximate the observed particle beams. Typical parameters seen in the ion beams for the ion cyclotron wave events were used. By direct measurement from the contour plots, the beam velocities are found to be 220 km/s for H+ and 55 km/s for O+. The phase velocity can be estimated from the spectral half width of the fundamental  $\Delta f_{1/2} = 10-14$  Hz, therefore,  $\lambda = 2 \cdot v_{sat} / \Delta f_{1/2} = .738$  km, yielding a phase velocity  $v_{\phi} = \lambda \cdot f = 28$  km/s. If  $k_{\parallel}/k_{\perp} = .1$  then  $v_{\phi\parallel} = 280$  km/s. If  $k_{\parallel}/k_{\perp} = .2$  then  $v_{\phi\parallel} = 140$  km/s. The relative streaming velocity between the two ion species is 165 km/s. Therefore, depending on the value of  $k_{\parallel}/k_{\perp}$ ,  $v_{\phi\parallel}$  could possibly satisfy the resonance condition and excite ion cyclotron waves. Table 1 lists the parameters used and Figure 14 shows a plot of the resulting dispersion relationship. This solution indicates that the EIC waves are damped. Therefore, an H+ background is needed to support the H+ cyclotron waves.

A plot (Figure 15) of the rms electric field of ion cyclotron waves detected in the 1 kHz band versus the spacecraft geocentric radial distance shows that the field drops off at higher altitudes. One might expect that the density of events should be double peaked at lower altitudes, since there are two principal sources of the free energy that could generate these waves. Linear theory predicts a much larger growth rate for electron current driven instabilities compared to ion beam driven instabilities. Therefore the distribution of events could be double peaked. Unfortunately, not enough events are available to draw firm conclusions regarding the existence of two distinct source regions.

#### B. Ion Cyclotron Harmonic Waves

Observations of H<sup>+</sup> cyclotron harmonics are less frequent than electrostatic H<sup>+</sup> cyclotron wave observations. In the evening sector, H<sup>+</sup> cyclotron harmonics they have a tendency to occur near the equatorial edge of the auroral oval. It has been suggested that H<sup>+</sup> cyclotron harmonics play an important role in causing the proton precipitation that generates the diffuse aurora [Ashour-Abdalla et al., 1978]. Figure 16 shows a spectrogram of an H<sup>+</sup> cyclotron harmonic event. H<sup>+</sup> cyclotron harmonics can be seen between 200 Hz and 400 Hz. A spectrum of this event is shown in Figure 36a. A plot (Figure 17) of the H<sup>+</sup> distribution function measured by Energetic Ion Composition Spectrometer when the event occurred shows a loss cone feature in the H<sup>+</sup> velocity distribution.

This loss cone feature seems to be present in all ICH cases with spectra similar to the one shown. The loss cone region (since  $\partial f / \partial v_{\perp} > 0$ ) is a potential source of free energy that could drive these waves. However, in most cases the loss cone feature persists before and after the event. This doesn't rule out the possibility of the loss cone being the wave source if the thermal background that contributes to the damping of the waves changes. Also the slope of the loss cone feature in the distribution might change enough to trigger the event.

A plot (Figure 18) of the rms electric field detected in the 1 kHz band for ion cyclotron harmonic events versus radial distance shows that the field drops off at higher altitudes. This drop off probably reflects the filling in the loss cone as the ions flow up the magnetic field lines. Note that ion cyclotron harmonic events tend to be at least a factor of 10 to 100 less intense than electrostatic ion cyclotron events.

As a final note the extent to which the electrostatic nature of these waves can be verified will be discussed. The S3-3 satellite data indicated that there was a strong electrostatic (longitudinal) component to the ion cyclotron waves based on the presence of H<sup>+</sup> cyclotron harmonics in the relative density fluctuations, but the presence of an electromagnetic component cannot be not ruled out. To verify that these waves are electrostatic, the magnetic field data must show that a magnetic component does not exist.

To verify the electrostatic nature of the electrostatic H<sup>+</sup> cyclotron waves the digital magnetic signal from the LFC must be used,

and to verify the electrostatic nature of  $H^+$  cyclotron harmonics the digital magnetic signal from the SFC must be used. The digital instrumentation imposes a number of difficulties in confirming the electrostatic nature of ion cyclotron waves. Both the LFC and SFC sample the signal using a set of frequency channels. Each channel samples a specified frequency band. The frequency coverage provided by the channels doesn't cover the whole frequency range. Each SFC channel is sampled for a 1 second interval every 32 seconds, while each LFC channel is sampled for a 1 second interval every 4 seconds. Therefore, to verify the electrostatic nature on an ion cyclotron wave, one of its spectral peaks must lie within a frequency band of a spectral channel during a time interval in which that channel is sampling the magnetic antenna. Also the electric field intensity of the ion cyclotron wave must be low enough to rule out the possibility of cross talk occurring between the electric and magnetic receivers.

For  $H^+$  cyclotron wave events in which the above criteria were met, no evidence of a magnetic component (above the spacecraft noise level) was found. In cases where there was an enhancement in the magnetic signal, the enhancement seemed to be broad banded. These enhancements were probably associated with other processes that were occurring along the auroral field lines during the  $H^+$  cyclotron wave events. The most likely explanations are that the magnetic enhancements are associated with auroral hiss or field aligned current filaments.

#### IV. GLOBAL DISTRIBUTION OF H<sup>+</sup> CYCLOTRON WAVES

Low frequency analog wave data was collected for the entire year 1984, from which approximately 1000 hrs of data, consisting of approximately 1000 auroral crossings, were produced and systematically searched for ion cyclotron wave events. An ion cyclotron wave event is characterized by the presence of continuous or intermittent harmonic structure with a spacing that corresponds to the local H<sup>+</sup> cyclotron frequency. Harmonic structure which seemed to be absorption bands in saucers [Gorney et al., 1982] were excluded, this amounts to a small percentage of the total number of events.

A plot of the satellite orbit coverage when the wideband receiver was in the 1 kHz mode as a function of geocentric Earth radii and invariant latitude is shown in Figure 19a. The coverage between 65° and 85° invariant latitude is fairly dense. Figure 19b shows a plot similar to Figure 19a. This plot shows when ion cyclotron wave events were occurring. The events seem to be clustered between 70° and 80° invariant latitude, which coincides with the auroral oval. The number of events that occurred dropped off at low and high radial distance. The drop off at high radial distance is due to limited frequency resolution of the wideband receiver as discussed in Chapter II. The drop off at low radial distance is due to two factors 1) higher satellite velocities and smaller spatial scales across the auroral

field lines reduce coverage time, and 2) higher satellite velocities result in enhanced Doppler broadening of the harmonics, causing neighboring harmonics to overlap to the point where they cannot be resolved. To avoid errors in interpreting the data ion cyclotron wave events below  $2 R_E$  and above  $4 R_E$  will be excluded in the global study.

Plots of the H<sup>+</sup> cyclotron harmonic halfwidths normalized by the local H<sup>+</sup> cyclotron frequency are shown for the H<sup>+</sup> cyclotron fundamental and second harmonics (Figures 20a,b, respectively) for a number of electrostatic H<sup>+</sup> cyclotron wave events. The figures indicate a general trend for the H<sup>+</sup> cyclotron harmonic halfwidths normalized by the local cyclotron frequency to increase in regions of low altitude (high satellite velocities) as compared to regions of high altitude (low satellite velocities). The curves in the plot are the least squares fit of the function:

$$\Delta f_{1/2}/f_{C_i} = 2 \cdot V_{sat}/V_{T_i} \quad (4.1)$$

which assumes that the Doppler broadening is due to the satellite velocity ( $V_{sat}$ ), neglecting the plasma flow velocity ( $V_{flow}$ ), and that  $k \cdot \rho = 1$ . The ion temperature was allowed to vary exponentially as a function of radial distance, although the exponential dependence was very weak.

Assuming the broadening is just due to Doppler effects (not source broadening, etc.) the tendency for the relative half width to increase

as the altitude of the satellite decreases (satellite velocity increases) suggests why  $O^+$  cyclotron waves have not been detected. Assuming that the wavelength is on the order of the ion cyclotron radius and that the  $O^+$  ions have roughly the same bulk energy as the  $H^+$  ions, the relative Doppler broadening of  $O^+$  should be four times greater than the relative Doppler broadening of  $H^+$ . Taking .2 as the typical value of the relative Doppler broadening of  $H^+$  indicates that the relative Doppler broadening of  $O^+$  should be 0.8, which indicates that the detection of  $O^+$  cyclotron waves is difficult, if not impossible. Chapter 5 investigates the effect Doppler broadening should have on the harmonics and reaches the conclusion that another mechanism must also significantly contribute to the broadening of the spectral peaks.

Since electrostatic ion cyclotron waves are highly nonconvective in nature, the global distribution of ion cyclotron waves should be closely correlated with the global distribution of the free energy source necessary to drive the instability. There are a number of possible sources theoretically capable of producing ion cyclotron waves: 1) field aligned currents, 2) ion beams, 3) ion conics, 4) electrostatic shocks, and 4) three wave decay process, such as lower hybrid waves decaying into ion cyclotron waves.

A large proportion of the ion cyclotron wave events have harmonic structure that would classify them as electrostatic ion cyclotron waves. Since a strong correlation is seen in the DE-1 data set between the turning on and off of electrostatic  $H^+$  cyclotron waves and the

turning on and off of ion beams, one would expect the distribution of ion cyclotron waves to be similar to the distribution of ion beams. For the majority of the sampling time along the auroral field lines, DE-1 was above  $2 R_E$  and therefore within or above the potential structures that probably create the ion beams [Mozer et al., 1977]. Therefore, the correspondence of ion beams with the wave events is not surprising.

To illustrate the global correspondence between ion cyclotron waves and beams, a plot (Figure 21a) of the occurrence of ion cyclotron waves between  $2 R_E$  and  $4 R_E$  and  $60^\circ$  and  $80^\circ$  invariant latitude is compared to a plot (Figure 21b, which is a reproduction of a figure from Ghielmetti et al. [1978]) of the relative occurrence of upwelling ion events as a function of magnetic local time. These ion measurements are from the S3-3 satellite. Clearly upwelling ion events and ion cyclotron waves occupy the same region of magnetic local time. The two peaks seen in the histograms at 17 hrs and 21 hrs magnetic local time roughly agree. The only points in the histograms where there is a strong disagreement is after midnight. This disagreement could be due too the lack of observation time by the DE-1 satellite in this region.

The maximum in the probability of occurrence of upwelling ion events is 30%, while for the DE-1 satellite it is 15%. One reason for the discrepancy is that not all upwelling ion events are ion beams and these events would not be unstable to ion cyclotron waves. Also ion beam events have been observed by DE-1 in regions where no ion



cyclotron waves have been detected. The presence of ion beams alone does not guarantee that the ion cyclotron instability will occur. The thermal H<sup>+</sup> background plasma plays an important role as the medium for supporting H<sup>+</sup> cyclotron waves and in the damping of these waves. S3-3 is in a lower orbit than the DE-1 satellite with apogee being roughly at  $2.2 R_E$ . Therefore, only a slight overlap exists between the altitude coverage of the two satellites. Even in the region of overlap the occurrence of upwelling ion events is more common. This discrepancy may also be due to the fact that potential drops along the magnetic field lines are extended in altitude and many of the upflowing ion events have not had time to develop into ion beams.

A plot of satellite orbit coverage when the wideband receiver is operating is shown in Figure 22a as a function of invariant latitude and magnetic local time. The coverage time between  $70^\circ$  and  $80^\circ$  invariant latitude is fairly uniform except in the region between 2 hrs and 10 hrs magnetic local time, where the coverage is sparse. Figure 22b shows a similar plot of orbit coverage when ion cyclotron wave events are observed. Note that there is an enhancement in ion cyclotron wave activity in the late afternoon, early evening sectors.

Contour plots were made of the occurrence of electrostatic H<sup>+</sup> cyclotron waves by dividing the auroral zone into bins of geocentric radial distance, invariant latitude, and magnetic local time. The value placed in each bin was the total time ion cyclotron waves were observed in that bin divided by the total time the wideband receiver was on in that bin. These values can be loosely interpreted as the

probability of observing an ion cyclotron wave event upon transversal of a bin. To get an idea of the statistical bias associated with each bin, the total time in minutes the wideband instrument was on in each bin is shown (Figures 23a,b) for the ranges of  $2-3 R_E$  and  $3-4 R_E$ .

Contour plots made from binned data between  $2 R_E$  and  $3 R_E$ , and between  $3 R_E$  and  $4 R_E$  are shown in Figures 24a,b, respectively. The maximum in occurrence as a function of magnetic local time is at roughly  $75^\circ$  invariant latitude at dusk. The maximum shifts to about  $67^\circ$  invariant latitude at local midnight. This shift can be seen in both contour plots and agrees with the shift seen in statistical studies of the auroral oval [Akasofu, 1980].

Three local maxima in occurrence probability appear in Figure 24b at roughly 17 hrs, 21 hrs, and 24 hrs magnetic local time. The location of the maxima at 17 hrs, 21 hrs and 24 hrs correspond with the maxima in energy of field aligned electron beams that are observed during inverted-V events by the AE-D satellite. This correspondence can be seen by comparing Figure 24b with Figure 25a (reproduced from in Figure 25a in Hoffman and Lin [1980]). A plot (Figure 25a) of electron energy versus magnetic local time is shown, for inverted-V events from data obtained by the AE-D satellite, which is a low altitude satellite. Figure 25b is reproduced from Hoffman and Lin [1980] and shows observations of inverted-V events in a format similar to that of Figure 22a. Caution should be used in interpreting this correspondence since the sampling times (Figure 23b) corresponding to

two of the local maximum is relatively small, and also because the bin size is large.

Hoffman and Lin observed that the field structures are relatively stationary in time. Therefore, one can infer that a similar energy dependence for field aligned ion beams flowing out of the ionosphere should be observed. The spatial correlation between inferred maxima in ion beam energy and the occurrence of H<sup>+</sup> cyclotron wave is not surprising. This maxima in ion cyclotron wave occurrence are not observed in the  $2 R_E$  to  $3 R_E$  bin which suggests that the extent in altitude of the potential structures that develops along the field lines is dependent on electron energy.

Hoffman and Lin also found no dependence on the occurrence of inverted-V events with the degree of magnetic activity. This is also true of ion cyclotron wave data when compared to the  $K_p$  and  $A_e$  indexes, which are a measure of magnetic activity. A plot (Figure 26a) of the distribution of  $K_p$  values for the year of 1984 is compared to a plot (Figure 26b) of the distribution of  $K_p$  values when ion cyclotron wave events are occurring. Both curves are quite similar in structure and imply the occurrence of an ion cyclotron wave event is independent of  $K_p$  index.

A histogram of  $A_e$  index for 1984 is shown in Figure 27a, while Figure 27b is a histogram of  $A_e$  index when ion cyclotron wave events were occurring. The mean value of  $A_e$  index when ion cyclotron wave events were occurring is 210 compared to a mean of 270 for 1984.

Except for the bite out in the histogram of Figure 27b between 100-150, both plots appear similar.

## V. DOPPLER EFFECTS

In some of the DE-1 observations, the ion cyclotron emissions take on a double peaked characteristic. The purpose of this section is to describe the double peak structure of the H<sup>+</sup> cyclotron harmonic emissions and discuss their interpretation. The double peak can be interpreted in terms of the Doppler shift arising from the satellite's velocity relative to the plasma's rest frame. Kintner et al. [1978] interpreted the broadening of ion cyclotron emissions in terms of Doppler shifts and used the broadening to estimate the phase velocity of the waves. However, no reports have been made of double peaks caused by Doppler shifts.

### A. Observations of Double Peaked Harmonics

The observations of interest cover a series of H<sup>+</sup> cyclotron harmonic emissions that started at approximately 3:53 UT and ended at 3:58 UT on June 1, 1984. During this event the radial distance varied from 2.67  $R_E$  to 2.84  $R_E$  and the invariant latitude varied from 73.2° to 75.9°. The magnetic local time was about 16 hrs.

Figure 28 shows a spectrogram of a H<sup>+</sup> cyclotron harmonic emission on June 1, 1984. The hydrogen cyclotron harmonics are first clearly observed at 3:53:06 UT at around 600 Hz and the emissions end at

3:53:50 UT. The H<sup>+</sup> cyclotron harmonics during this time interval show no double peaks.

At 3:53 UT a lower continuous band of wave activity becomes apparent at approximately 300 Hz, below the cyclotron harmonics. Figure 29a shows a spectrum of the H<sup>+</sup> cyclotron harmonics and the continuous band just below it. The evenly spaced lines are located at integer multiples of the H<sup>+</sup> cyclotron frequency. The 12-14th harmonics are present and occur just below  $n \cdot f_{H^+}$ . The first 4 harmonics are also present. The rms electric field in the 10 Hz to 1 kHz range averaged over the time period 03:53:06 UT to 03:53:50 UT is approximately .15 mV/M. At approximately 03:54 UT the lower band appears to merge with the band of hydrogen cyclotron harmonics at approximately 450 Hz. It should also be added that this lower continuous band is not always present during other time intervals when H<sup>+</sup> cyclotron harmonics are observed.

At this point the H<sup>+</sup> harmonics first take on a double peaked nature. Figure 29b shows a spectrum covering the time interval 03:54:50 UT to 03:55:00.3 UT. Note that the 9-11th harmonics are excited and that each harmonic shows a distinct double peak. The 10th harmonic most clearly shows the double peak. Figure 29c,d are similar to Figure 29b but taken at different times. Figure 29d is interesting in that only one harmonic is present. In all of the harmonics shown in Figures 29b,c and d the lower peak of each harmonic  $n$  is located below  $n \cdot f_{H^+}$  and the higher peak is located above  $n \cdot f_{H^+}$ . These illustrations clearly show that the H<sup>+</sup> harmonics dominate the

spectrum. The double peaked H<sup>+</sup> harmonics persist almost continuously from 03:54 UT to 03:58:25 UT, at which time the H<sup>+</sup> harmonics completely disappear, but the continuous band of wave activity persists until 04:01 UT. The rms electric field strength is roughly .26 mV/M when the double peaked harmonics are present.

The H<sup>+</sup> cyclotron harmonics are strongly spin modulated. This modulation is not easily detected in the spectrogram due to the logarithmic compression of the data by the wideband receiver. But it does clearly show up in the rms electric field strength in the 10 Hz-1 kHz band. Figure 30 is a plot of the rms electric field strength versus time over the interval 03:55 UT to 03:56 UT. The dashed vertical lines in the plot indicate when the  $E_x$  antenna is parallel to the magnetic field. This plot can be used to estimate  $k_{\parallel}/k_{\perp}$  since the H<sup>+</sup> harmonics make the dominant contribution to the rms electric field strength. The ratio  $k_{\parallel}/k_{\perp}$  is estimated to be less than .2. It is also possible that  $k_{\parallel}/k_{\perp}$  could be much less if the contribution made by the background could be subtracted from the plot. This ratio indicates that the spread in unstable  $k_{\parallel}$  is at least a factor of 5 smaller than the spread in unstable  $k_{\perp}$ .

Hydrogen cyclotron harmonic emissions that are double peaked are a factor of 16 times smaller in electric field intensity than the average intensity of H<sup>+</sup> cyclotron harmonics observed by DE-1 between  $2.5 R_E$  and  $3 R_E$ . The double peaked events lie at the lower edge in electric field intensity formed by the ICH events shown in Figure 17. This suggests that the free energy source driving these waves is marginally unstable.

Thus, only a limited range of wavenumbers for each harmonic are excited. However, it should be pointed out that there are other low intensity events like the one occurring from 03:53:06 UT to 03:53:50 UT that don't exhibit double peaked harmonics. One possible explanation is that the ratio of the electric field intensity to the electron temperature is the important parameter for determining if double peaked harmonics should be observed because this ratio is a measure of the degree of nonlinearity (the relative density fluctuations) that is involved in the physics of the harmonic emissions. Unfortunately no electron data are available for H<sup>+</sup> cyclotron waves observed by DE-1. The Doppler effect interpretation given in section III indicates that the ratio  $\Delta k_{\perp}/k_{\perp 0}$ , is an important parameter in detecting double peaked H<sup>+</sup> cyclotron emissions, where  $\Delta k_{\perp}$  is the spread in unstable wave modes centered about the wavenumber  $k_{\perp 0}$ . Lowering this ratio would lead to an enhancement of the double peaked nature of the harmonics.

### B. Interpretation of Double Peaked Harmonics

To see how the Doppler shift can cause double peaked harmonics, consider a plasma in which two wave components are excited in the rest frame of the plasma. Both waves have the same frequency  $f_0$  and wavelength  $\lambda$ , but one wave is propagating in the +x direction while the other wave is propagating in the -x direction. An observer in the rest frame of the plasma would detect one frequency component at  $f_0$ , while an observer moving relative to the plasma with a velocity  $V$  in the x



direction would detect two components with frequencies at  $f_0 - v/\lambda$  and  $f_0 + v/\lambda$ .

Now consider a plasma with many waves excited, each wave having the same wavelength and frequency but with wave vectors distributed uniformly in all directions in the x-y plane. At first one might think that this would fill in the gap between the shifted frequency peaks producing a single peaked spectrum, but as will be shown a double peaked spectrum occurs. The reason is that the spectrum seen by the observer moving relative to the plasma when looking in a direction  $\phi$  in the x-y plane ( $\phi$  is measured with respect the +x direction) is proportional  $1/|\sin\phi|$ . A more detailed analysis is given below.

For simplicity it will be assumed that each harmonic  $n$  is composed of waves of monochromatic frequency  $\omega_n$ . The justification of this assumption is based on the observation that the power present in the wideband data is low during these events indicating that the waves are marginally unstable. The assumption of marginally unstable waves implies that  $\Delta k_{\perp}/k_{\perp 0}$  is much less than 1. To show how the Doppler shift affects the spectrum, consider a function  $\underline{E}(\underline{X}, t)$  that describes the amplitude of the electric field in a certain region of space. Now consider a satellite traveling through that region of space with a velocity  $\underline{V}$ . The satellite measures the component of the electric field detected by the  $\underline{E}_x$  antenna. The amplitude of the signal is given by  $\phi(t) = \underline{e}_x(t) \cdot \underline{E}(\underline{V}t, t)$ , where  $\underline{V}t$  has been substituted for  $\underline{X}$  and  $\underline{e}_x(t)$  is a unit vector that points along the  $\underline{E}_x$  antenna. The signal can be represented by the following integral:

$$\phi(t) = \underline{e}_x(t) \cdot \sum_n \iiint dk_{\perp x} dk_{\perp y} dk_{\parallel} E_n(k_{\parallel}, k_{\perp}) \exp(i[\omega_n - \underline{k} \cdot \underline{V}]t) \quad (5.1)$$

In Equation 5.1 the Doppler shift of each frequency component is contained in the exponential term. The magnetic field  $\underline{B}$  is chosen to lie along the z axis and  $\underline{V}$  lies in the x-z plane making an angle of  $\theta$  with respect to the magnetic field.

To obtain the frequency spectrum,  $\phi(t)$  is multiplied by  $e^{-i\omega t}$  and then integrated over time from  $t_0 - T/2$  to  $t_0 + T/2$ . Where the time interval  $T$  is chosen to be small enough such that  $\underline{e}_x(t)$  is approximately constant over the time interval, and therefore  $\underline{e}_x(t)$  is pulled out of the time integral. The following approximate expression results.

$$\phi(\omega) = \underline{e}_x(t_0) \cdot \sum_n \iiint dk_{\perp x} dk_{\perp y} dk_{\parallel} E_n(k_{\parallel}, k_{\perp}) \left[ \frac{\sin([\omega_n - \underline{k} \cdot \underline{V} - \omega]T/2)}{[\omega_n - \underline{k} \cdot \underline{V} - \omega]T/2} \right] \quad (5.2)$$

Approximating the quantity in the brackets with a delta function  $\delta(\omega_n - \underline{k} \cdot \underline{V} - \omega)$  and integrating over  $k_x$  yields the following approximate expression:

$$\phi(\omega) = (V \sin \theta)^{-1} \sum_n \iiint dk_{\perp x} dk_{\perp y} dk_{\parallel} (|e_x(t_0)k_{\parallel}/k| + |e_{x\perp}(t_0)k_{\perp x}/k|) E_n(k_{\parallel}, k_{\perp}) \quad (5.3)$$

where  $\underline{e}_x(t_0)$  is broken up into components. Assuming the waves are electrostatic  $\underline{E}$  is rewritten as  $(\underline{k}/k)E$ . The absolute values of the wave vectors is used since phase information is being neglected.

Integrating over the delta function sets  $k_{\perp x}$  equal to

$$(\omega - \omega_n - k_{\parallel} V \cos \theta) / V \sin \theta.$$

Since we are looking for the effect on harmonics caused by a marginally unstable gyrotropic distribution of wave components, the simplest distribution to treat mathematically that contains the pertinent assumptions that  $\Delta k_{\perp 0}/k_{\perp 0}$  and  $k_{\parallel}/k_{\perp}$  are small is given by letting  $E(k_{\parallel}, k_{\perp})$  be proportional to  $\delta(k_{\perp} - k_{\perp 0}) \cdot \delta(k_{\parallel} - k_{\parallel 0})$ . Integrating over the delta functions yield:

$$\phi(\omega' + \Delta \omega) \propto 1 / (k_{\perp} V \sin \phi) \cdot (|e_{x\parallel} k_{\parallel}| + |e_{x\perp} k_{\perp 0} \cos \phi|) / k \quad (5.4)$$

where  $\Delta \omega = k_{\perp 0} \cos \phi \cdot V \sin \theta$ , and  $\phi$  is the azimuthal angle about  $\underline{B}$  measured from the x-axis, and  $\omega' = \omega_n + k_{\parallel 0} V \cos \theta$ . The second term in  $\omega'$  represents the Doppler shift caused by the parallel component of the wave vectors. The  $\Delta \omega$  term is the Doppler broadening of the harmonic. Equation 5.3 indicates that the frequency spectrum is double peaked with each peak located at  $\Delta \omega = \pm k_{\perp 0} V \sin \theta$ .

Equation 5.4 predicts that the separation between the peaks of the double peaked harmonics  $\Delta f$  is given by the following relationship.

$$\Delta f = 2 \cdot V \sin \phi / \lambda \quad (5.5)$$

Therefore if  $\Delta f$  is known, the wavelength  $\lambda$  can be inferred. The distribution used to derive Equation 4 assumes the spread in unstable wavenumbers  $\Delta k_{\perp} = 0$ , but if a finite spread is included Equation 5.5 overestimates the wavelengths. A case where  $\Delta k_{\perp}$  is not equal to zero is given below.

For purposes of estimating the effect of a spread in  $k_{\perp}$ , the following distribution for the amplitude of the waves in  $k$ -space is used:

$$E(k_{\parallel}, k_{\perp}) \sim \exp(-((k_{\perp} - k_{\perp 0}) \Delta k_{\perp})^2) \cdot \delta(k_{\parallel} - k_{\parallel 0}) \quad (5.6)$$

As discussed in Section II, the delta function for  $k_{\parallel}$  is used because  $k_{\parallel}/k_{\perp}$  is small.

A plot of  $|\phi(\Delta \omega)|$  versus  $\Delta \omega / (k_{\perp 0} v_{\text{sat}} \sin \theta)$  when the  $E_x$  antenna is perpendicular to the magnetic field is shown in Figure 31a. Each curve in the plot is for a different value of  $\Delta k_{\perp} / k_{\perp 0}$ . Figure 31b shows a similar plot when the  $E_x$  antenna is parallel to the magnetic field. The double peaked nature of the spectra is apparent in both plots, but the spectral shape of each spectrum is different (separation between the peaks changes and the amplitude between the peaks is different). The spectral shape in Figure 31b cannot be observed because of the 1) the high spin rate of the satellite, and 2) nonlinear effects caused by the logcompressor.

The spin rate of DE-1 limits the time interval when the  $E_x$  antenna is almost parallel to  $\underline{B}$ . The parallel contribution to the spectral

intensity is much smaller (on the order of  $k_{\parallel}/k_{\perp}$ ) than the perpendicular contribution. Therefore, the sampling time available for detection of the parallel contribution is given approximately by  $T_s = 2 \cdot \Theta / \omega_{\text{spin}}$ . The angle  $\Theta = \tan^{-1}(k_{\parallel 0}/k_{\perp 0})$  is the angle the  $E_x$  antenna makes with respect to the magnetic field when the parallel and perpendicular wave components contribute approximately the same intensity to the signal. For the event on June 1, 1984,  $k_{\parallel 0}/k_{\perp 0}$  is probably less than .1 and  $T_s < .2$ s. Substituting  $T_s$  into the uncertainty relationship gives a frequency resolution of  $> 5$  Hz.

To show the effects introduced by the logcompressor, a test signal was generated by the computer with a similar dB level and frequency structure corresponding to the double peaked harmonic emission that occurs on June 1, 1984, at 03:56:20 UT. The test signal was composed of 200 wave modes. All the modes were assigned the same frequency, but each mode was assigned a randomly chosen perpendicular wavenumber, whose amplitude was determined by the Gaussian profile described in Equation 5.6. A plot of the perpendicular wave numbers assigned to the modes is shown in Figure 32. Each mode was also given a small random spread in parallel wave number and a random phase. For this case  $k_{\parallel}/k_{\perp}$  was set equal to .1. From these modes a temporal signal was generated for one satellite spin period that would be detected by the  $E_x$  antenna in the DE-1's reference frame. Figure 33a and 33b are plots of the envelope of the temporal signal before and after compression, respectively. The  $E_x$  antenna is parallel to  $\underline{B}$  at 1.5 s and 4.5 s in the plot.

Nonlinear distortion of the signal by the wideband receiver produces sidebands which transfer spectral power from the peaks to the center of the double harmonics. The sideband generation can be seen by comparing the spectrum shown in Figure 34a with that of Figure 34b, which were generated from the signals shown in Figures 33a and 33b, respectively. The local minimum between the double peaks is almost zero in Figure 33a, whereas Figure 33b has a local minimum similar to that of Figure 29d. The local minimum is not due to enhancement of the signal when  $E_x$  is parallel to the magnetic field, and still persists even when  $k_{\parallel}$  is set equal to zero for all the wave modes.

Table 1 lists the inferred wavelengths and perpendicular phase velocities, determined by measuring the separation of the double peaks for the spectra in Figures 29b-d. Equation 5.5 was used to determine the inferred wave velocities, in which the assumption  $\Delta k_{\perp} = 0$  was made. As shown earlier the inferred phase velocities given in Table 1 are probably slightly overestimated since the spread of unstable wavenumbers  $\Delta k_{\perp}$  was not taken into account. This could account for the discrepancy in the inferred phase velocities, since one would expect the phase velocities to be close to the H<sup>+</sup> thermal velocity.

If  $v_{\phi}$  is approximately  $v_{th,H^+}$  then the separation between the peaks should increase with increasing harmonic number. Since  $\omega_n$  is approximately equal to  $n \cdot \Omega_{H^+}$ , the wavelength is given by the following relation:  $\lambda_n = 2\pi v_{th,H^+} / n \cdot \Omega_{H^+}$ . Unfortunately this behavior is hard to see for the H<sup>+</sup> harmonic emissions that occur on June 1, 1984, since the harmonic numbers of the excited harmonics are large. Figure 35a shows

a spectrum taken on January 15, 1984, where the 3rd through the 7th harmonics are excited. These harmonics clearly show the above frequency effect. Figure 35b shows a plot of the inferred inverse wavelength (using Equation 5.5) versus the center frequency of the excited harmonics shown in Figure 35a. These points lie close to a straight line whose inverse slope should correspond to a H<sup>+</sup> thermal velocity on the order of 153 km/s. Figure 35 is a plot of the log of phase space density versus energy for H<sup>+</sup> during the June 1 wave event. Each curve corresponds to a different range in pitch angle. There is a very hot energetic component and a cold 250 eV component. The 250 eV component is twice the H<sup>+</sup> temperature predicted by the phase velocity (Table 2), which is in good agreement due to the poor energy resolution of the Energetic Ion Spectrometer in the low energy range.

In the above analysis it was assumed that  $V_{\text{flow}}$  is much less than  $V_{\text{sat}}$ . One uncertainty in any method of analyzing the Doppler effect is the determination of the flow velocity of the plasma. Since the static electric field measurements on DE-1 can only make a determination of the flow velocity perpendicular to both the spin plane of the satellite and the magnetic field, there is always some uncertainty in estimating the flow velocity based on electric field data alone. The parallel component of the flow velocity is relatively unimportant to the spreading of the harmonics, but adds a Doppler shift to the spectrum.

In the analysis it was assumed that  $V_{\text{flow}}$  is much less than  $V_{\text{sat}}$ , but if this is not true  $V_{\text{sat}}$  should be replaced by  $|\vec{V}_{\text{sat}} - \vec{V}_{\text{flow}}|$ . The plasma flow velocity is determined primarily by the  $\vec{E} \times \vec{B}$  drift. The

$E_x$  antenna measures a voltage of 5 mV/m during the June 1 event which gives a value of 1.85 km/s for the component of the  $\underline{E} \times \underline{B}$  drift perpendicular to both the magnetic field and satellite velocity. This measurement gives the east-west component of the flow velocity. This flow component alone only changes  $|\underline{V}_{sat} - \underline{V}_{flow}|$  by 7% since  $V_{sat} = 4.82$  km/s.

Unfortunately interference noise on the  $E_z$  antenna makes it impossible to determine the other component of the  $\underline{E} \times \underline{B}$  drift, which is the north-south component perpendicular to  $\underline{B}$ . Along the auroral field lines the north-south component is usually smaller than the east-west component. So using 1.85 km/s as the uncertainty in magnitude of the component which lies in the plane defined by  $\underline{B}$  and  $\underline{V}_{sat}$ , and projecting this component onto  $\underline{V}_{sat}$  gives an uncertainty in determining  $k_{\perp}$  of about 30%.

### C. Spectral Broadening in General

The above discussion of Doppler effects leads to the following question. If Doppler broadening makes a major contribution to the broadening of ion cyclotron waves, why isn't the occurrence of double peaked harmonics the rule instead of the exception? Most ion cyclotron harmonics take on the appearance shown in Figure 6 in which there is no clearly discernable double peak. Furthermore, if Doppler spreading is the dominate broadening mechanism and if  $\lambda_n$  is proportional to  $n^{-1}$  the ratio of the half width of the second harmonic to the half width of the first harmonic should be about 2. Figure 38 shows a histogram of



the ratio of the half width of the second harmonic to that of the first harmonic for a number of ion cyclotron wave events. Clearly the peak in the histogram lies closer to 1 instead of 2. The answer must lie in the fact that other broadening mechanisms play an equally important role.

There are a number of other mechanisms that would contribute to spectral broadening. One such mechanism would be the spatial and temporal coherence of the waves. In general any mechanism that disrupts a wave mode over a time interval  $\Delta t$  will lead to a broadening  $\Delta f$  which is proportional to  $\Delta t^{-1}$ . Figures 38(a-c) show the effect of introducing a phase coherence time (assigning to each wave mode a finite lifetime) into the wave modes that make up the signal. In Figure 38a the phase coherence time is .5s and the double peaked harmonic is clearly detectable. As the phase coherence time is decreased to .1s (Figure 38b), the double peaked harmonics are still detectable but the gap between the peaks is starting to fill. When the phase coherence time is reduced to .025s (Figure 38c), the double peak harmonic disappears leaving a single broadened spectral peak.

## VI. CONCLUSION

A systematic survey of H<sup>+</sup> cyclotron wave events was carried out using data from the DE-1 satellite. The majority of the H<sup>+</sup> cyclotron wave events could be classified into two categories: 1) events in which the excited harmonics occur only below the lower hybrid frequency, and 2) events in which the excited harmonics occur at or above the lower hybrid frequency. Events in the first category were highly correlated with the ion beams, while events in the second category were associated with loss cone distributions. However, the loss cone distributions usually persisted before and after the wave events. Hydrogen cyclotron waves that occurred below the lower hybrid frequency were a factor of 10 to 100 times more powerful than hydrogen cyclotron waves that occurred above the lower hybrid frequency.

The observed spatial distribution of electrostatic H<sup>+</sup> cyclotron wave events corresponded to the statistical auroral oval, exhibiting a strong dusk-dawn asymmetry, with the majority of H<sup>+</sup> cyclotron wave events occurring in the dusk sector. A strong correspondence to the magnetic local time and invariant latitude was found between the occurrence of H<sup>+</sup> cyclotron waves and the occurrence of upflowing ion events observed by the S3-3, which was in a lower orbit than DE-1. A sharp drop off in hydrogen cyclotron wave events occurred below  $2 R_E$ , part of this drop off can be attributed to Doppler broadening of the

spectral peaks. Comparison of hydrogen cyclotron wave event data with  $K_p$  index data indicates that the occurrence of H+ cyclotron waves is independent of magnetic activity.

In a small fraction of H+ cyclotron harmonic events the harmonics were observed to take on a double peaked appearance. In addition it is observed that the separation between the peaks varies, being proportional to the harmonic number. The Doppler effect can explain the observation of double peaked harmonics and their variation in separation with harmonic number. Since double peaked harmonics aren't observed in most ion cyclotron wave events, another broadening mechanism must contribute to spectral broadening.

Table 1  
Parameters Used In Dispersion Relationship

| Species   | $\omega_{pi}$ (Hz) | $\Omega_i$ (Hz)   | $T_i$ (eV) | $V_{di}$ (km/s)   |
|-----------|--------------------|-------------------|------------|-------------------|
| H+        | 66.2               | 32.26             | 50         | 0.0               |
| O+        | 16.5               | 2.0               | 50         | $1.65 \cdot 10^2$ |
| Electrons | $4.0 \cdot 10^3$   | $-5.9 \cdot 10^4$ | $10^3$     | 0.0               |

Table 2  
Measured Perpendicular Phase Velocities of Harmonics

| Harmonic            | $\Delta f$ (Hz) | $f_0$ (Hz) | $\lambda$ (m) | $V_\phi$ (km/s) |
|---------------------|-----------------|------------|---------------|-----------------|
| 03:54:50 03:55:02.5 |                 |            |               |                 |
| 9                   | 20.7            | 382.15     | 362           | 138             |
| 10                  | 23.0            | 424.7      | 326           | 138             |
| 11                  | 23.0            | 466.1      | 326           | 152             |
| 03:55:35 03:55:37.5 |                 |            |               |                 |
| 8                   | 16.6            | 336.2      | 452           | 152             |
| 9                   | 22.1            | 378.95     | 338           | 128             |
| 10                  | 16.1            | 417.85     | 446           | 194             |
| 03:56:20-03:56:32.5 |                 |            |               |                 |
| 10                  | 23.0            | 407.8      | 326           | 134             |

$$\theta = 51.115^\circ \quad V_{\text{sat}} = 4.82 \text{ km/s} \quad \lambda = 2V_{\text{sat}} \cdot \sin\theta / \Delta f$$

$\Delta f$  is the separation between the split harmonic peaks.

Figure 1      This figure shows a plot of the orientation of the satellite orbit in the orbital plane at two different times. One orbit occurred on January 4, 1984, and the other orbit occurred on May 24, 1984. The fuzzy trace on each of the orbits corresponds to the detection of electrostatic H<sup>+</sup> cyclotron waves by the DE-1 satellite. The lines that intersect the Earth's surface (at geographic latitudes of 65° and 85° in both hemispheres) are magnetic field lines.

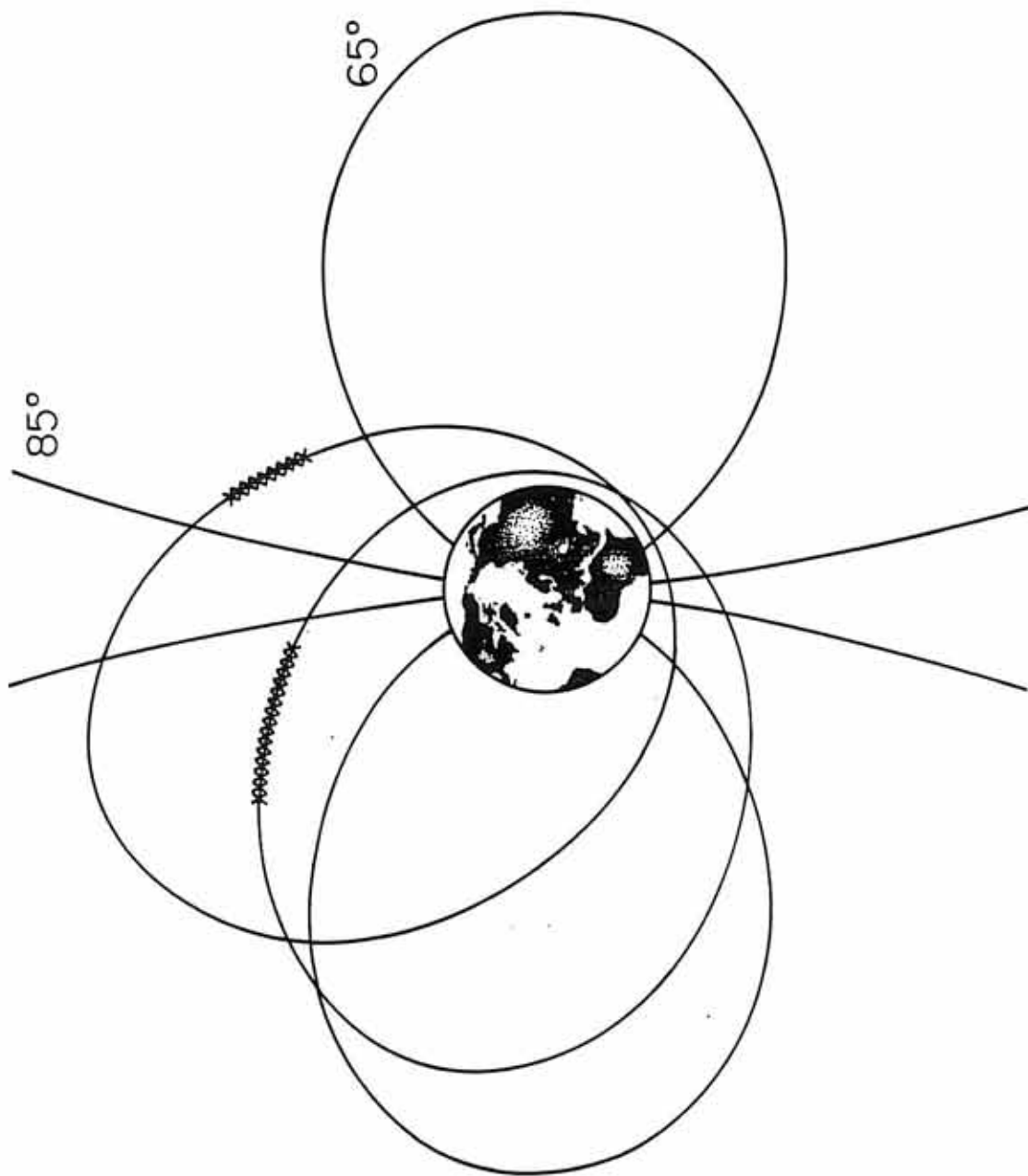
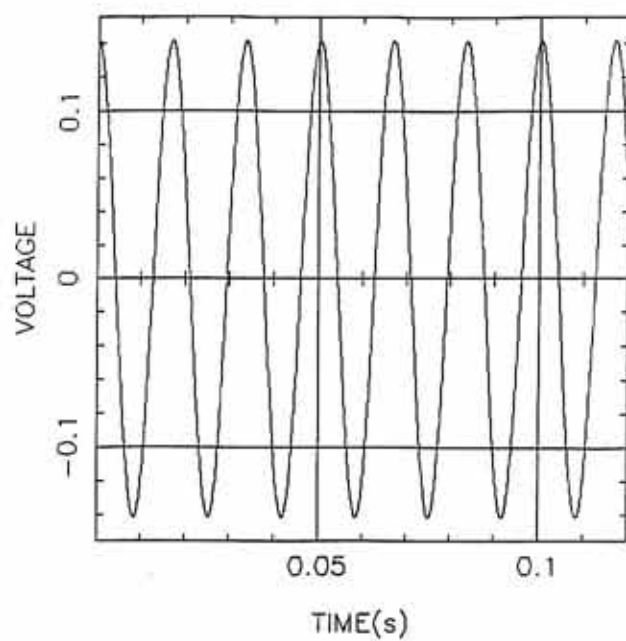


Figure 2      This figure (a) shows the sine wave input signal before compression, and (b) is the resulting compressed output signal.



(a) INPUT SIGNAL



(b) COMPRESSED SIGNAL

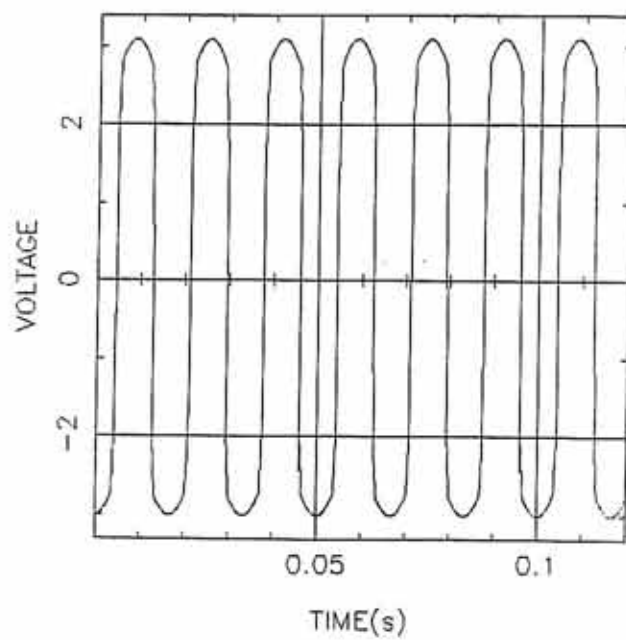


Figure 3      This figure (a) shows the spectrum of the input signal which is composed of two frequency components, and (b) is the spectrum of the resulting compressed signal. Figure 3c is the spectrum of the input signal which is composed of four frequency components, and (d) is the corresponding spectrum of the compressed signal.

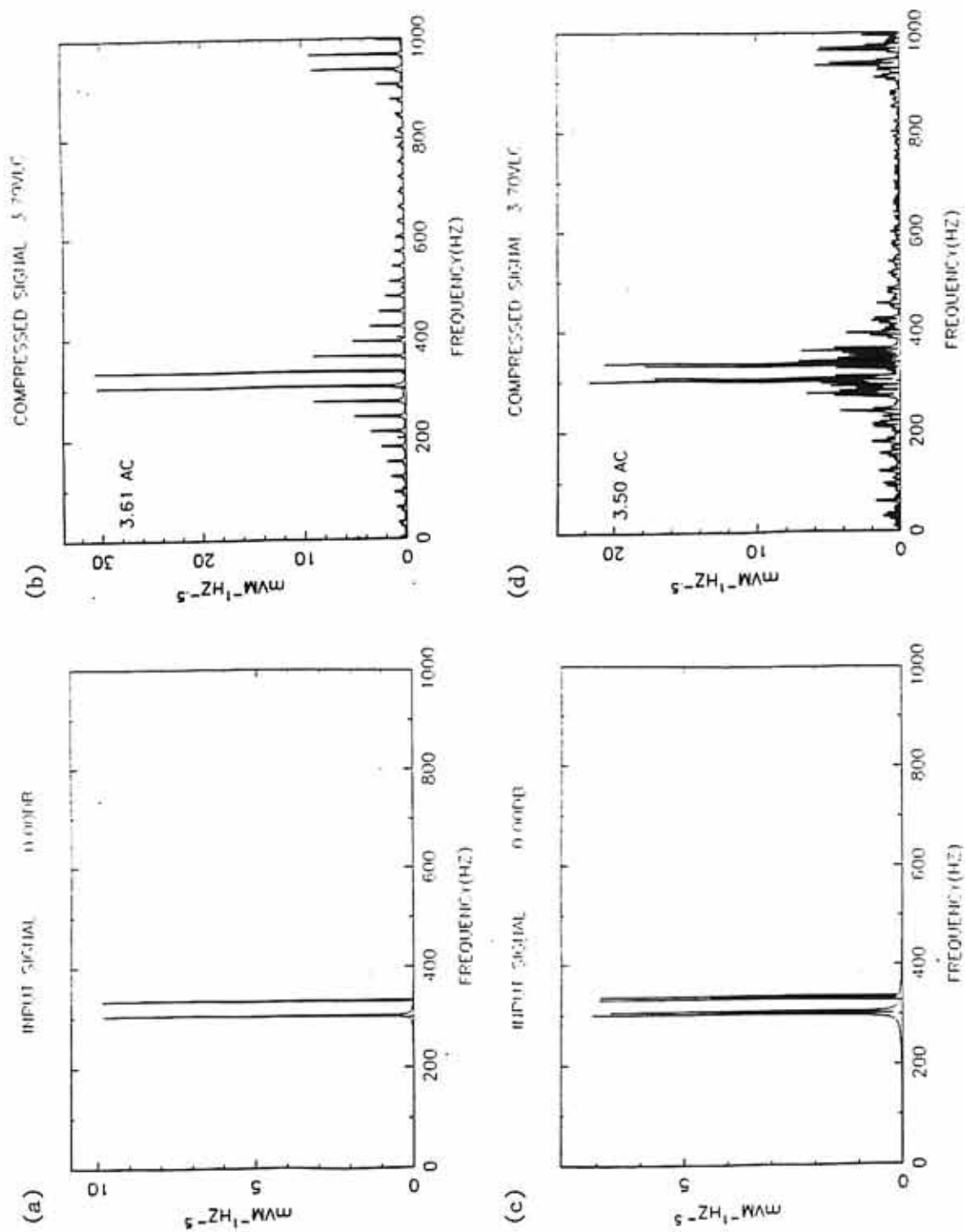


Figure 4      In this figure (a) is the spectrum of a more complex input signal, and (b) is the spectrum of the resulting output signal. Figure 4c is the spectrum of a more complex input signal, and (d) is the spectrum of the resulting output signal.

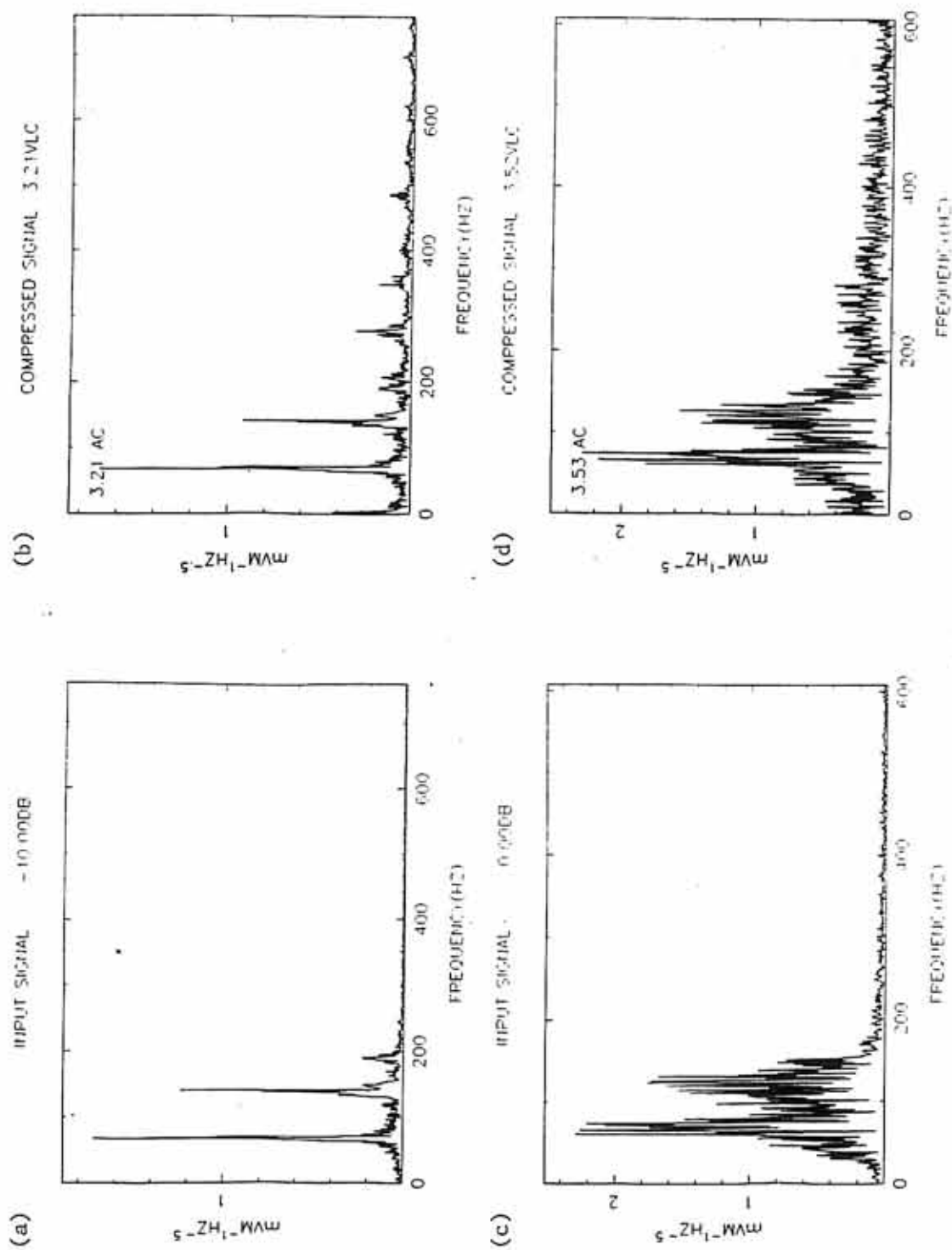


Figure 5      This figure is a spectrum of an EIC event that occurred at 14:38:54 UT on January 4, 1984, the evenly spaced vertical lines are located at integer multiples of the local  $H^+$  cyclotron frequency.

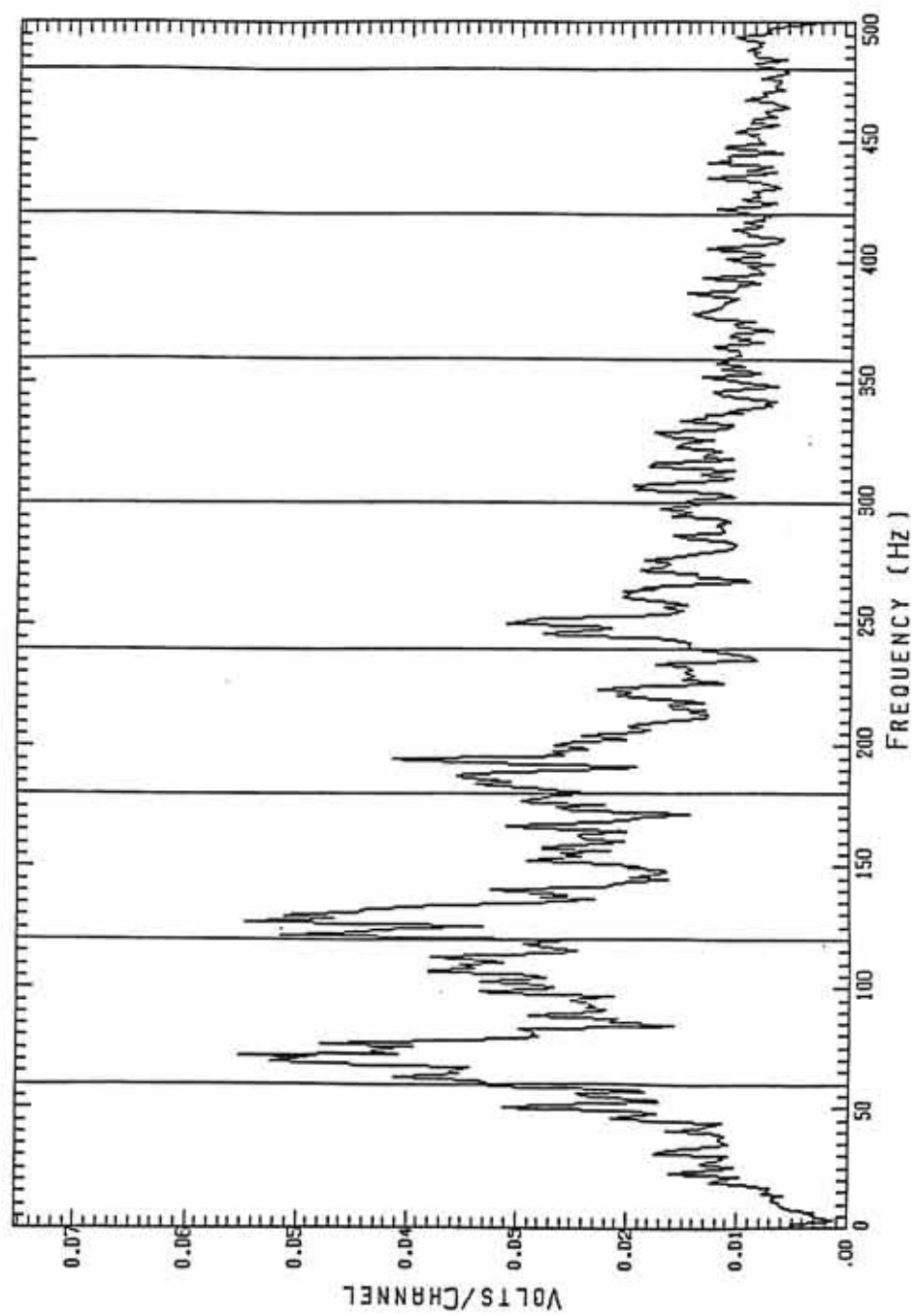


Figure 6      This figure is a spectrum of an IHC event that occurred at 07:19:35 UT on June 15, 1984, the evenly spaced vertical lines are located at integer multiples of the local H<sup>+</sup> cyclotron frequency. The fourth and eleventh harmonics are excited.



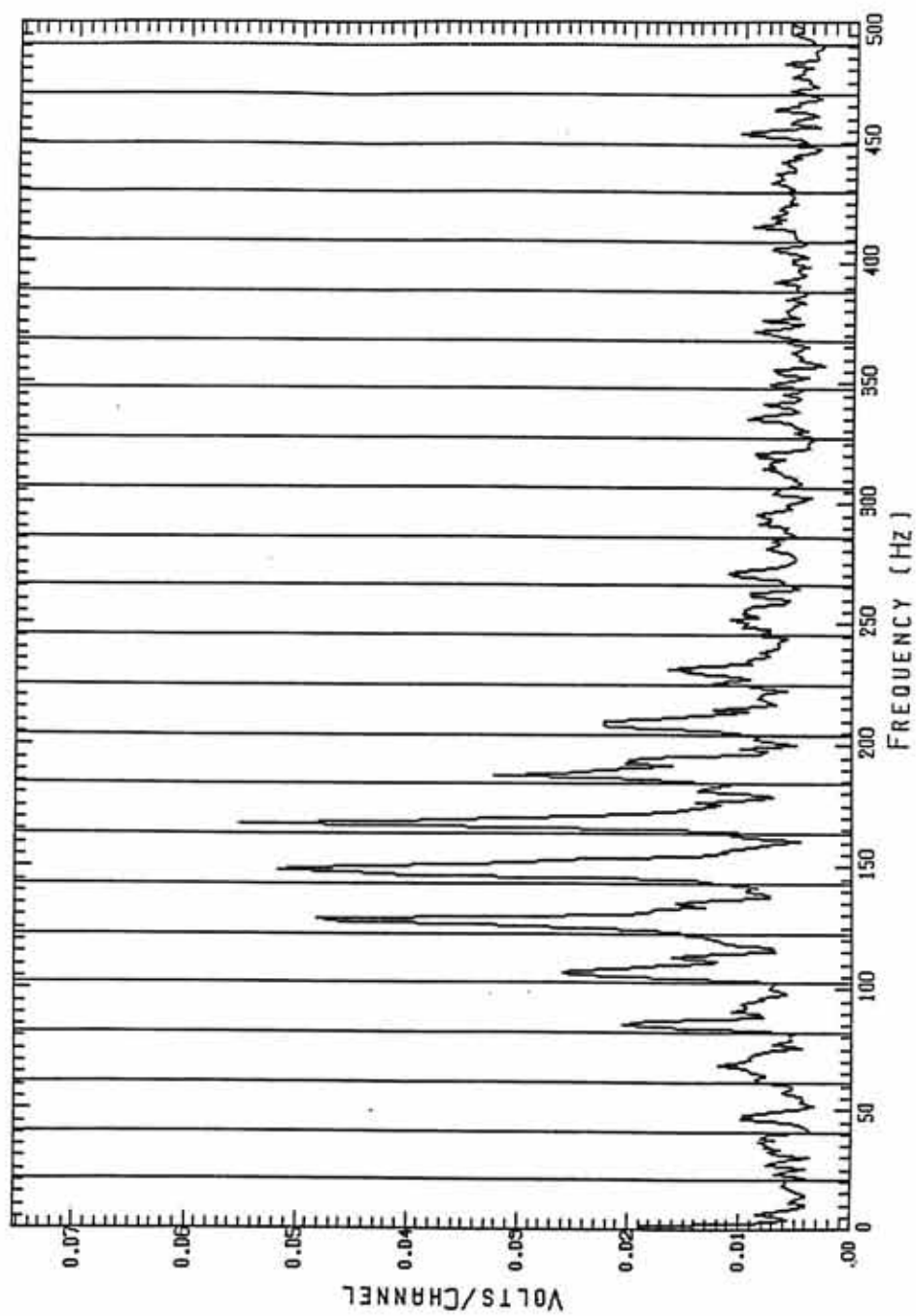


Figure 7      This figure is a spectrogram of the EHC event that occurred on May 24, 1984, from 04:16 UT to 04:32 UT.

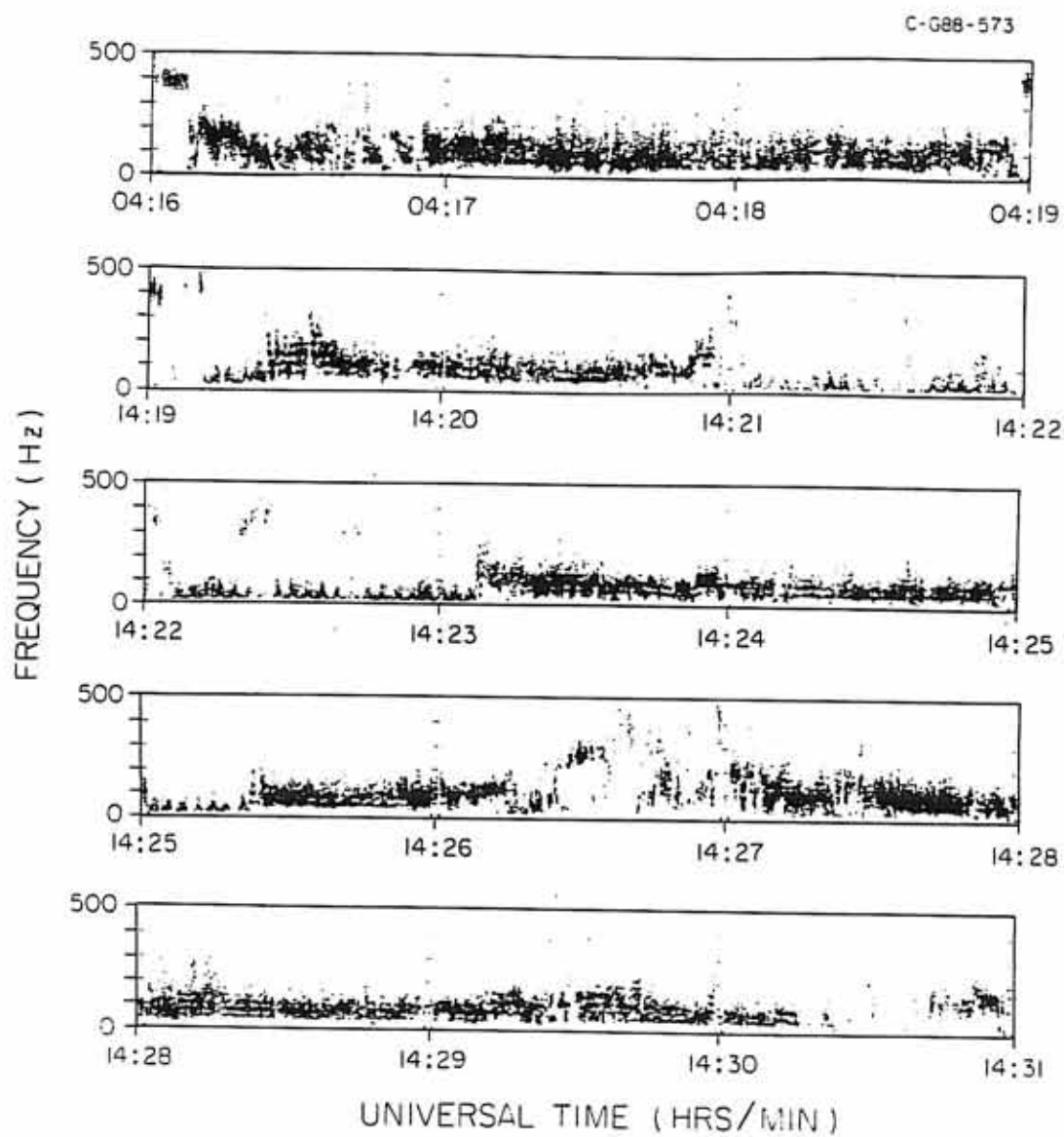


Figure 8      This figure is a spectrum taken at 04:25:46 UT on May 24, 1984, showing the fundamental slightly above the H<sup>+</sup> cyclotron frequency and a small number of harmonics.

ICH58.DAT TO ICH59.DAT MOD 35.80HZ

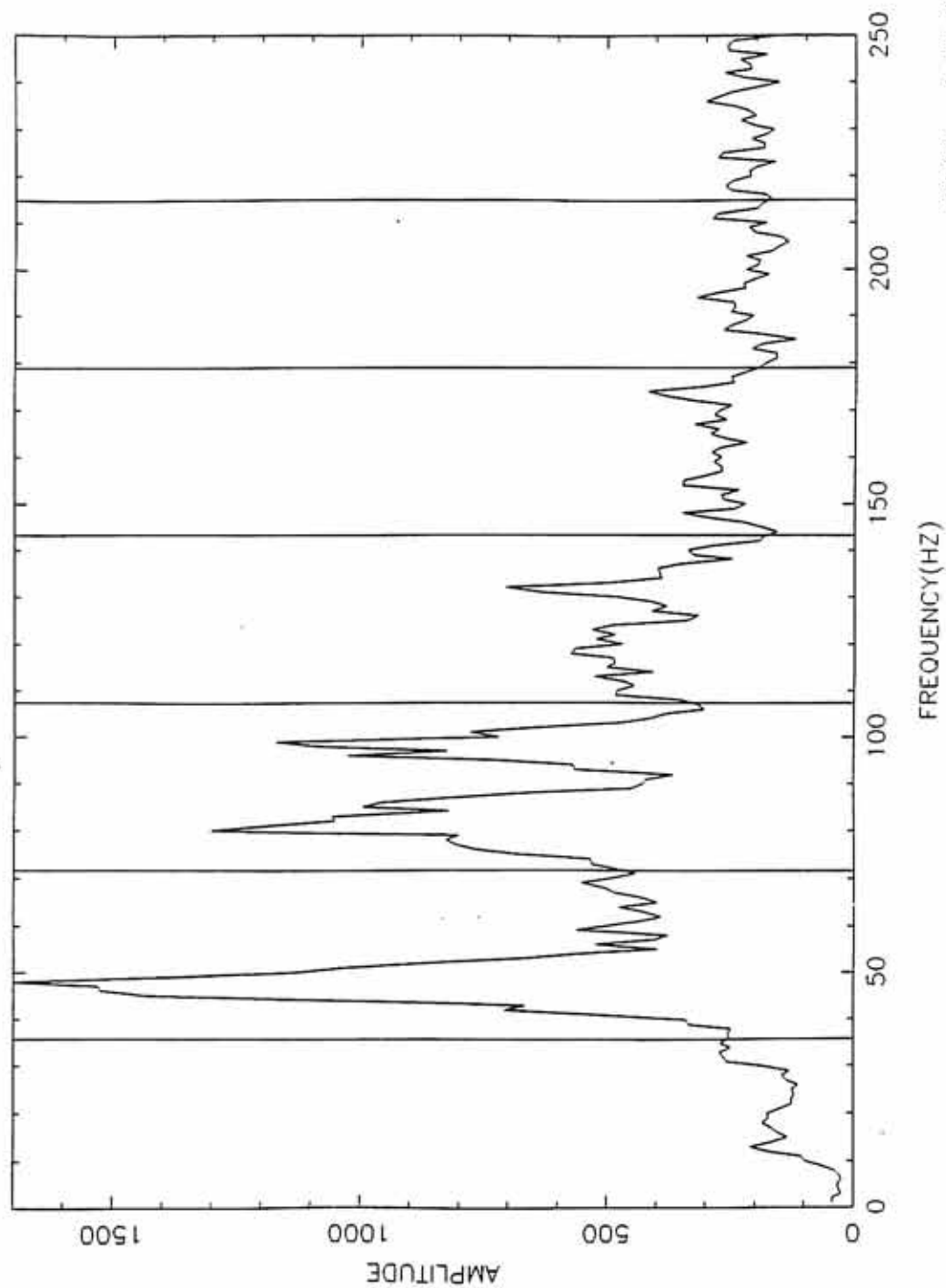
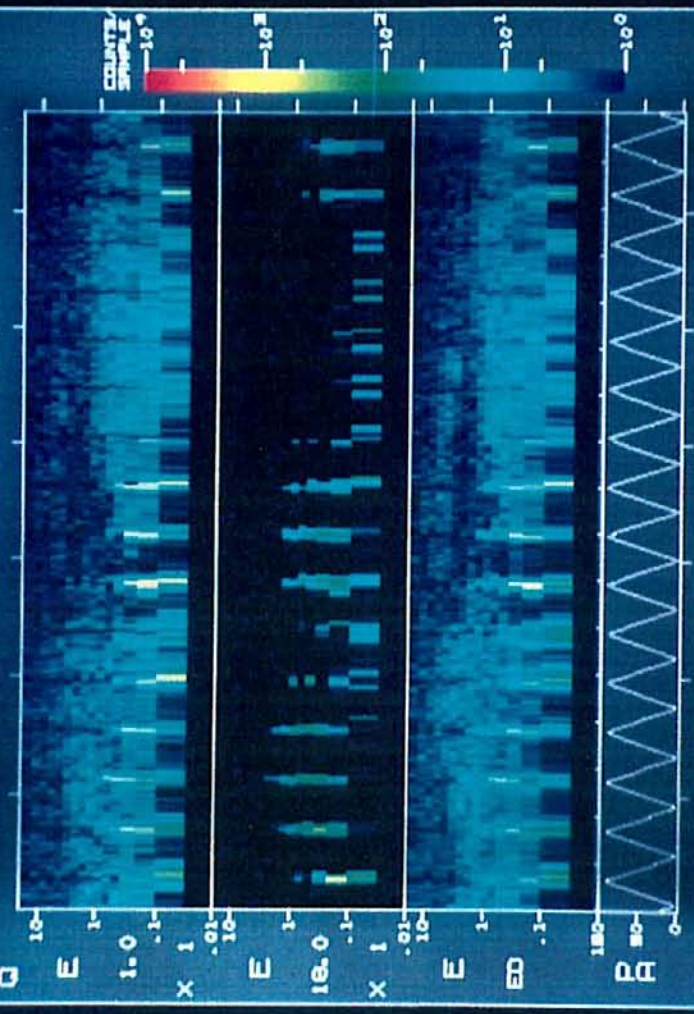


Figure 9      In this figure is a plot of H<sup>+</sup> and O<sup>+</sup> particle flux recorded by Energetic Ion Composition Spectrometer in the 0-1 keV energy range as a function of time and pitch angle that occurred from 4:16 UT to 4:32 UT on May 24, 1984.

DATA B4145  
MAY 24, 1984

PROCESSED  
21:56 APR 11, 1985

# EICS FAST MODE



|     |      |      |      |
|-----|------|------|------|
| UT  | 0418 | 0420 | 0422 |
| MLT | 1658 | 1651 | 1644 |
| INW | 75.8 | 76.6 | 77.5 |
| FE  | 2.73 | 2.78 | 2.84 |

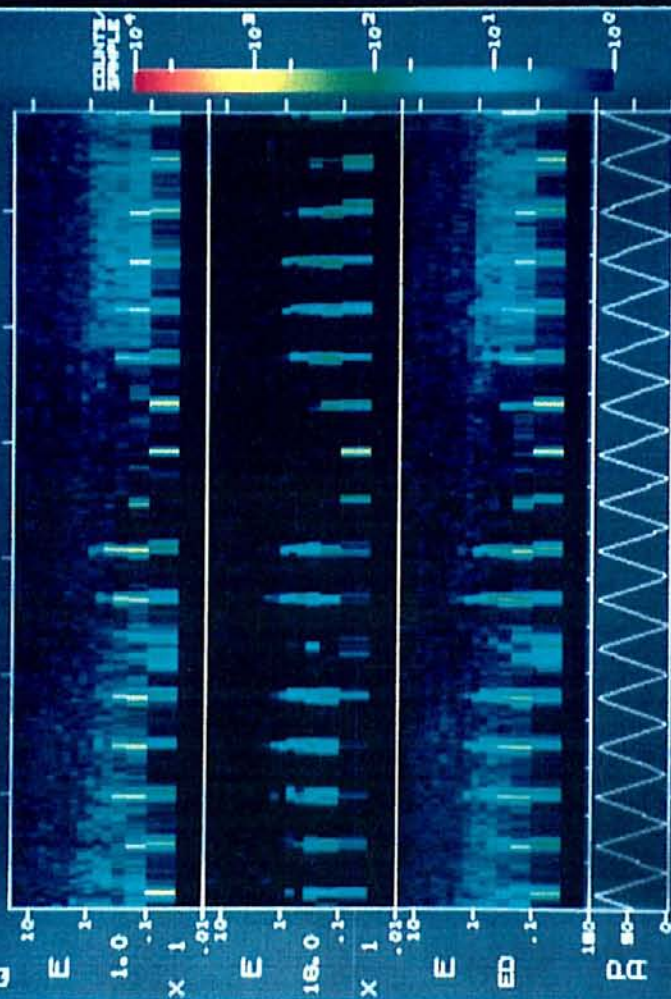
Figure 10     In this figure is a plot of H<sup>+</sup> and O<sup>+</sup> particle flux recorded by Energetic Ion Composition Spectrometer in the 0-1 keV energy range as a function of time and pitch angle that occurred from 4:16 UT to 4:32 UT on May 24, 1984.



DATA 84145  
MAY 24, 1984

PROCESSED  
22:03 APR 11, 1985

ETICS FAST MODE



UT MLT INW RE

Figure 11      This figure is a plot of the rms electric field recorded by the  $E_x$  antenna during the time interval from 04:16 UT to 04:32 UT on May 24, 1984, note the strong correspondence of local minimums in power with the disappearance of EHC wave during the interval.

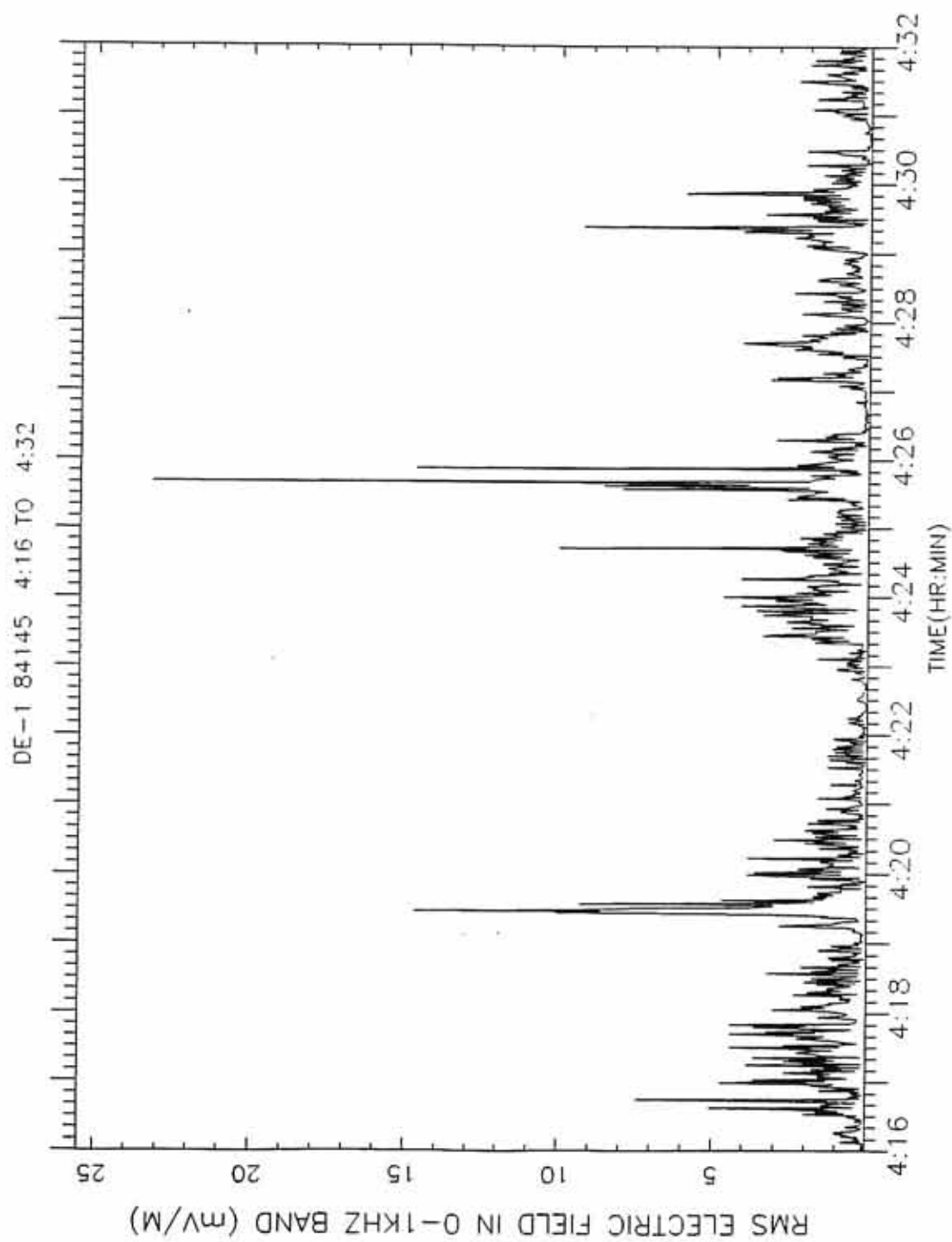


Figure 12      This figure is a wideband spectrum taken at 10:40:46 UT on January 15, 1984, the evenly spaced lines are located at integer multiples of the local H<sup>+</sup> cyclotron frequency.

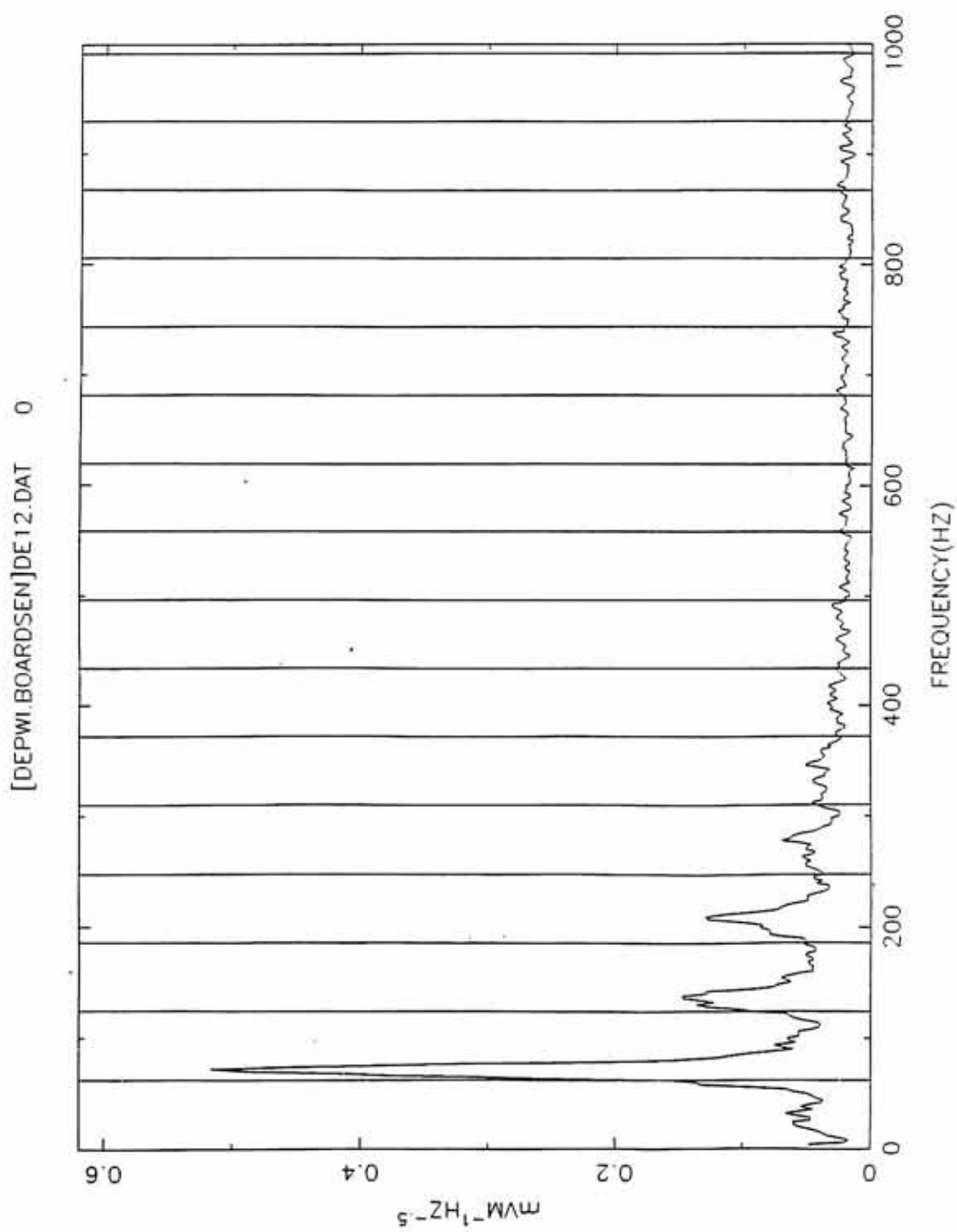


Figure 13     In this figure (a,b) are contour plots of the corresponding  $O^+$  and  $H^+$  velocity space distributions measured around 10:40 UT on January 15, 1984. The solid contours are spaced at the decade intervals of the phase space density measured in units of  $s^3 km^{-6}$ . The dashed curves are at half decade intervals. Particles with a positive parallel velocity are flowing toward the ionosphere. The axes are labelled in units of km/s.

EICS

M/Q= 16.0

ESA

JAN 15. 1984

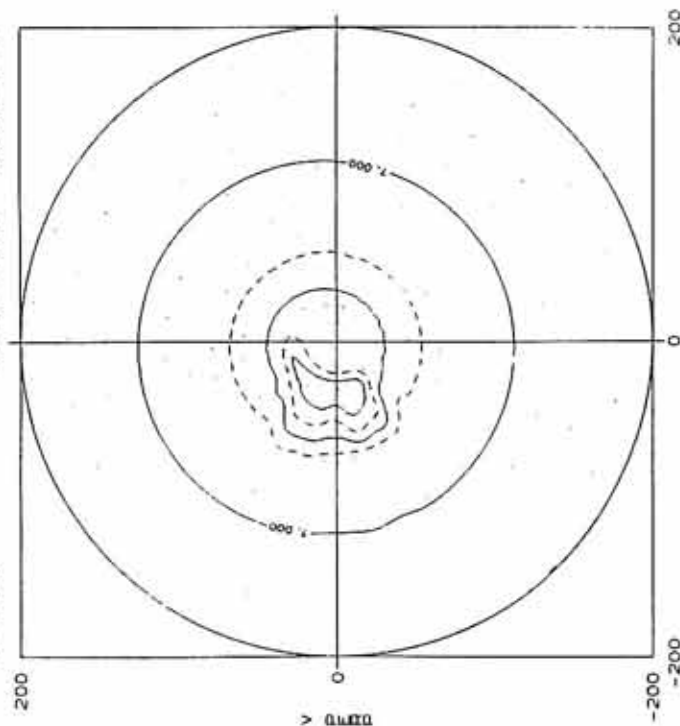
10: 43: 34

10: 43: 52

84015

38614308

38632244



(a)

EICS

M/Q= 1.0

ESA

JAN 15. 1984

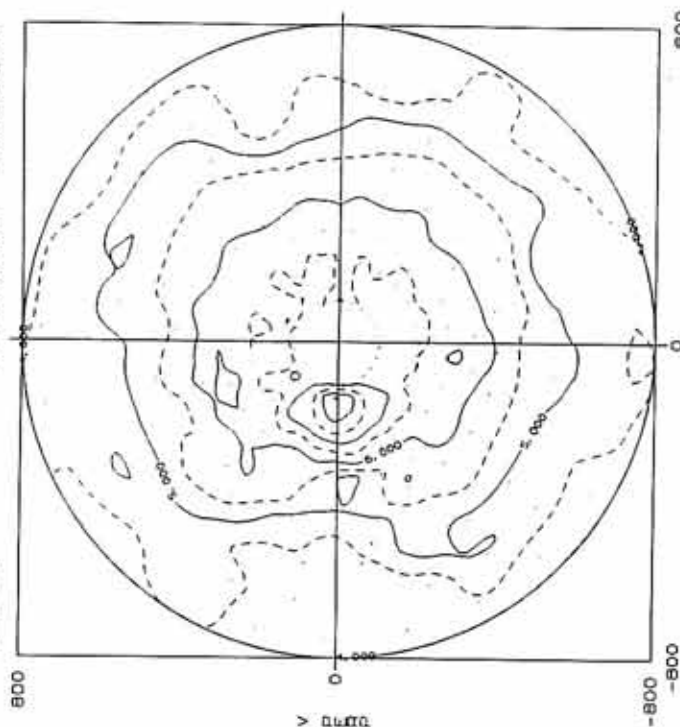
10: 40: 40

10: 40: 58

84015

38440304

38458244



(b)

Figure 14      This figure is the dispersion relationship for an  $H^+$  beam streaming through an  $O^+$  beam similar the the beams shown in Figure 12 which indicates that the EHC waves are damped and therefore  $H^+$  background is probably needed. The negative of the damping rate is plotted (dashed curve).



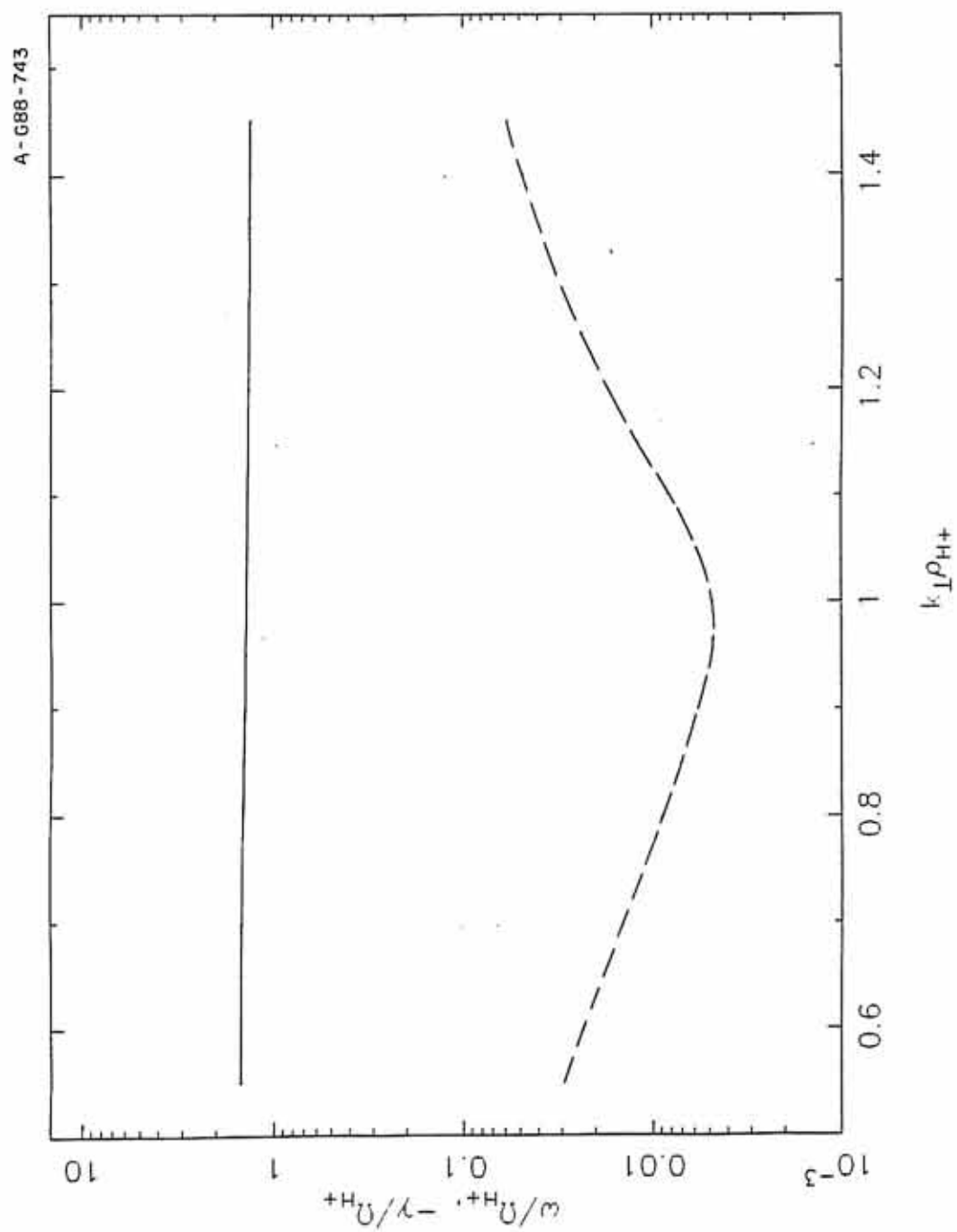


Figure 15      This figure is a plot of rms electric field detected in the 1 kHz band for electrostatic ion cyclotron wave events versus geocentric Earth radii (in units of  $R_E$ ).

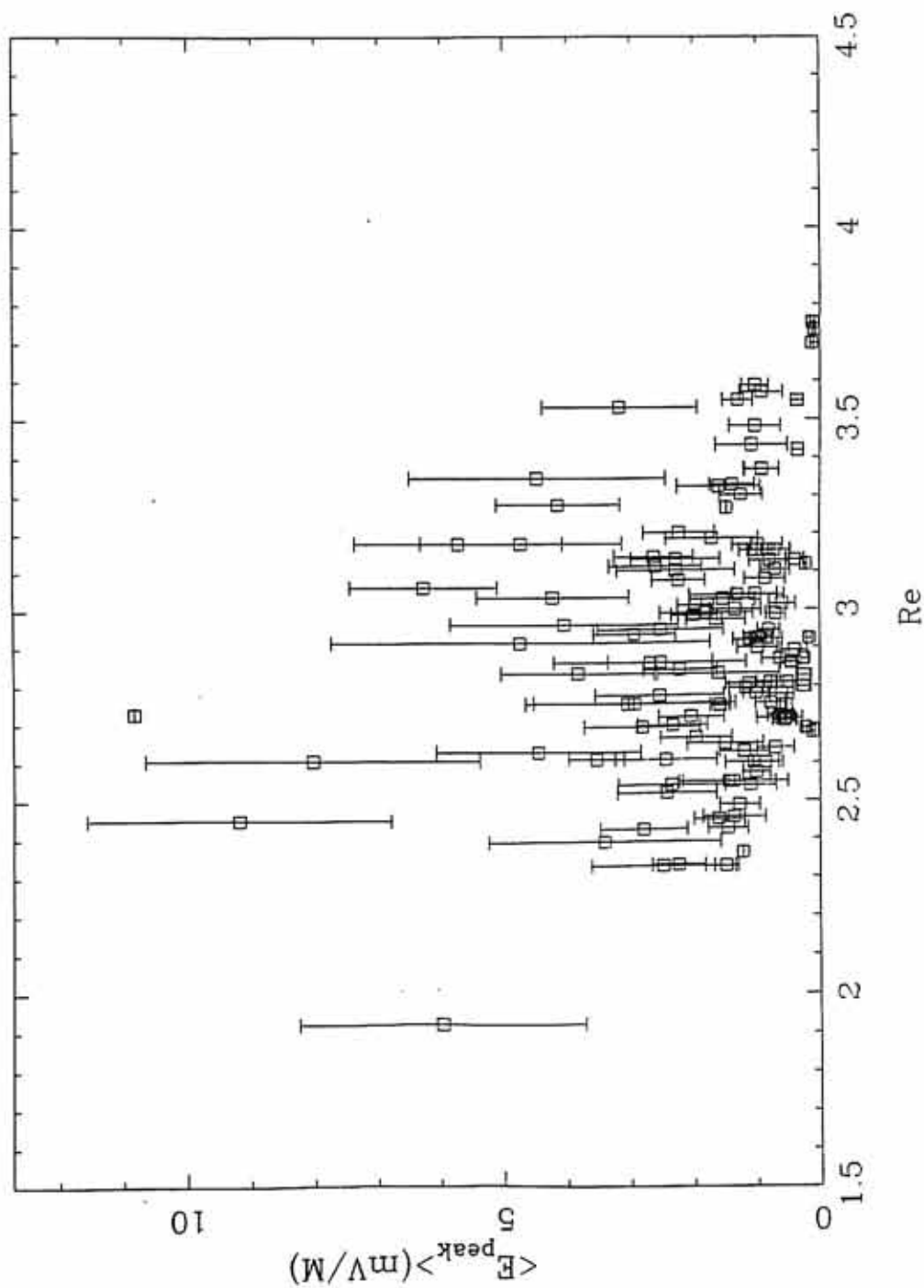
Electrostatic H<sup>+</sup> Cyclotron Wave Events

Figure 16      This figure is a spectrogram of an H<sup>+</sup> cyclotron harmonic event that occurred at 10:45 UT on day 15 of the year 1984.

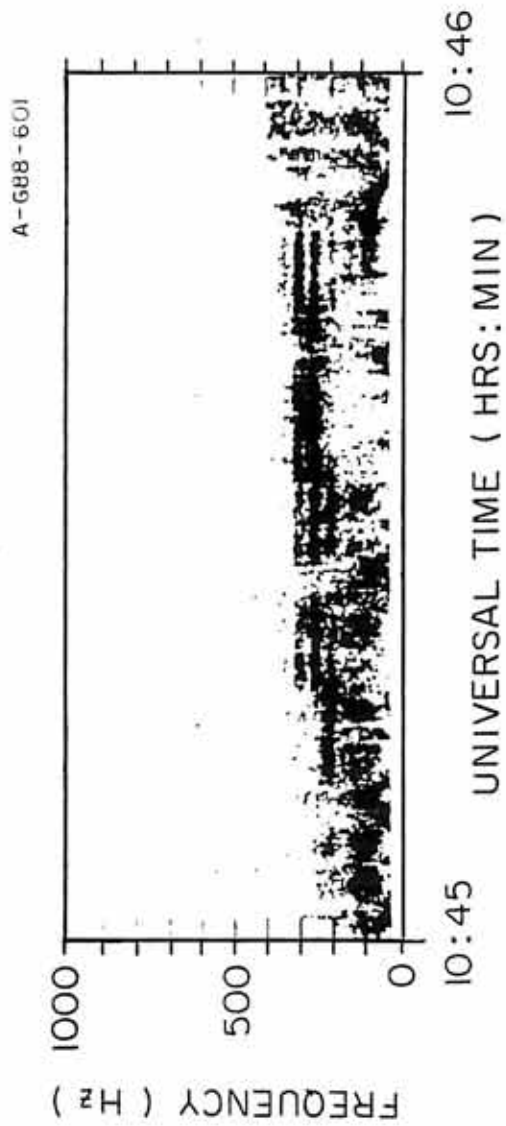


Figure 17 This figure is a plot of  $H^+$  distribution function measured by EICs on June 12, 1984, at 10:45:28-46 UT. Note the loss cone feature flowing up the field line in the data. The solid contours are spaced at the decade intervals of the phase space density measured in units of  $s^3 km^{-6}$ . The dashed curves are at half decade intervals. Particles with a positive parallel velocity are flowing toward the ionosphere. The axes are labelled in units of km/s.

EICS

M/Q= 1.0

ESA

JAN 15. 1984

10:45:28

10:45:46

84015

38728308

38746244

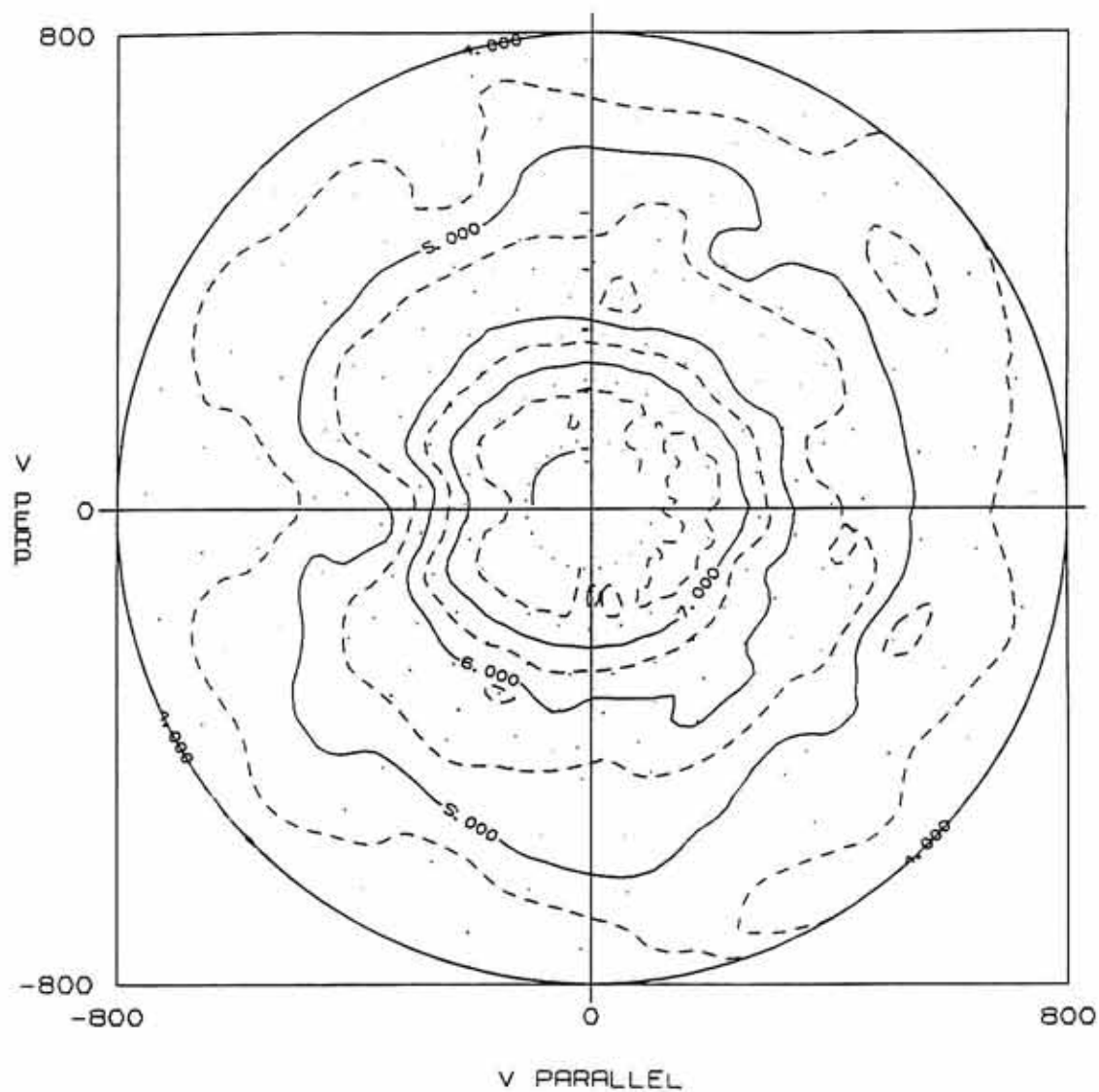


Figure 18 This figure is a plot of rms electric field detected in the 1 kHz band for ion cyclotron harmonic events versus geocentric Earth radii (in units of  $R_E$ ).



## H+ Cyclotron Harmonic Wave Events

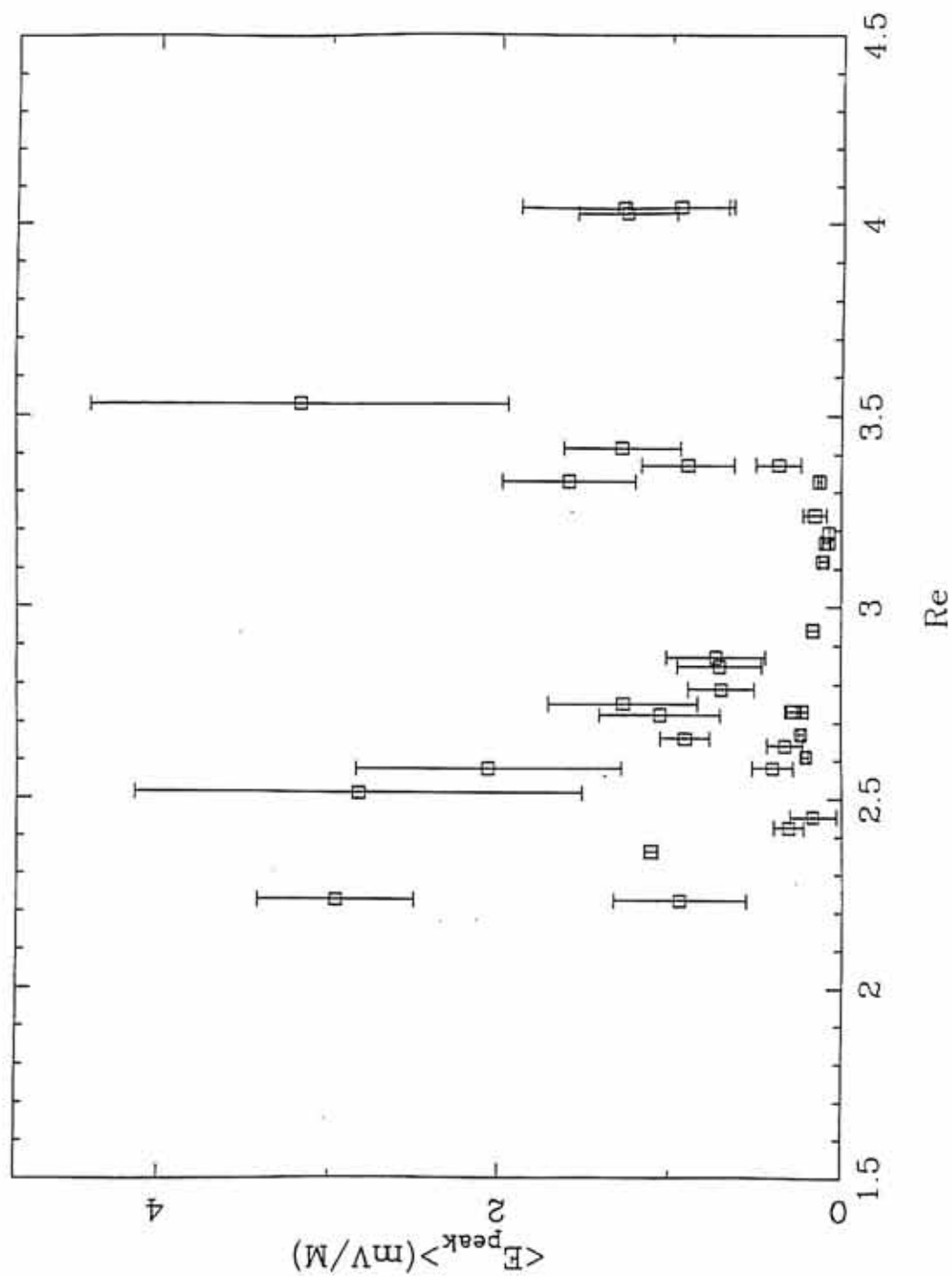
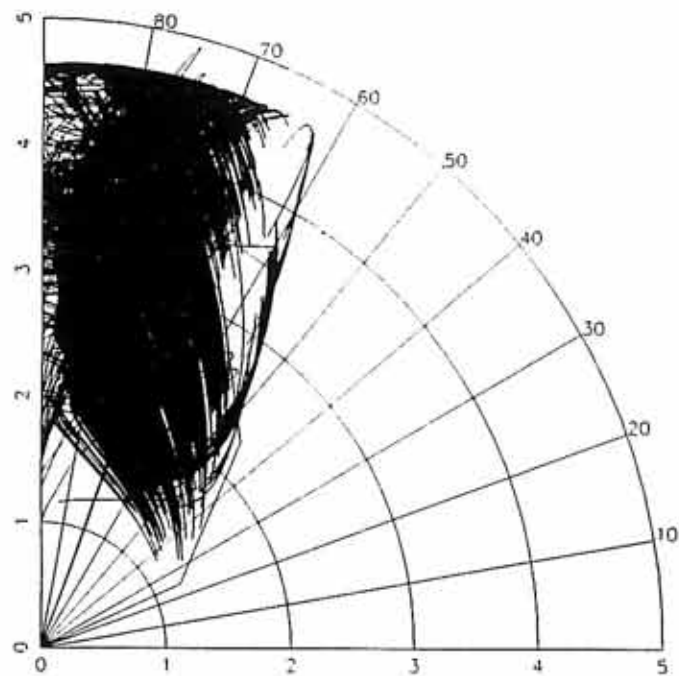


Figure 19      This figure (a) shows a plot of the satellite orbit coverage when the wideband receiver was on as a function of geocentric Earth radii and invariant latitude, and (b) is a similar plot to (a) of orbit coverage when ICW events were detected.

(a)



(b)

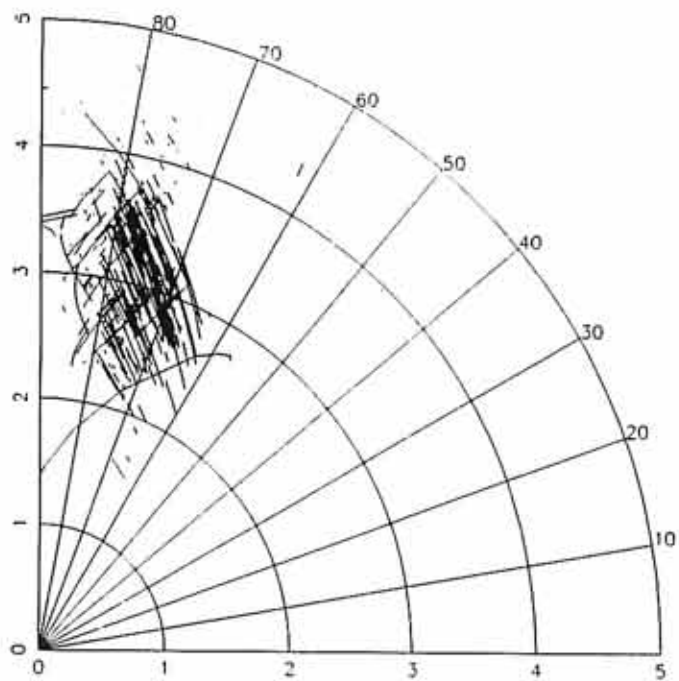


Figure 20      This figure (a,b) shows plots of the halfwidths normalized by the local  $H^+$  cyclotron frequency for the (a) fundamental and the (b) second harmonic of a sample of electrostatic  $H^+$  cyclotron wave events.

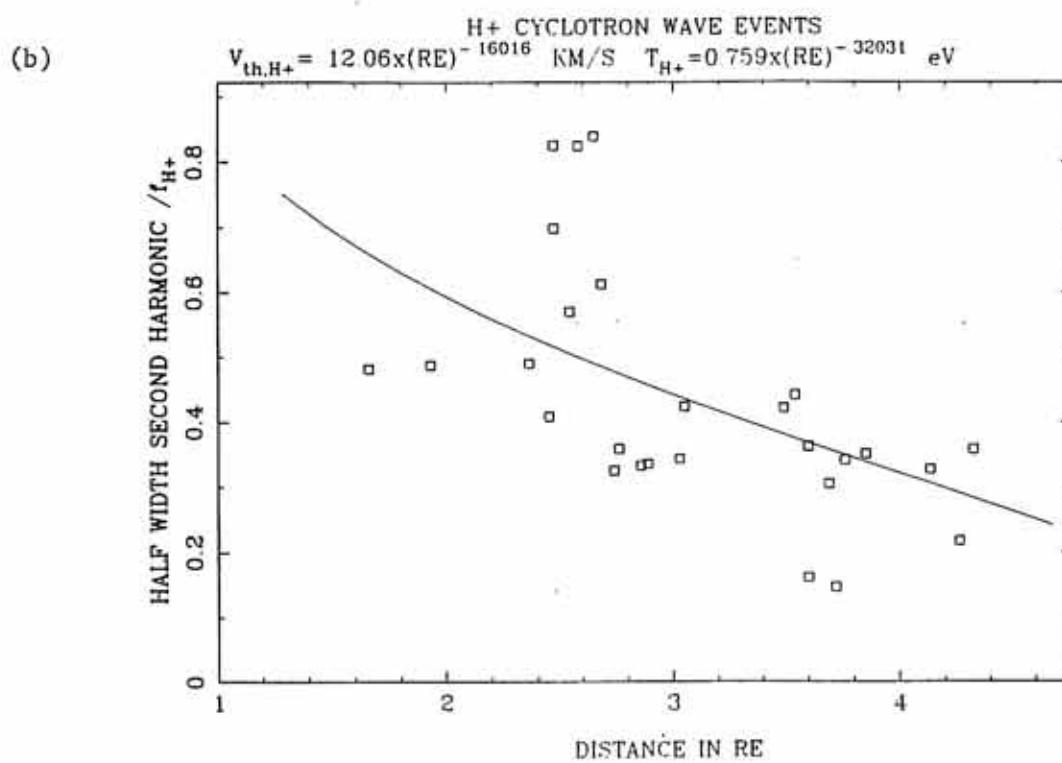
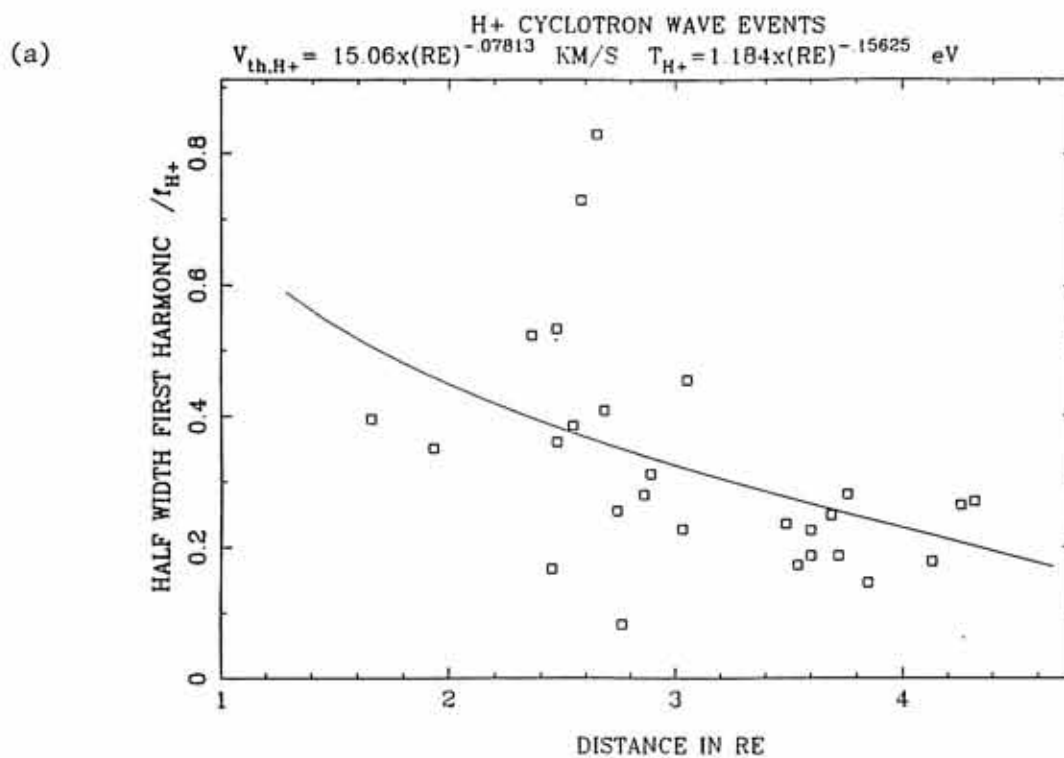
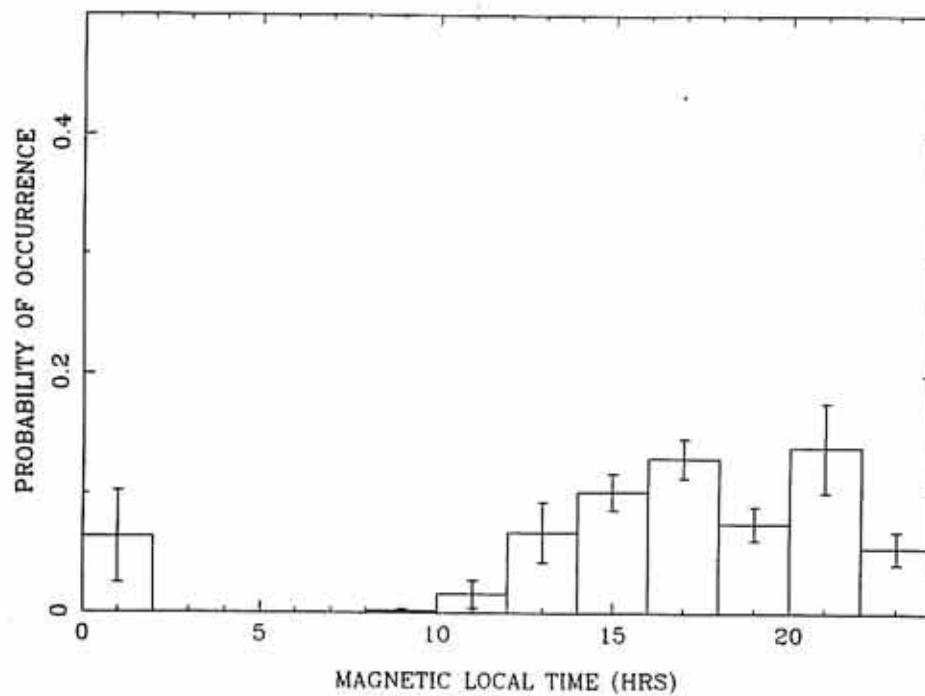


Figure 21     In this figure (a) is a plot of the occurrence of ion cyclotron waves between 2  $R_E$  and 4  $R_E$  and 60° and 80° invariant latitude versus magnetic local time, and (b) is reproduced from Figure 3 in Ghielmetti et al. [1978] and is a plot of the relative occurrence of upflowing ion beam events versus magnetic local time in the auroral oval.

(a)

2-4RE 60° TO 80° INVARIANT LATITUDE



BOARDSEW 22-AUG-1988 18:00

(b)

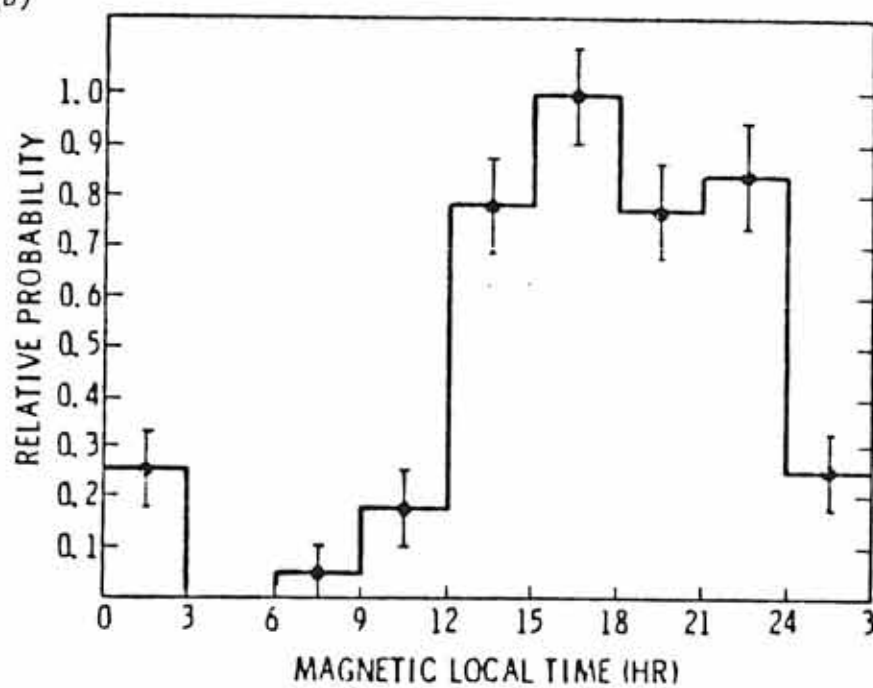
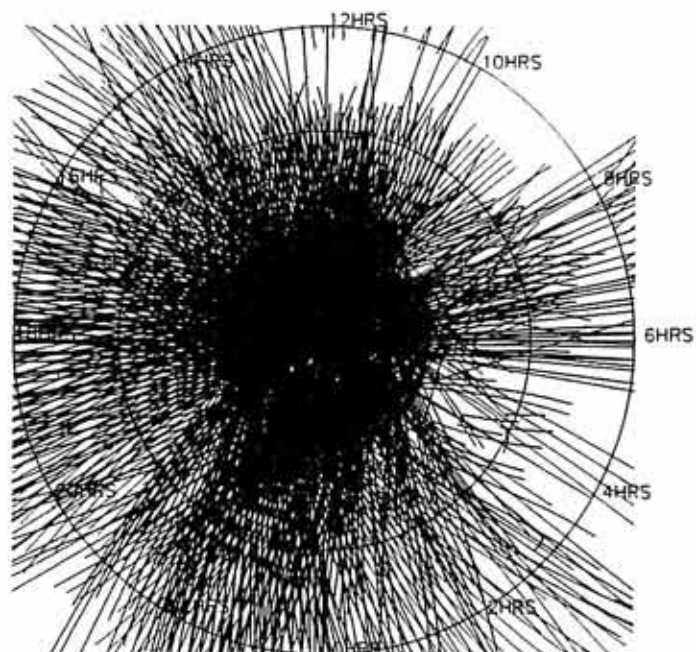


Figure 22      This figure (a) shows a plot of satellite orbit coverage when the wideband receiver is on as a function of invariant latitude and magnetic local time, while (b) is a similar plot of orbit coverage when ICW events are observed. The circles are separated by  $10^\circ$  invariant latitude.



(a)



(b)

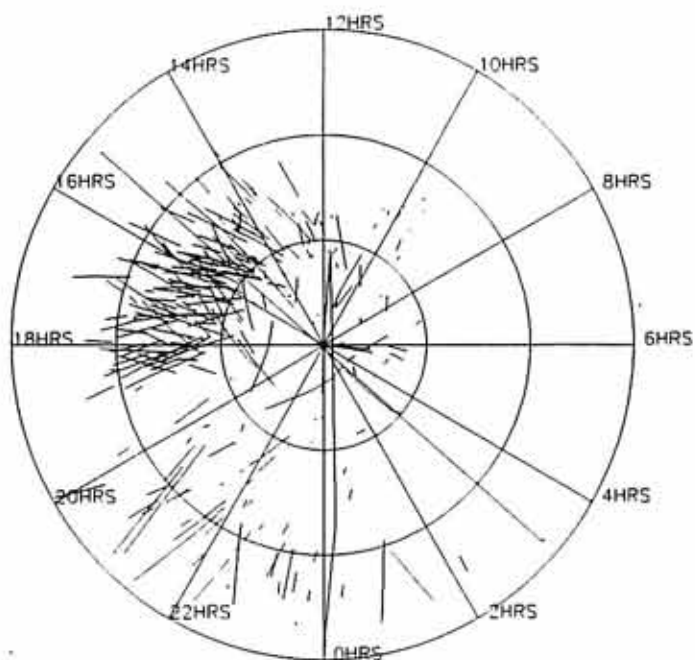
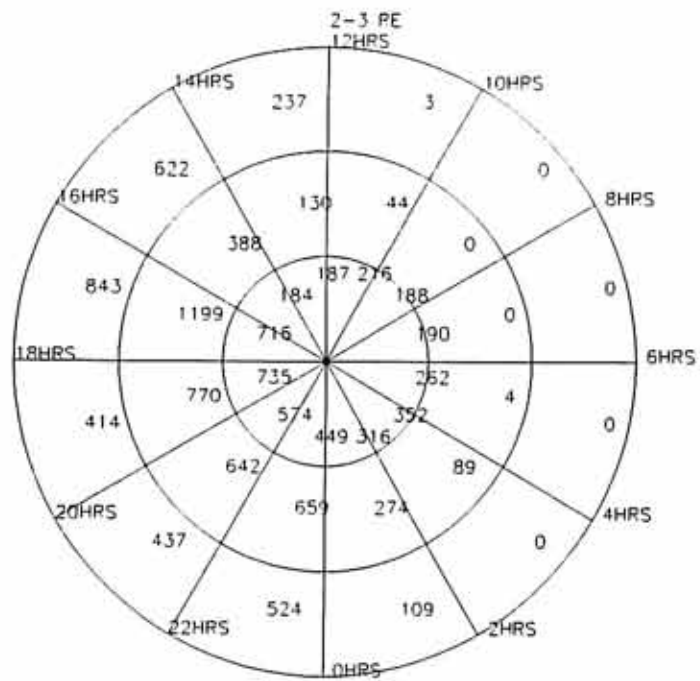


Figure 23 In this figure (a) is a plot giving the total time in minutes the wideband instrument was on in each bin between 2 and 3 Earth radii and (b) is a plot giving the total time in minutes the wideband instrument was on in each bin between 3 and 4 Earth radii.

(a)



(b)

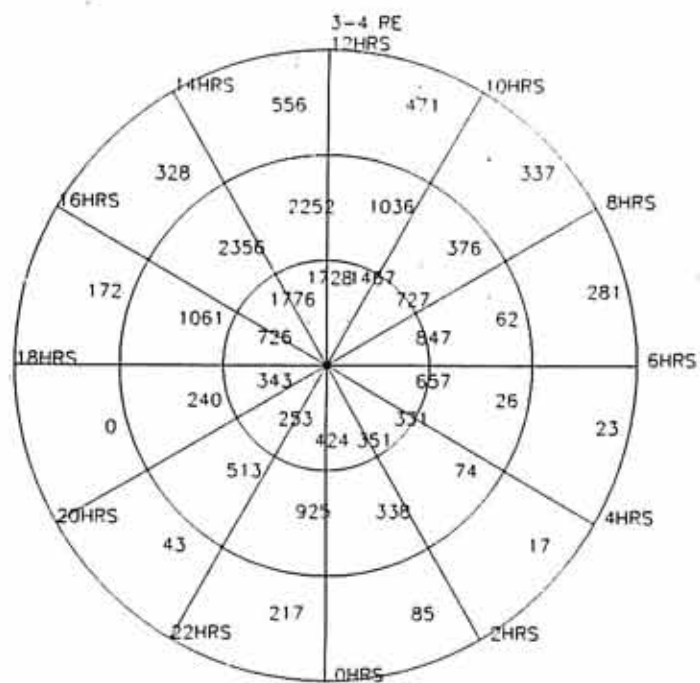
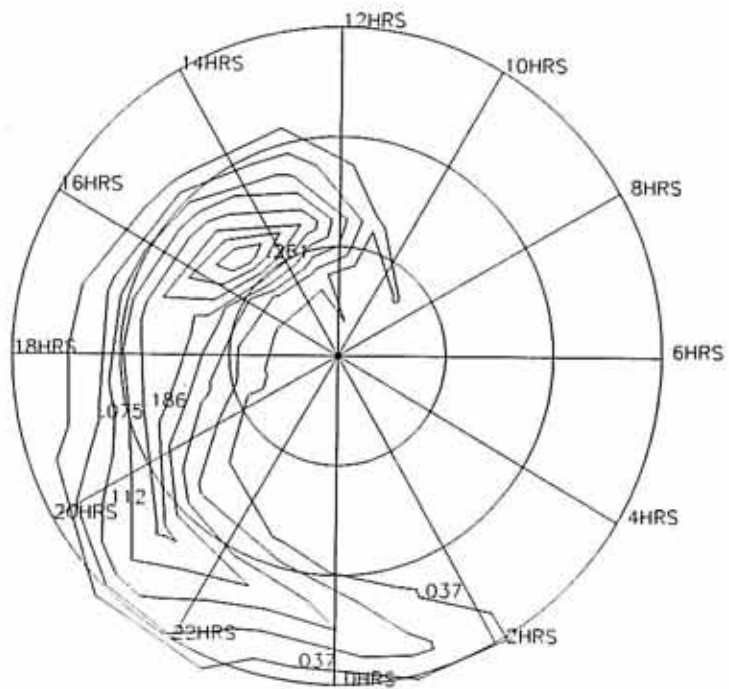


Figure 24      In this figure (a,b) are contour plots made from the binned observations of ion cyclotron waves normalized by wideband receiver ontime in each bin, (a) is a probability of occurrence plot as a function of magnetic local time and invariant latitude for observations between 2 and 3 Earth radii, and (b) is a probability of occurrence plot as a function of magnetic local time and invariant latitude for observations between 3 and 4 Earth radii.

(a)



(b)

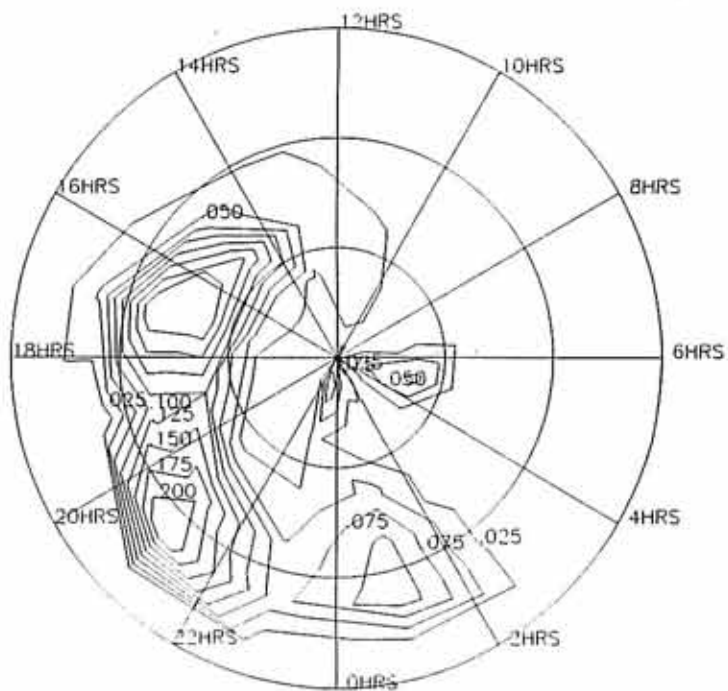


Figure 25      This figure (a) is reproduced from Figure 6 in Hoffman and Lin [1980] and is a plot of electron energy versus magnetic local time for inverted V events, while (b) is reproduced from Figure 4 in Hoffman and Lin and is a plot of the occurrence of inverted V events as a function of magnetic local time and invariant latitude.

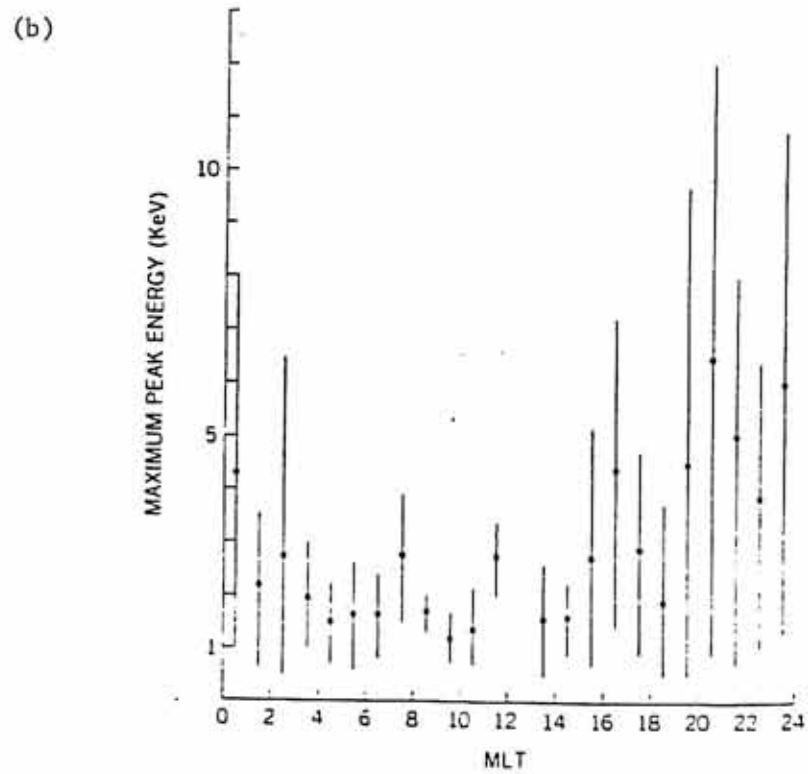
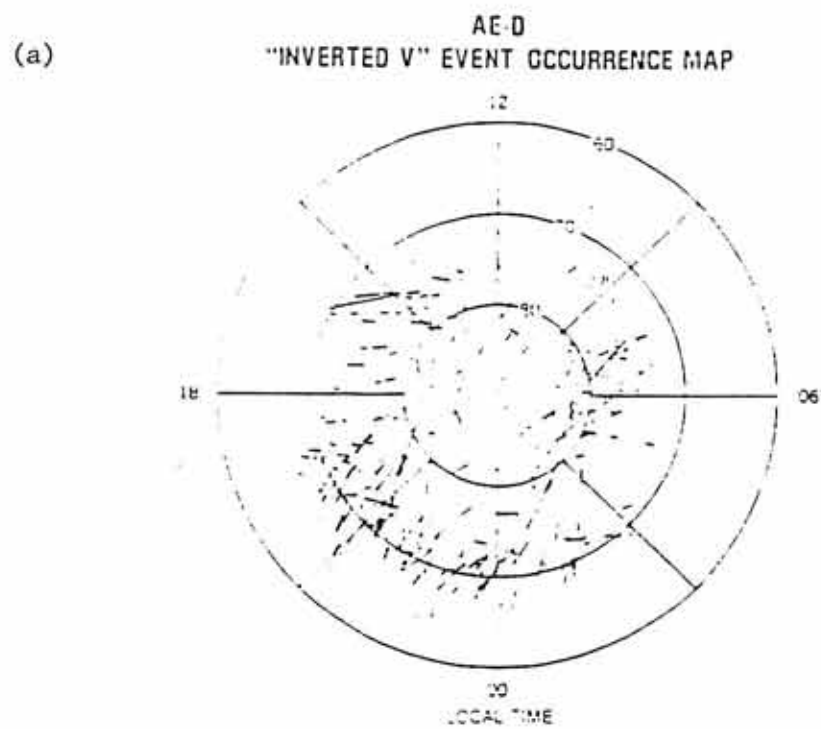


Figure 26      This figure (a) is a plot of the distribution of  $K_p$  values for the year of 1984, while (b) is a plot of the distribution of  $K_p$  values when ion cyclotron wave events are occurring.



(a)

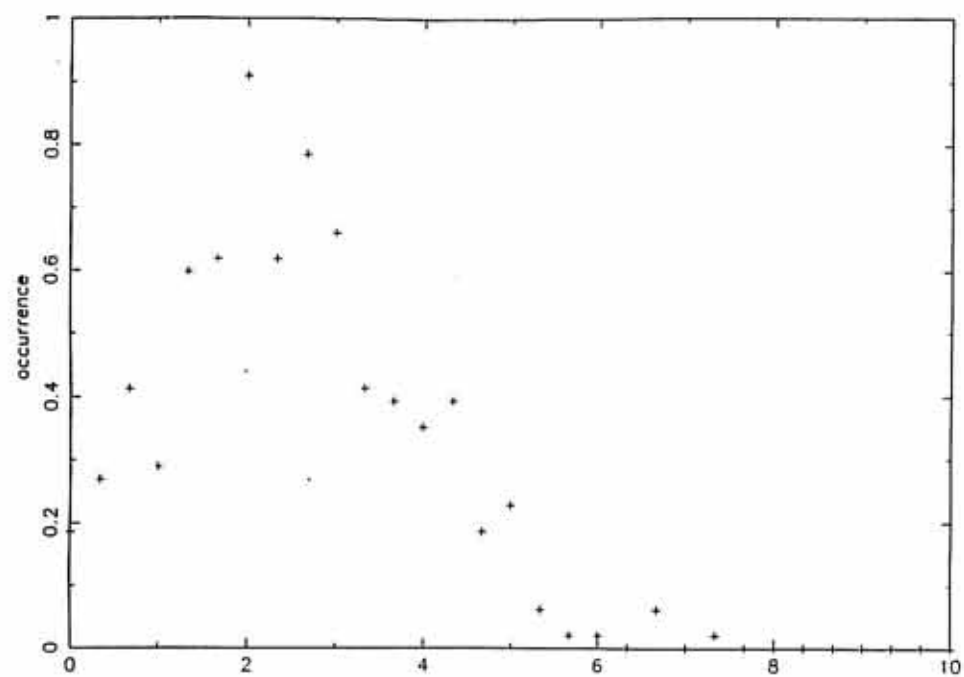


Figure is a plot of the distribution of Kp values for 1984

(b)

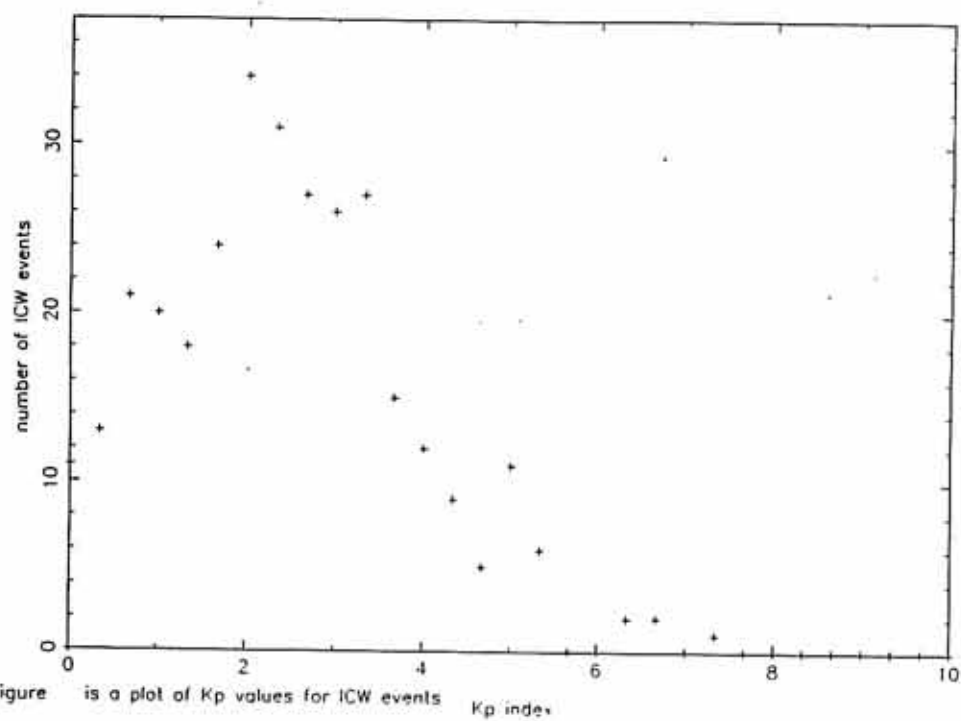


Figure is a plot of Kp values for ICW events

Figure 27      This figure (a) is a histogram of  $A_e$  index for the year of 1984, and (b) is a histogram of  $A_e$  index when ICW events were occurring.

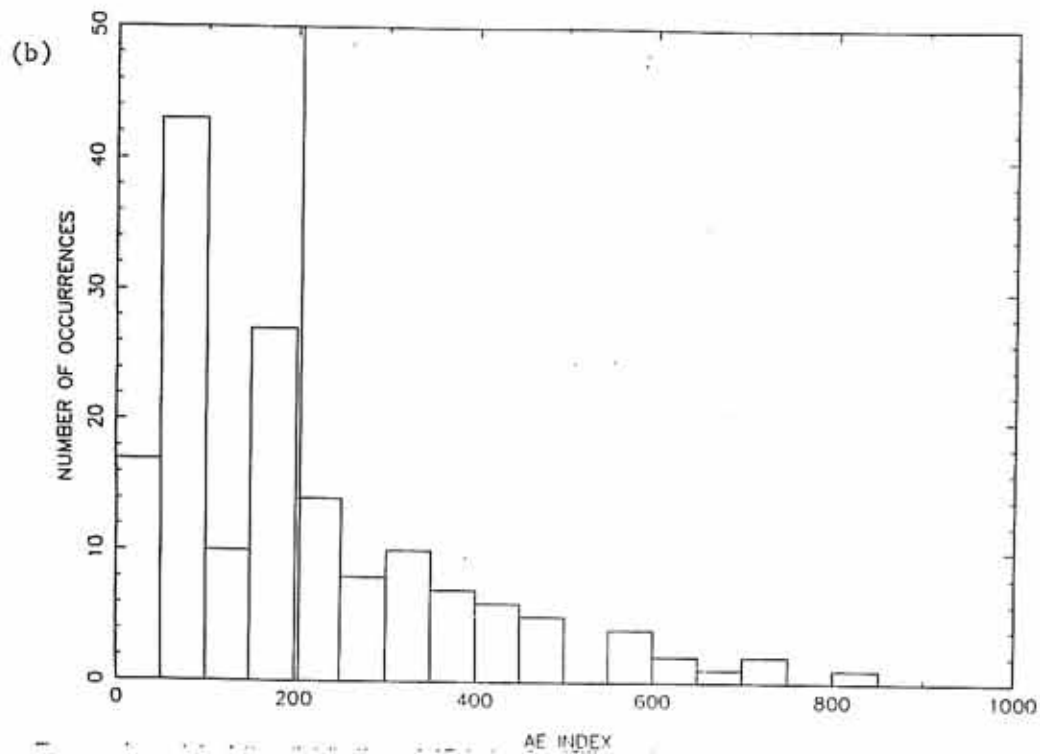
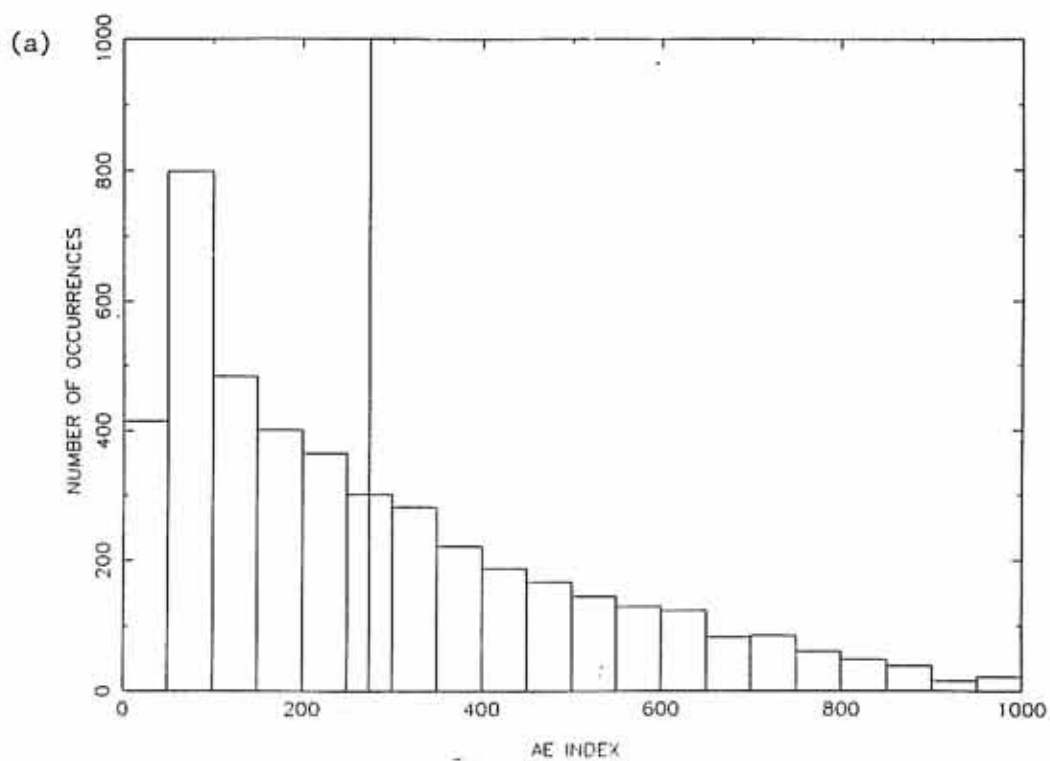


Figure 28      This figure is a spectrogram of the analog wideband electric field signal detected by the  $E_x$  antenna on DE-1 in the 0-1 kHz mode. Split  $H^+$  cyclotron harmonics are present between 300 Hz and 600 Hz.

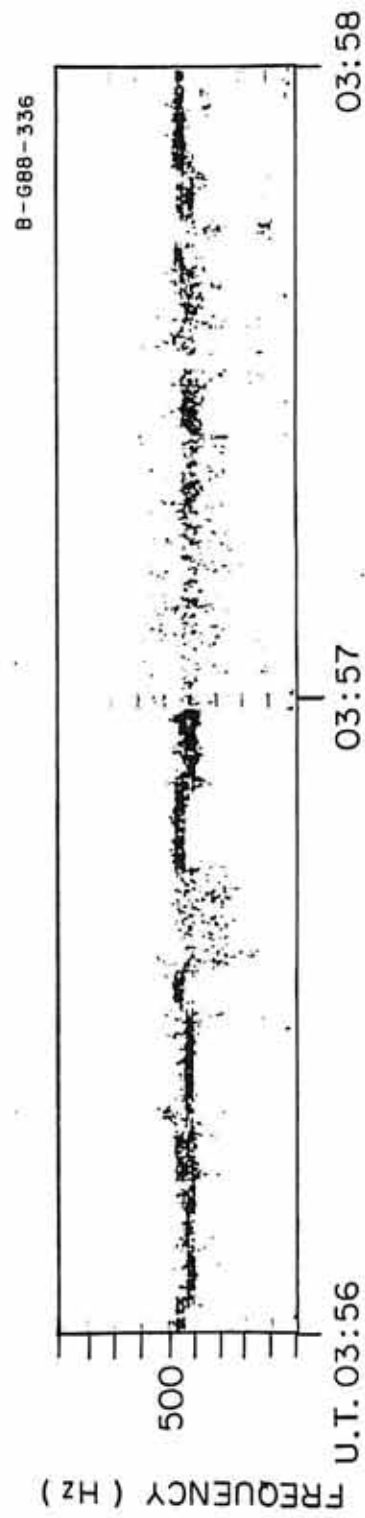
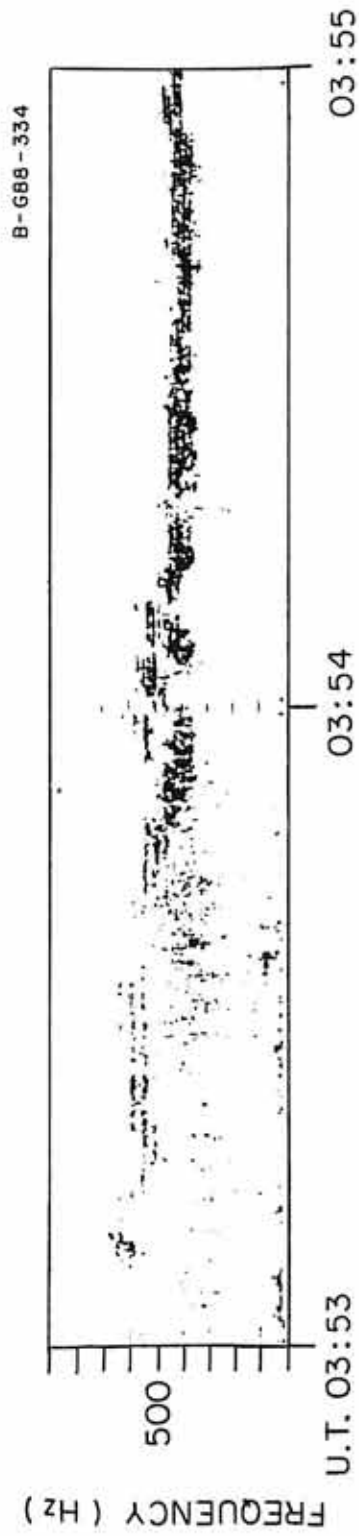


Figure 29      This figure (a) is a spectrum of the analog wideband electric field signal taken at 03:53:15 UT consisting of 50 spectrums averaged over 2.5 seconds. The evenly spaced lines are located at integer multiples of the  $H^+$  cyclotron frequency. This figure (b) is a spectrum of the analog wideband electric field signal taken at 03:54:40 UT consisting of 250 spectrums averaged over 12.5 seconds. The 9th through 11th harmonics are excited, each one is split. This figure (c) is a spectrum consisting of 50 spectrums averaged over 2.5 seconds taken at 03:55:35 UT. In this figure (d) is a spectrum consisting of 250 spectrums averaged over 12.5 seconds taken at 03:56:20 UT. The evenly spaced lines are located at integer multiples of the  $H^+$  cyclotron frequency.

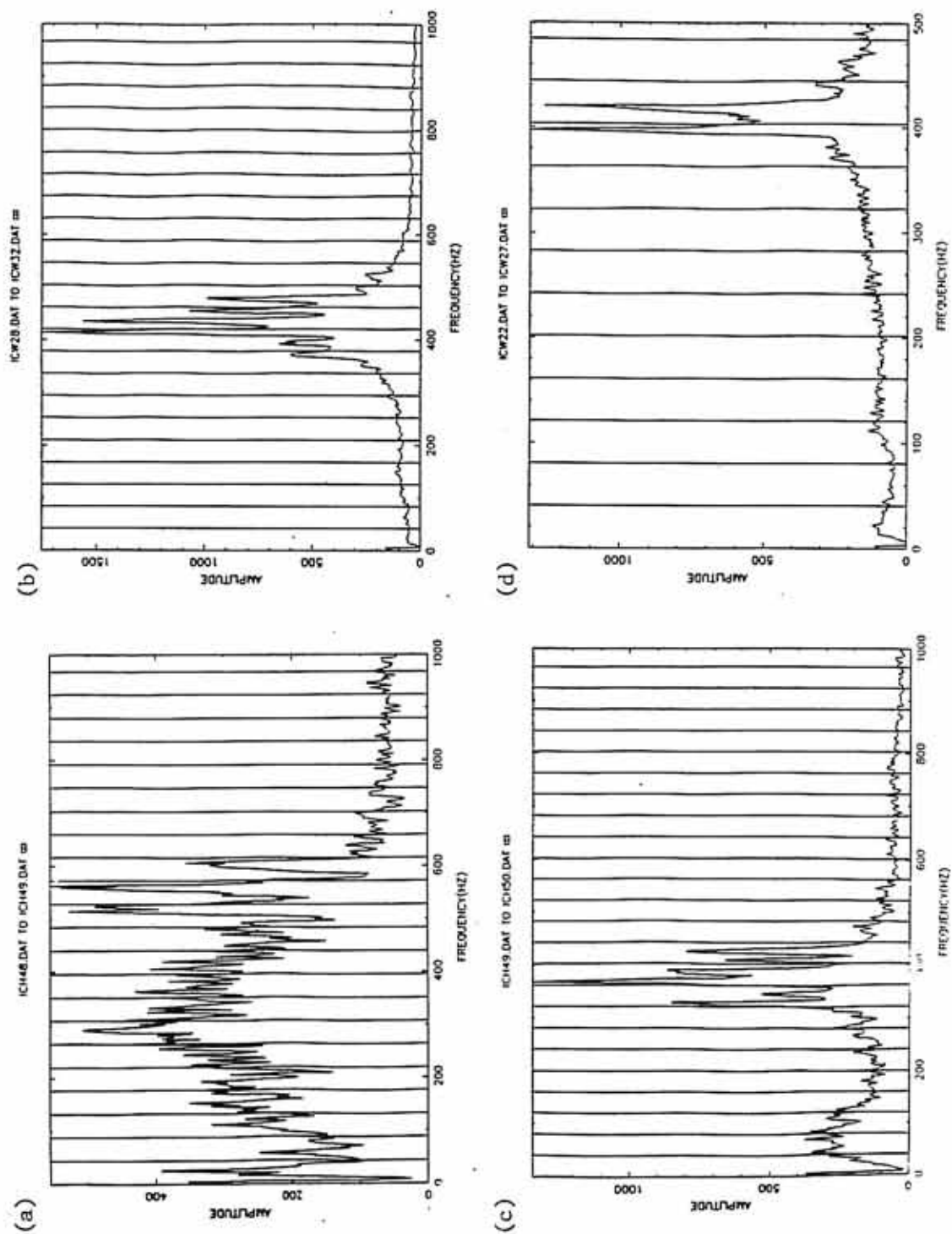


Figure 30      This figure is the rms electric field in the 10 Hz-1 kHz band measured by the  $E_x$  antenna versus time. The dashed vertical lines indicate when the  $E_x$  antenna is parallel to the magnetic field.



DE-1 84153 3:55 TO 3:56

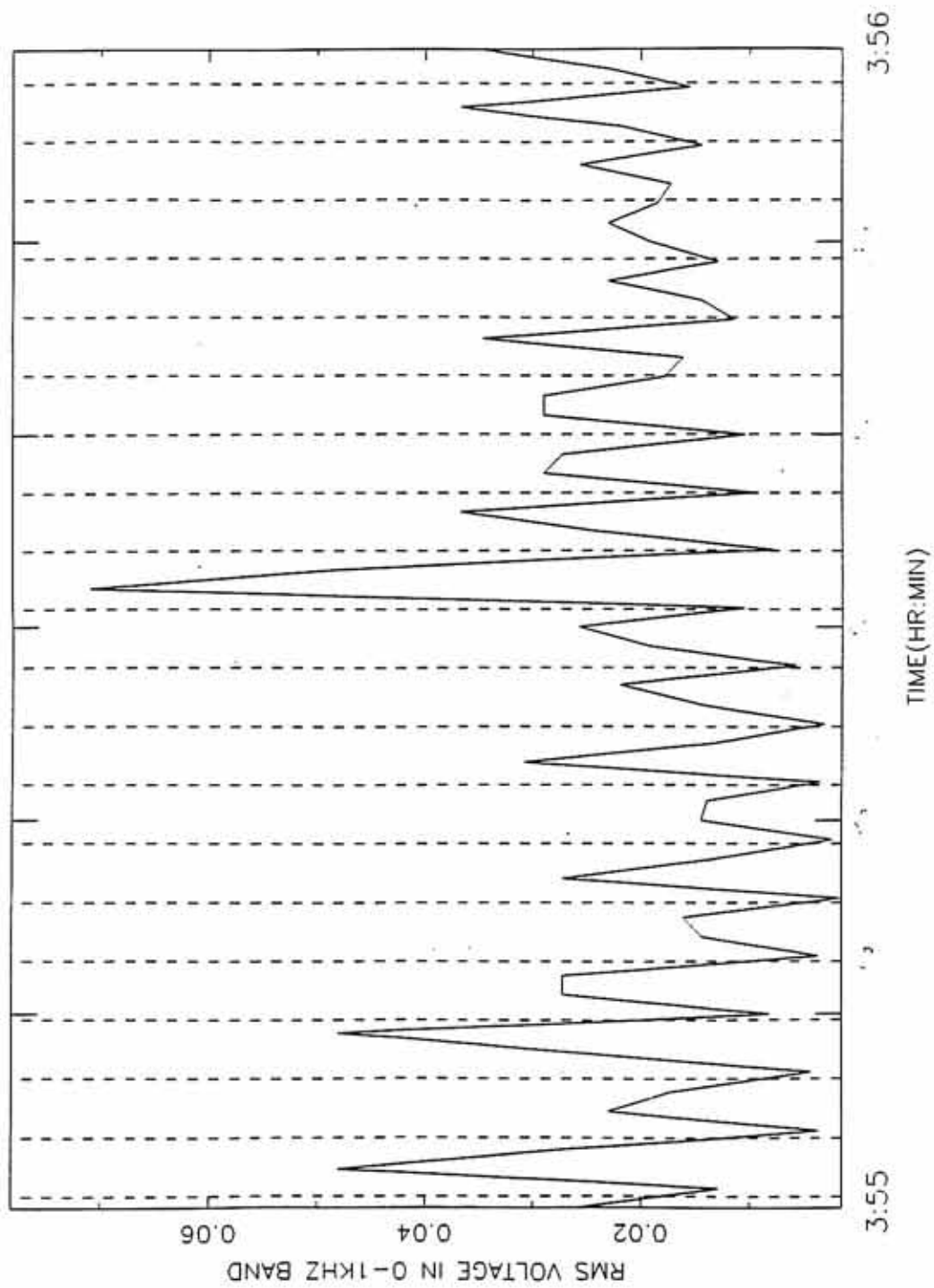


Figure 31      This figure (a) is a plot of the spectrum obtained when the  $E_x$  antenna is perpendicular to the magnetic field for various values of  $\Delta k_{\perp 0}/k_{\perp 0}$ .  $\Delta k_{\perp x}/k_{\perp 0} = (\omega - \omega_n)/(k_{\perp 0} V \sin \theta)$  relates the shift in frequency to  $k_{\perp x}$ . This figure (b) is a plot of the spectrum obtained when the  $E_x$  antenna is parallel to the magnetic field for various values of  $\Delta k_{\perp 0}/k_{\perp 0}$ .

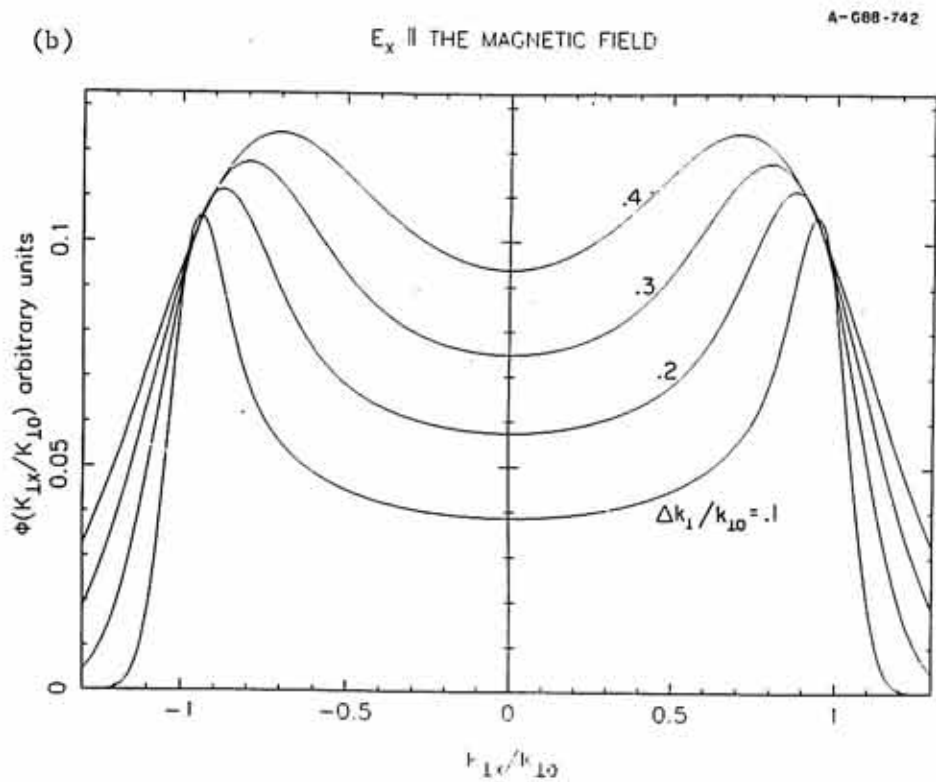
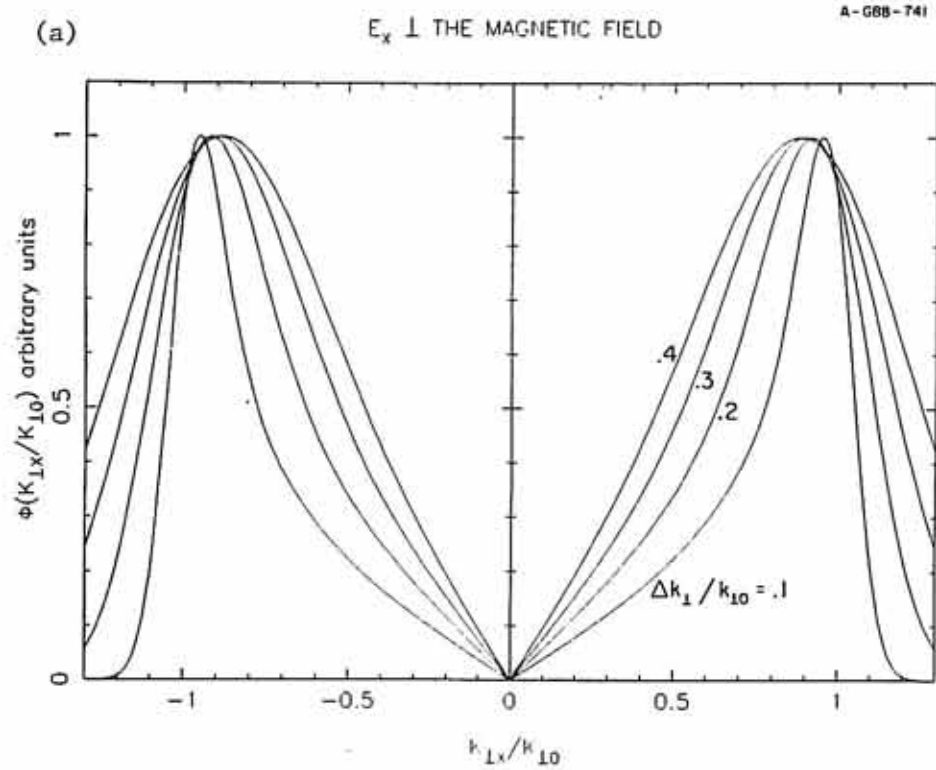


Figure 32    This figure is a plot of randomly selected perpendicular wave numbers lying in an annular ring of width  $2\Delta k_{\perp 0}$ , centered at  $k_{\perp 0}$ .

## EXCITED WAVE MODES PERPENDICULAR TO THE MAGNETIC FIELD

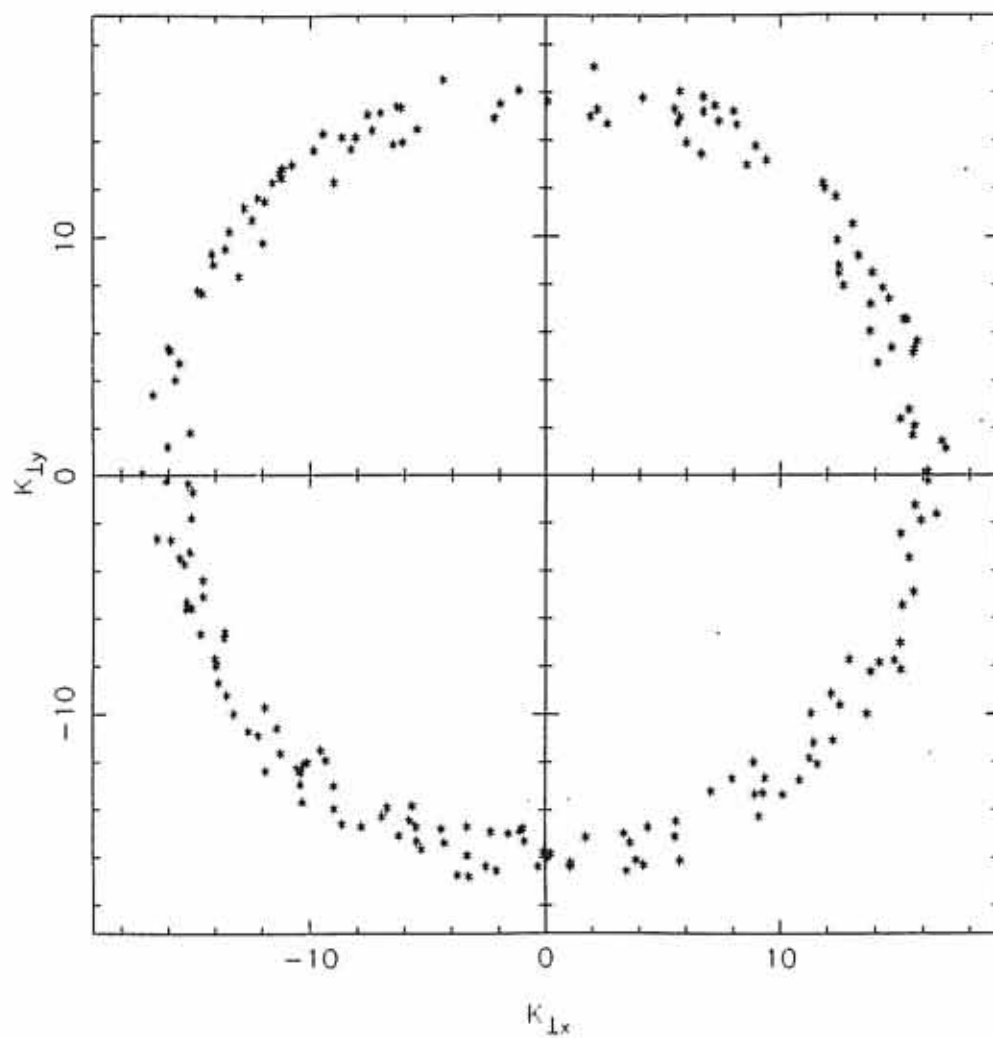
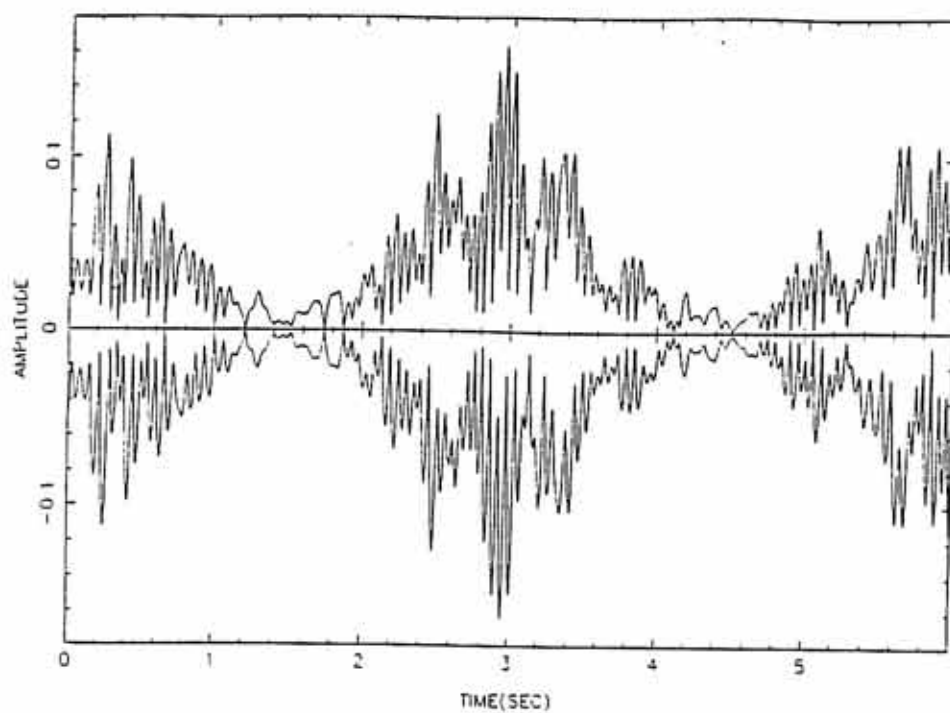
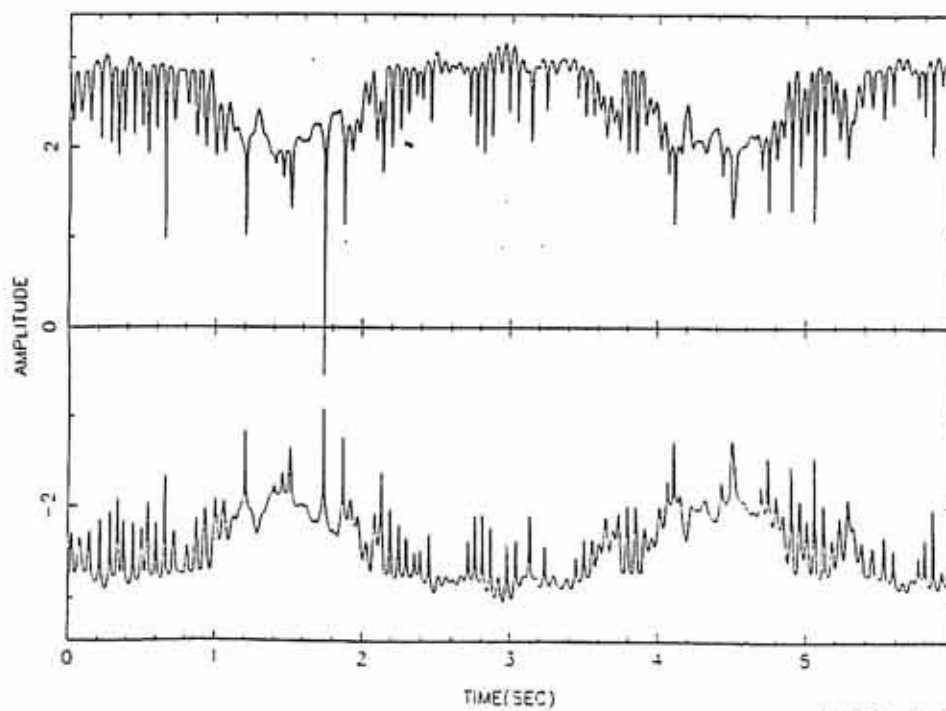


Figure 33     In this figure (a) is a plot of the envelope of computer generated signal as seen by the  $E_x$  antenna in DE-1's reference frame covering 1 spin period. The  $E_x$  antenna is parallel to the magnetic field at 1.5s and (b) is the envelope of the signal shown in Figure 33a after it has been compressed.

SIGNAL SAMPLED BY THE  $E_x$  ANTENNA

(a)

BGAROSON 13-APR-1968 21 55

SIGNAL(COMPRESSED) SAMPLED BY THE  $E_x$  ANTENNA

(b)

BGAROSON 13-APR-1968 22 03

Figure 34      This figure (a) is the spectrum made from the six second signal shown in Figure 33a. (b) is the spectrum made from the six second compressed signal shown in Figure 33b. (c) is a spectrum, which consists of averaging spectrums made from 1 second subintervals, which cover the spin period.



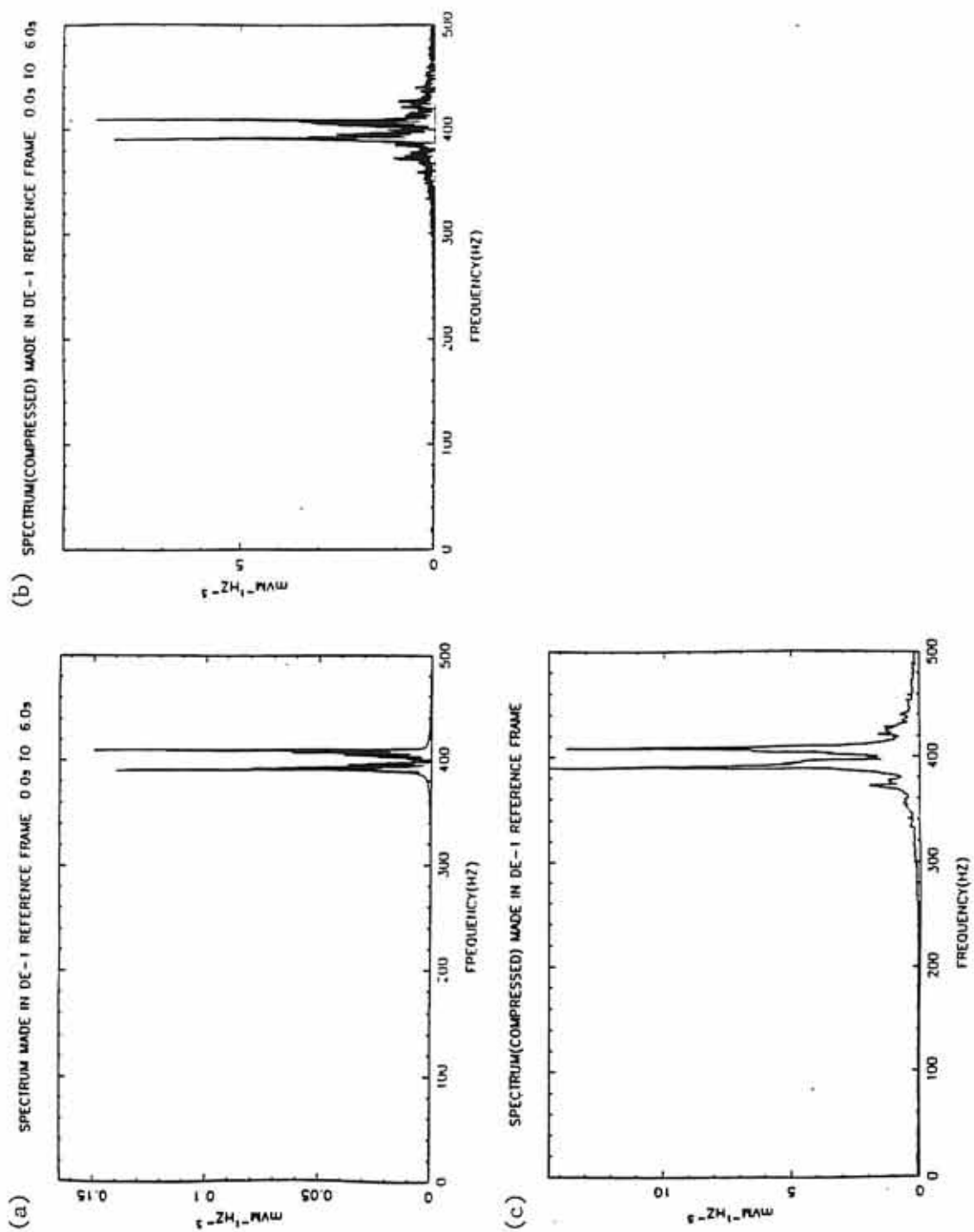
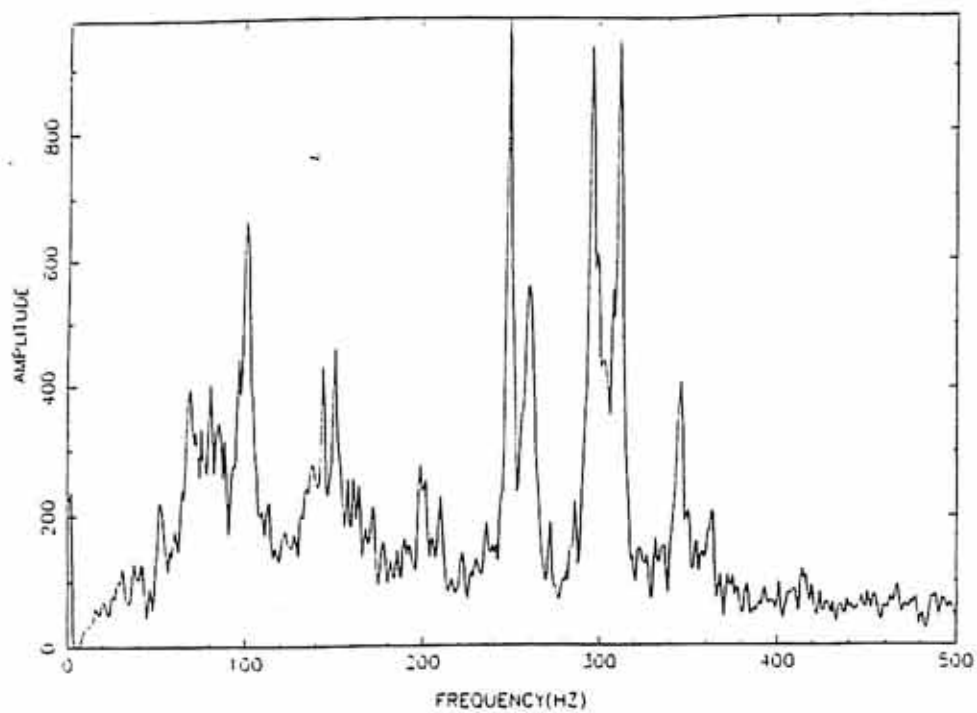


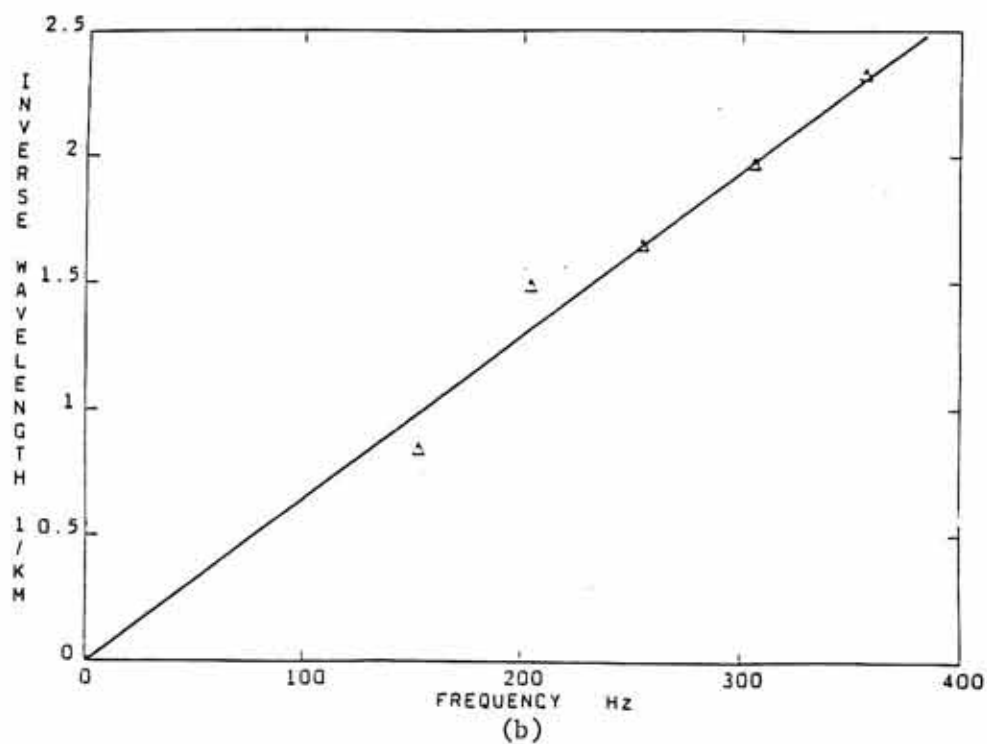
Figure 35    This figure (a) is a spectrum taken on January 15, 1984, where the 3rd to the 7th harmonics are excited. Figure (b) is a plot of the inferred inverse wavelengths versus the center frequencies for the excited harmonics shown in 8a.

(a)

ICW38 DAT TO ICW38 DAT



(a)



(b)

Figure 36 This figure is a plot of the log of phase space density versus energy for  $H^+$  during the wave event. Each curve refers to a different pitch angle range in which the particle detector was sampling.

# ETCS

JUN 1. 1984 3:56:22 3:56:46  
84153 14182065 14206034

| PITCH | ANGLE   |
|-------|---------|
| M/Q   | RANGE   |
| 1.0   | 0 45    |
| 1.0   | 45 90   |
| 1.0   | 90 135  |
| 1.0   | 135 180 |

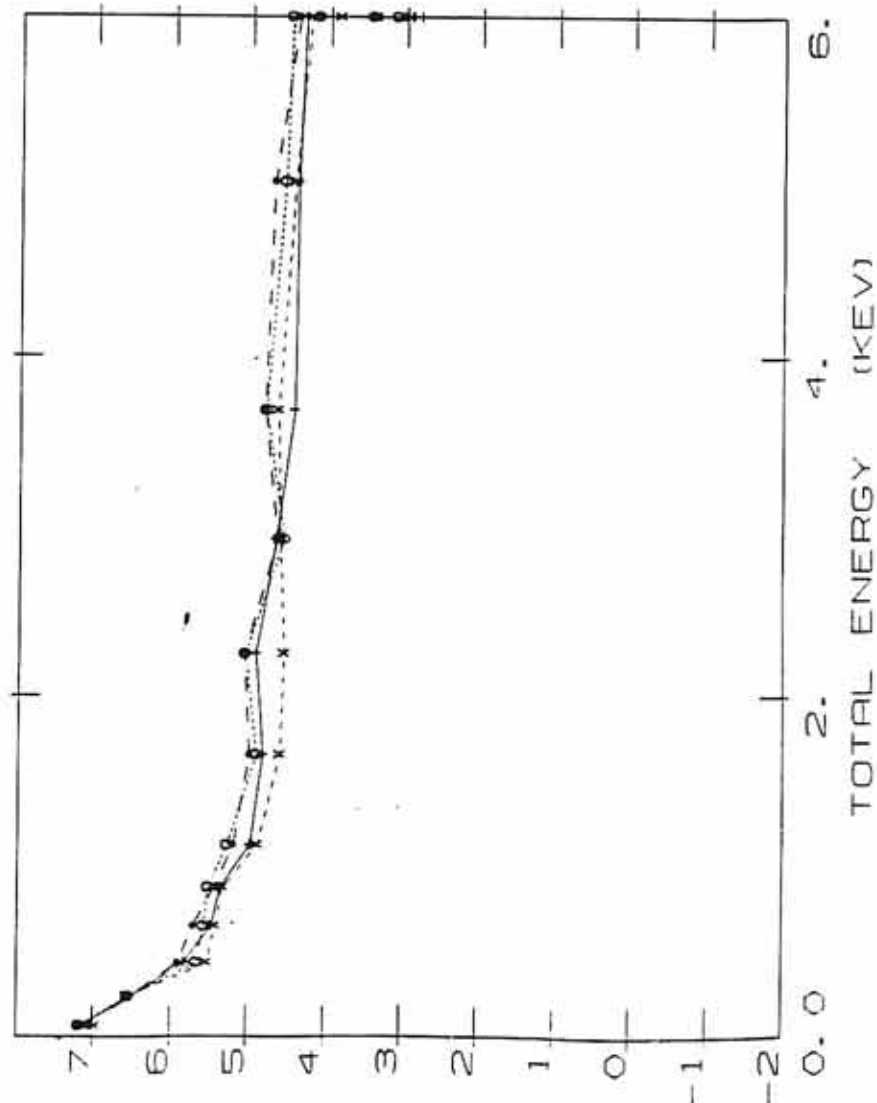


Figure 37      This figure is a histogram of the ratio of the second harmonic to that of the first harmonic for a number of ion cyclotron wave events, the peak in the histogram lies closer to 1 instead of 2.

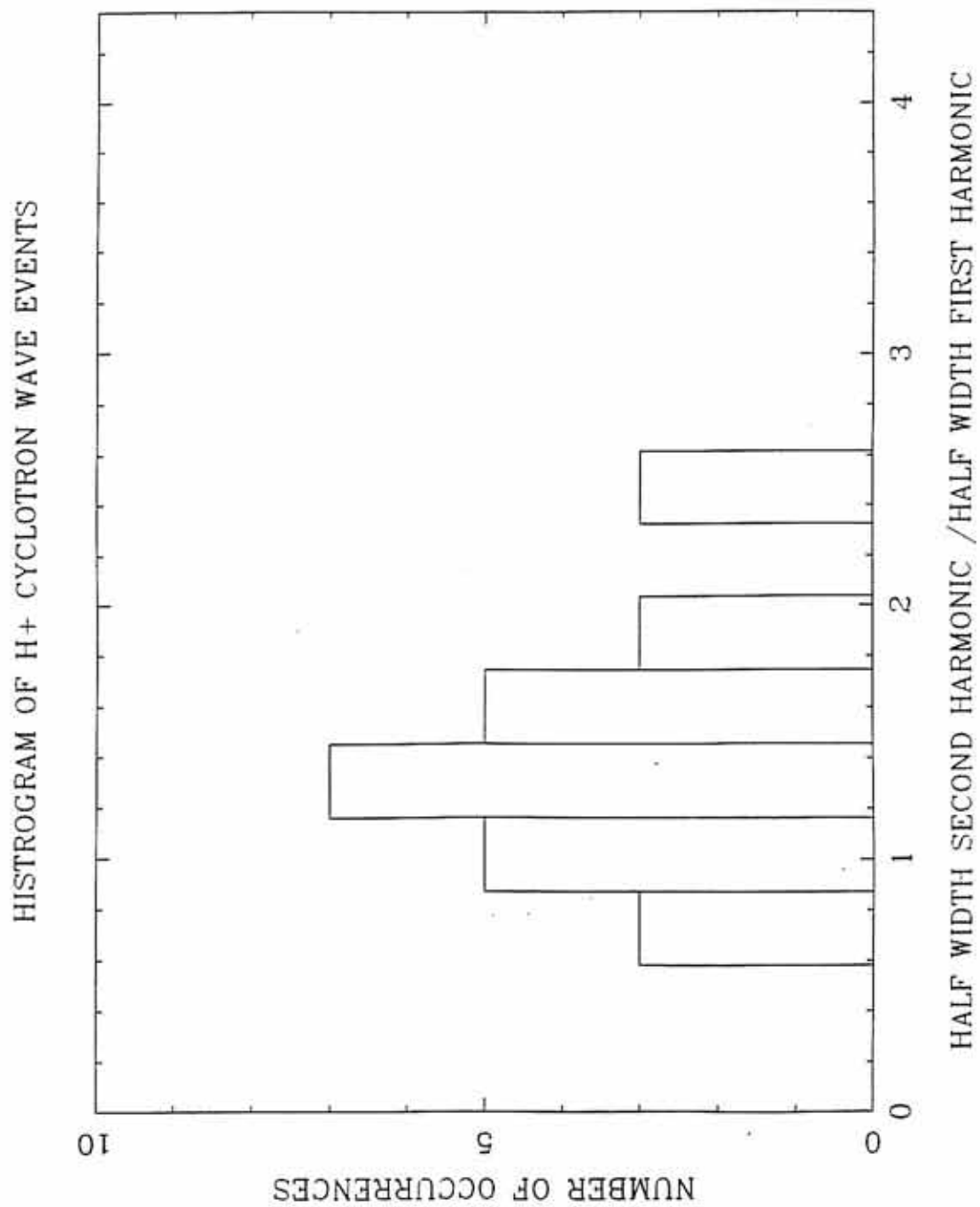


Figure 38     In this figure (a-c) shows the effect of introducing a phase coherence time into the wave modes that make up the signal. In Figure 38a the phase coherence time is .5s, coherence time is .1s (Figure 38b), and the phase coherence time is .025s in Figure 38c.



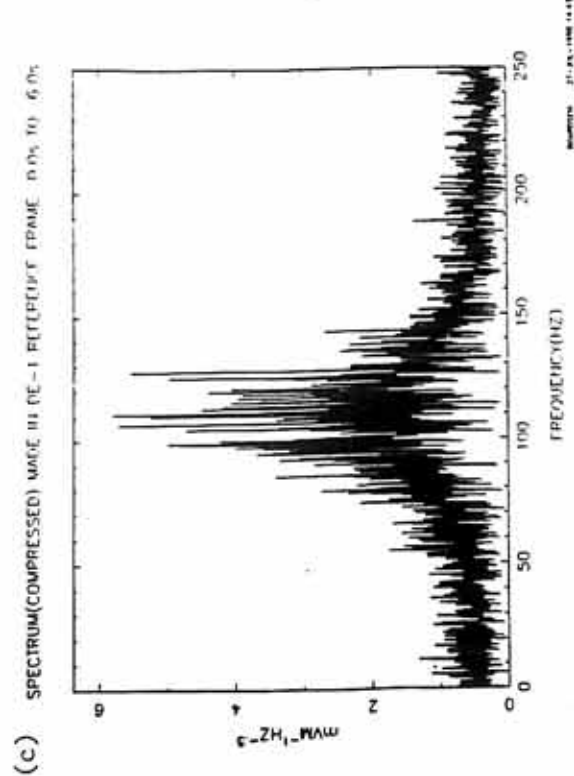
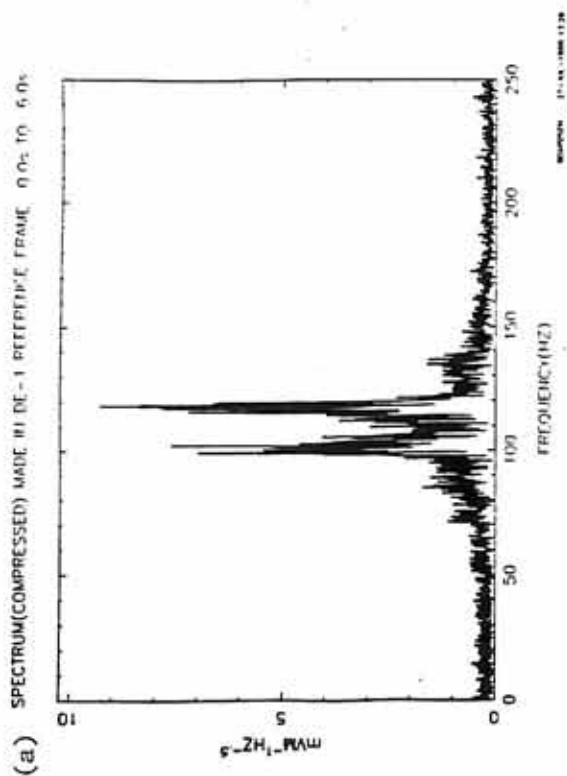
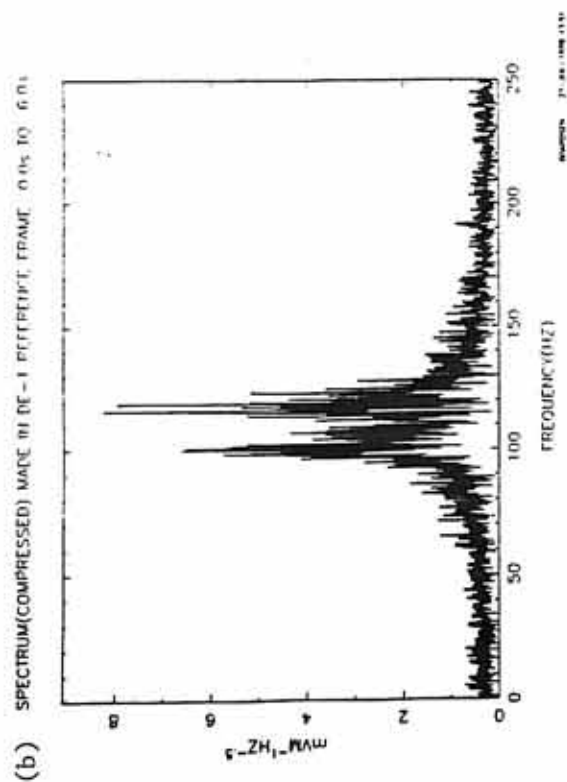


Figure 39    This figure is a schematic of the logarithmic compressor.

C-608-556

## L. F. COMPRESSOR CHARACTERISTICS

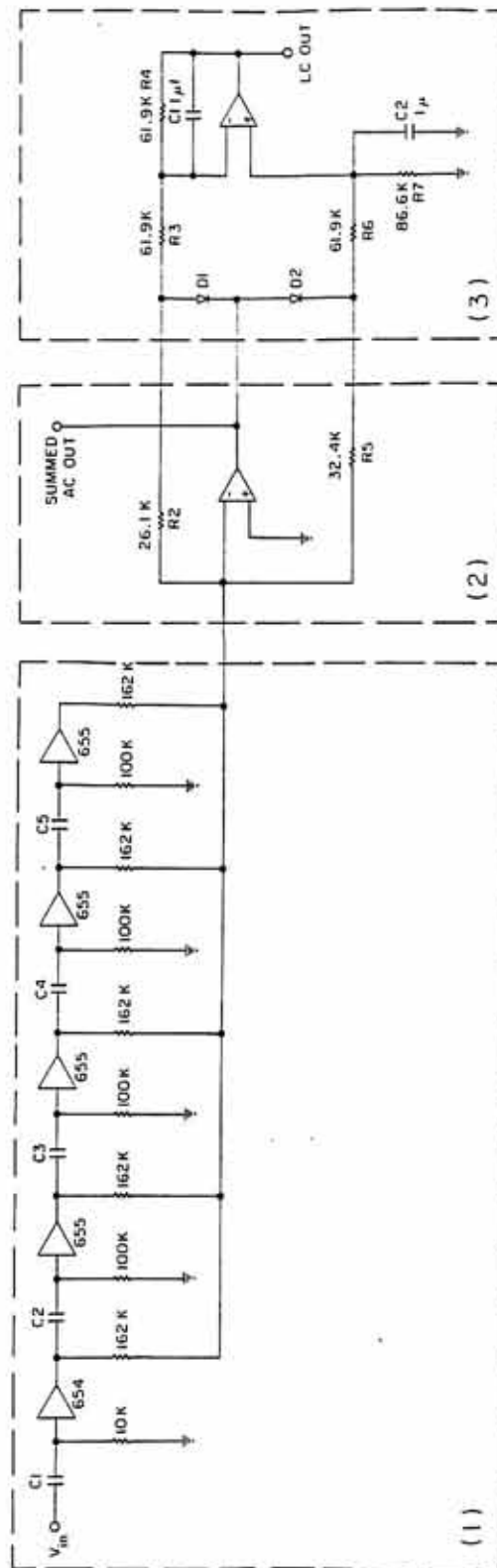
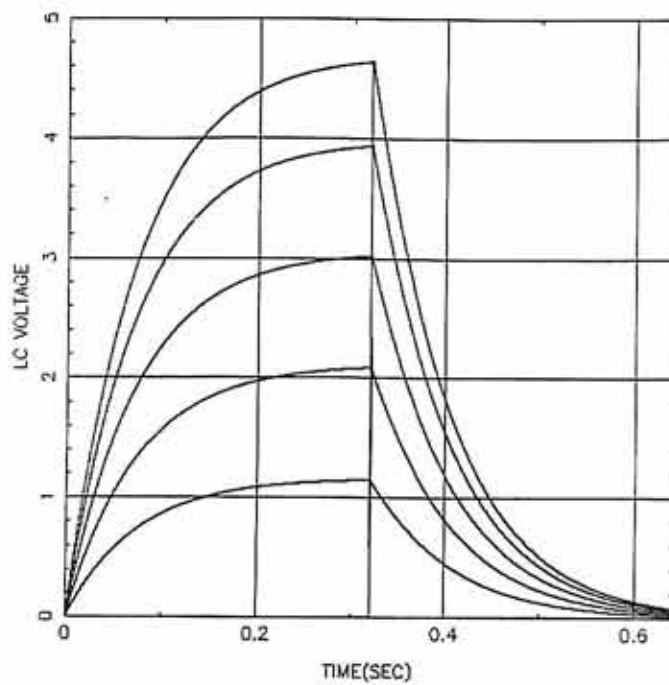


Figure 40      This figure shows the response time of the LC voltage when the input signal is suddenly switched on and then switched off after the LC voltage saturates. Each curve corresponds to an input signal with a different db level. Plot (a) is for a 700 Hz sine wave input signal, while plot (b) is for an input signal that consists of white noise.

(a) COMPRESSOR RESPONSE TIME 700HZ SINE WAVE



(b) COMPRESSOR RESPONSE TIME WHITE NOISE

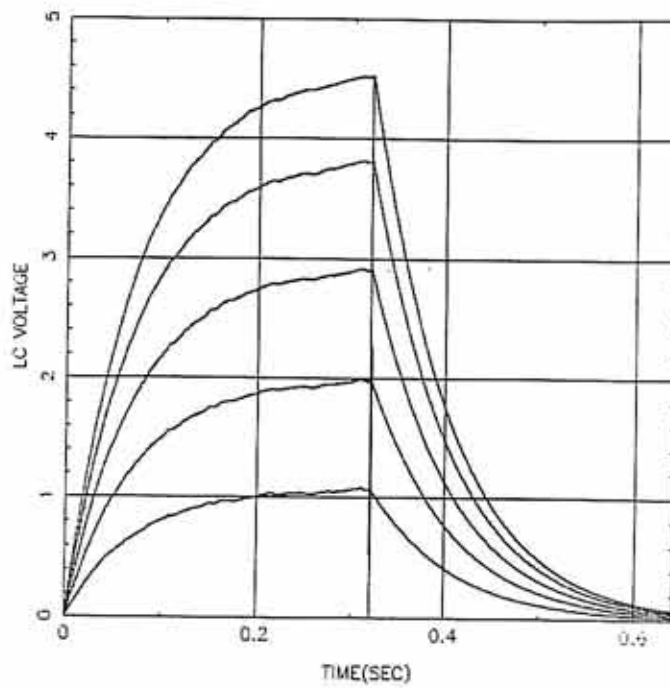


Figure 41      This figure is a preflight calibration curve of LC output voltage vs. input voltage in decibels (referenced to 1 volt rms) for a 700 Hz sine wave input signal. The superimposed curved (smoother of the two curves) is a computer model generated calibration curve.

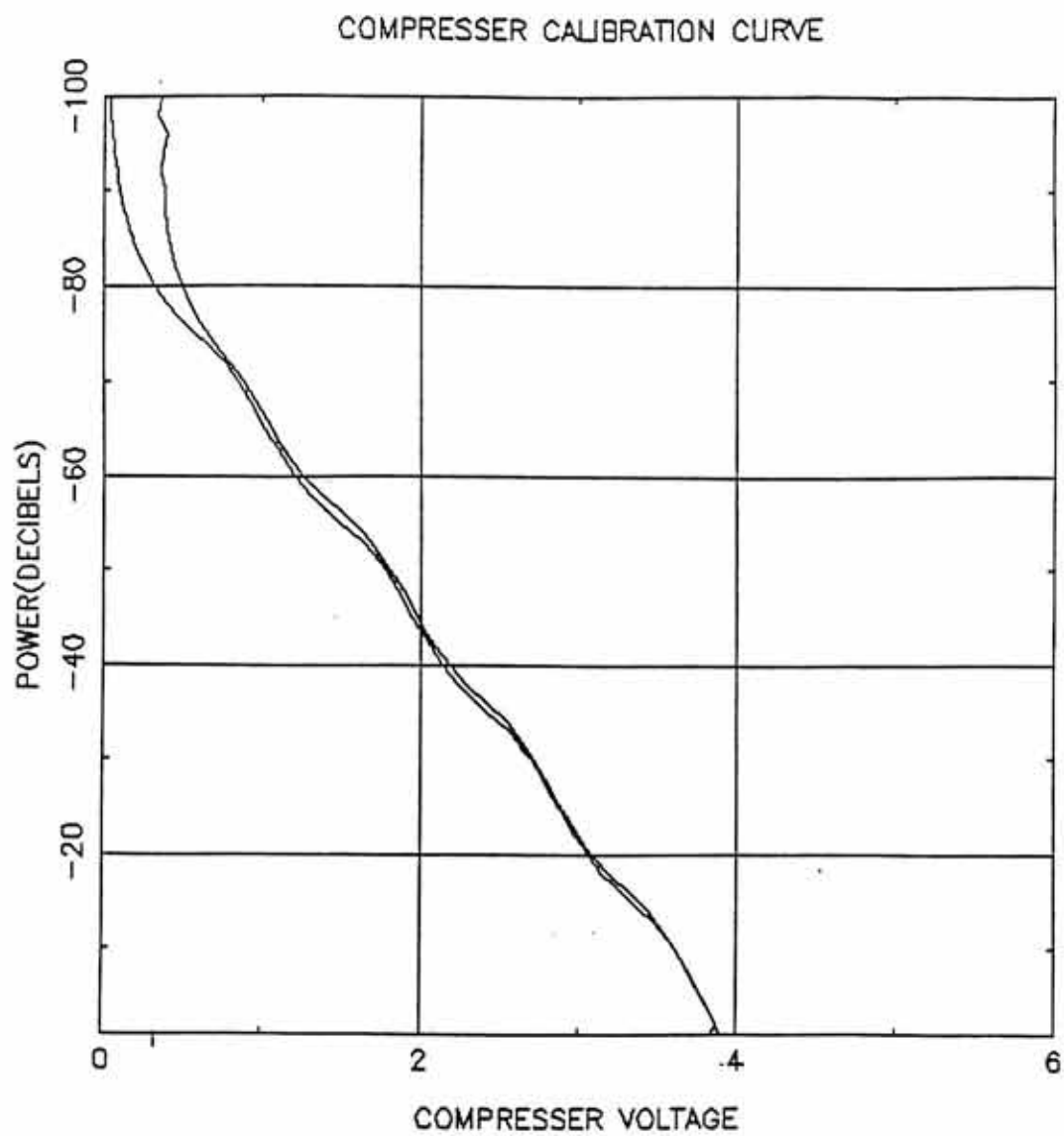
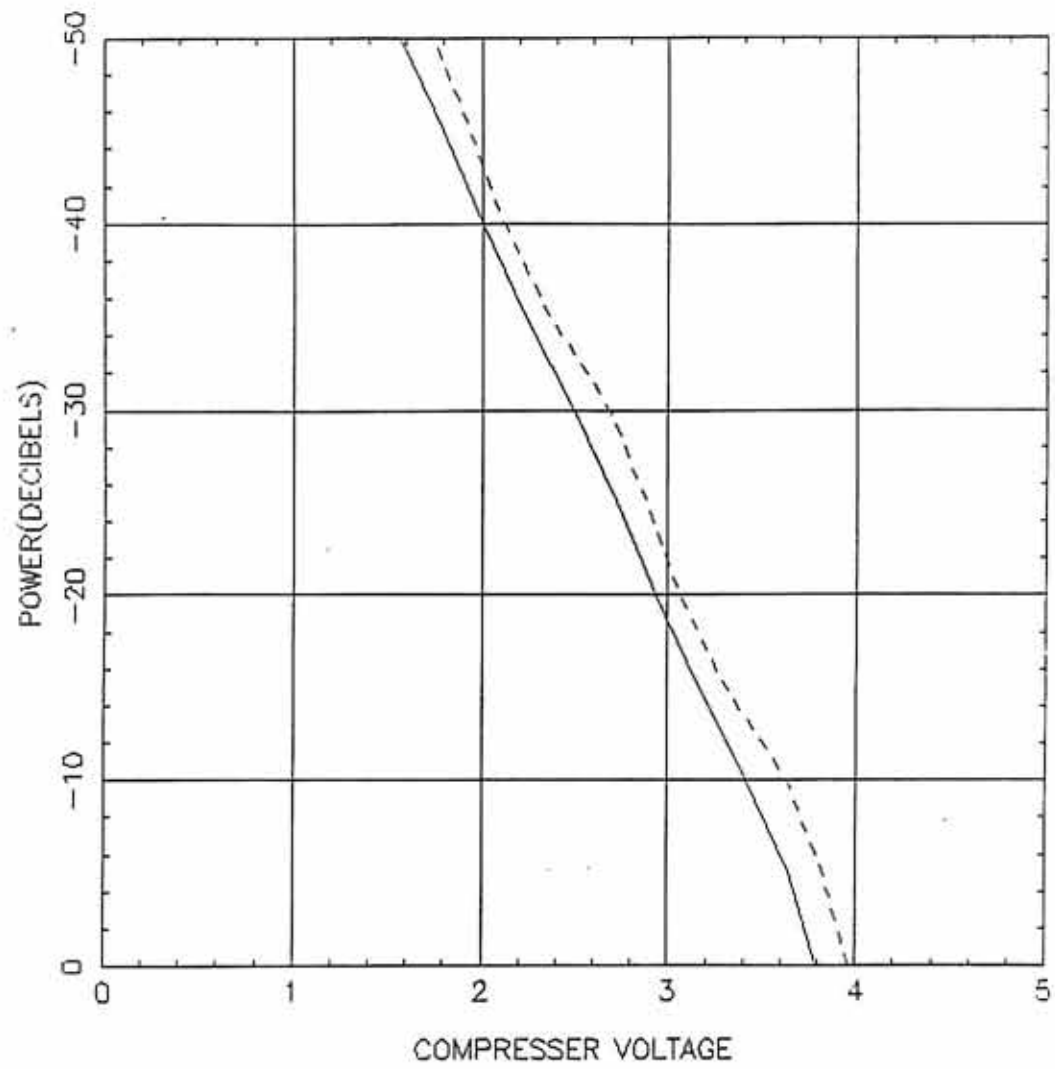


Figure 42      This figure is a superimposed plot of the LC level versus input signal power of the single component sine wave case as compared to the white noise case.



COMPRESSOR CALIBRATION CURVE



## APPENDIX: DISCUSSION OF THE LOGARITHMIC COMPRESSOR

Since the study is of data with a harmonic nature, it is important to consider the nonlinear distortion of the signal caused by the logarithmic compressor located in the wideband receiver. The logarithmic compressor is the principal source of nonlinear signal distortion. To gain a quantitative understanding of the amount of distortion that occurs the logcompressor was modeled.

### A. Discussion of the Compressor Circuitry

Figure 39 is a schematic of the logcompressor. The circuitry can be broken up into three parts. The first part consists of a series of four coupled operational amplifiers. Each amplifier has a gain of 10 and clips the output at roughly 5 volts. The output of one amplifier provides the input for the next amplifier.

The original input signal and the four output signals from the coupled amplifiers are added together in the second part of the circuit which is a voltage summer. For example, if the input signal voltage is 4 volts, the output will be  $4+5+5+5+5 = 24$  volts, an input voltage of .4 volts will have an output of  $.4+4+5+5+5 = 19.4$  volts 24.6 volts peak. Therefore, the input signal is compressed with the compressed signal being proportional to the logarithm of the input signal,

although when the input signal becomes small, less than 2.4 millivolts, the compression becomes linear.

Figure 1b is the compressed signal of a sine wave. Note that compression makes the sine wave look more like a square wave. The compressed signal is transmitted back to Earth and will be referred to as the summed AC output signal. This signal contains the frequency information of the detected waves.

In the third part of the circuitry, the signal is rectified and filtered, this voltage is sampled every eighth of a second and is transmitted in the digital data stream. This signal will be referred to as the LC output signal. The LC voltage is close to the rms voltage of the compressed signal. Figure 40 shows the response time of the LC voltage when the input signal is suddenly switched on and then switched off after the LC voltage saturates. This plot indicates that the response time is on the order of two tenths of a second. This time determines the lowest time resolution possible for determining input power based on the LC voltage, although the response of the summed AC signal to a sudden change in power is almost instantaneous.

The modeling of the logcompressor was done by approximating the amplifiers with ideal amplifiers (saturation voltage is included), letting the diodes assume either a perfect conducting or nonconducting state depending upon their bias. The two diodes yield four possible combinations of on-off states, each diode combination yields a linear circuit. The on-on and off-off diode combinations are states which occur only for zero seconds, so they are not taken into consideration.

Therefore, the mathematical modeling of the circuitry switches between the state on-off and off-on for the diodes D1 and D2 (labelled in the schematic), respectively, depending on the bias of the diodes.

To test the accuracy of the model, computer generated calibration curves were produced that are in good agreement with the calibration curves produced from preflight calibration of the wideband receiver. Figure 41 is a calibration curve of LC output voltage versus input voltage in decibels (referenced to 1 volt rms). The input voltage was a 700 Hz sine wave whose input amplitude was varied over the range indicated. The preflight calibration curve starts to level off at an input of -70 dB due to the pick up of environmental noise present when the calibration was made. The curve superimposed upon the experimental calibration curve is the calibration curve generated by the computer model of the logcompressor. The fit was obtained by varying a scale factor on the input voltage and the saturation levels of the amplifiers, a better fit could be obtained by varying the saturation level of each amplifier individually. The scale factor and saturation voltage used are in reasonable agreement with the engineering data on the circuitry.

Figure 42 is a superimposed plot of the LC level versus input signal power of the single component sine wave case as compared to the white noise case. Note that the corresponding curves for a given LC level differ in input power by at most 6 dB with a 3 dB difference being the typical value. This shows that a  $\pm 25\%$  (6 dB uncertainty) estimate of the input power in the 0-1000 Hz band can be made from the

calibration curves based on transmitted LC data regardless of the type of frequency components in the 0-1000 Hz band, but it is not clear how the power is distributed within the band due to the instrumental generation of harmonics.

In order to correct for nonlinear distortion of the received signal, the signal must be decompressed to obtain the original input signal. If the peak input signal is less than 2.4 millivolts, the logcompressor response is linear. There are a number of problems associated with regenerating the input signal to the log-compressor. A small DC shift (less than 10% of the summed AC signal amplitude) due to small differences in signal amplification when the signal bias is negative compared to positive is lost due to AC coupling. The computer model has to be a good approximation of the actual instrumentation. Since the amplitude of the signal is uncalibrated the signal has to be decompressed in a cyclic manner, adjusting the signal amplitude in each cycle and comparing the computer generated LC values with the measured LC values. Since ion cyclotron waves are generally large in amplitude and drive the logcompressor into the logarithmic regime, noise added to the signal during transmission and reception, now becomes a major obstacle to decompressing the data. The noise added to the signal by the ground station receiver can result in signal to noise ratio as high as 10 dB. These factors indicate that little information can be retrieved by trying to regenerate the original input signal.

### B. Computer Generated Test Signals

The computer model can be used to investigate how well the frequency time spectrograms generated from the summed AC data, will reflect reality for various LC levels. Simple artificial input signals were generated by the computer, from which frequency spectrums were made of the input and summed AC signals. A few examples are shown in Figure 3a-d.

The modeling indicates that for input signals of high amplitude the instrumental harmonics are generated with spacings at integer increments of the input frequencies and difference frequencies, so care must be taken in interpreting wideband data.

## REFERENCES

- Akasofu, S.-I., Auroral arcs and auroral potential structure, Physics of Auroral Arc Formation, S.-I. Akasofu and J. R. Kan, Editors, p. 1, 1981.
- Ashour-Abdalla, M., and R. M. Thorne, Toward a unified view of diffuse auroral precipitation, J. Geophys. Res., 83, 4755, 1978.
- Ashour-Abdalla, M., and H. Okuda, Turbulent Heating of Heavy Ions on Auroral Field Lines, J. Geophys. Res., 89, 2235, 1984.
- Bergmann, R., Electrostatic Ion (Hydrogen) Cyclotron and Ion Acoustic Wave Instabilities in Regions of Upward Field-Aligned Current and Upward Ions Beams, J. Geophys. Res., 89, 953, 1984.
- Bering, E. A., M. C. Kelley, and F. S. Mozer, Observations of an intense field aligned thermal ion flow and associated intense narrowband electric field oscillations, J. Geophys. Res., 80, 4612, 1975.
- Borovsky, J. E., The production of ion conics by oblique double layers, J. Geophys. Res., 89, 2251, 1984.
- Choy, L. W., R. L. Arnoldy, W. Potter, P. Kintner, and L. J. Cahill, Jr., Field aligned particle currents near and auroral arc, J. Geophys. Res., 76, 9879, 1971.
- Cloutier, P. A., H. R. Anderson, R. J. Park, R. R. Vondrak, R. J. Spiger, and B. R. Sandel, Detection of geomagnetically aligned currents associated with and auroral arc, J. Geophys. Res., 75, 2595, 1970.
- Collin, H. L., W. K. Peterson, and E. G. Shelley, Solar cycle variation of some mass dependent characteristics of upflowing beams of terrestrial ions, J. Geophys. Res., 92, 4757, 1987.
- D'Angelo, N. and R. W. Motley, Electrostatic oscillations near the ion cyclotron frequency, Phys. Fluids, 5, 663, 1962.
- Drummond, W. E., and M. N. Rosenbluth, Anomalous diffusion arising from microinstabilities in a plasma, Phys. Fluids, 5, 1597, 1962.

- Gorney, D. J., S. R. Church, and P. F. Mizera, On ion harmonic structure in auroral zone waves: The effect of ion conic damping of auroral hiss, J. Geophys. Res., 87, 10,479, 1982.
- Hoffman, R. A., and C. S. Lin, Study of inverted-V auroral precipitation events, Physics of Auroral Arc Formation, S.-I. Akasofu and J. R. Kan, Editors, p. 80, 1981.
- Kaufmann, R. L. and P. M. Kintner, Upgoing ion beams: 1. Microscopic analysis, J. Geophys. Res., 87, 10,487, 1982.
- Kindel, J. M. and C. F. Kennel, Topside current instabilities, J. Geophys. Res., 76, 3055, 1971.
- Kintner, P. M., On the distinction between electrostatic ion cyclotron waves and ion cyclotron harmonic waves, Geophys. Res. Lett., 7, 585, 1980.
- Kintner, P. M., M. C. Kelly, and S. F. Moser, Electrostatic hydrogen cyclotron waves near one Earth radius in the polar magnetosphere, Geophys. Res. Lett., 5, 139, 1978.
- Kintner, P. M., M. C. Kelley, R. D. Sharp, A. G. Ghielmetti, M. Temerin, C. Cattell, P. F. Mizera, and J. F. Fennel, Simultaneous observation of energetic (keV) upstreaming ions and electrostatic hydrogen cyclotron waves, J. Geophys. Res., 84, 7201, 1979.
- Klumpar, D. M., Transversely accelerated ions: An ionospheric source of hot magnetospheric ions, J. Geophys. Res., 89, 10,779, 1984.
- Mosier, S. R., and D. A. Gurnett, Ionospheric observation of VLF electrostatic noise related to harmonics of the proton gyrofrequency, Nature, 223, 605, 1969.
- Moser, F. S., C. W. Carlson, M. K. Hudson, R. B. Torbert, B. Parady, T. Yatteau, and M. C. Kelley, Observations of paired electrostatic shocks in the polar magnetosphere, Phys. Rev. Lett., 38, 292, 1977.
- Okuda, H., and K.-I. Nishikawa, Ion-beam-driven electrostatic hydrogen cyclotron waves on auroral field lines, J. Geophys. Res., 89, 1023, 1984.
- Peterson, W. K., E. G. Shelley, S. A. Boardsen, and D. A. Gurnett, Transverse auroral ion energization observed on DE-1 with simultaneous plasma wave and ion composition measurements, Ion Acceleration in the Magnetosphere and Ionosphere, T. Chang, Editor, 1986.



- Peterson, W. K., E. G. Shelley, S. A. Boardsen, D. A. Gurnett, B. G. Ledley, M. Sugiura, T. E. Moore, and J. H. Waite, Jr., Transverse ion energization and low frequency plasma waves in the mid-altitude auroral zone: A case study, J. Geophys. Res., accepted for publication.
- Sharp, R. D., R. G. Johnson, and E. G. Shelley, Observation of an ionospheric acceleration mechanism producing energetic (keV) ions primarily normal to the geomagnetic field direction, J. Geophys. Res., 82, 3324, 1977.
- Shelley, E. G., R. D. Sharp, and R. G. Johnson, Satellite observations of an ionospheric acceleration mechanism, Geophys. Res. Lett., 3, 654, 1976.
- Temerin, M., The polarization, frequency, and wavelengths of high-latitude turbulence, J. Geophys. Res., 83, 2609, 1978.